Design and Characterisation of Quantum Dot Lasers

A thesis submitted in fulfilment of the partial requirement for the degree of Doctor of Philosophy

by

Maryam Alsayyadi

School of Physics and Astronomy - Cardiff University

UK

December 2024

Abstract

InAs quantum dot (QD) lasers grown on GaAs substrates have demonstrated significant advantages over quantum well devices, including low threshold currents and long-term reliability, particularly for applications on silicon platforms. For longer wavelengths around 1550 nm, InAs QD lasers on InP substrates have been explored; however, limited studies exist for achieving high-performance QD lasers in this range.

This work primarily focuses on lasers fabricated from InAs quantum dots (QDs) on InP substrates grown by metal-organic chemical vapor deposition (MOCVD). High performance AlGaInAs/InP multi-quantum-well (MQW) laser diodes are first examined for comparison, with the QW structures exhibiting a gain parameter (NG_0) as high as 94.4 cm^{-1} for 9-QW layer samples. Simulations of AlInGaAs/InP MQW laser diodes highlight the poor performance at high temperature and demonstrate the benefits of incorporating an electron stopper layer. This layer may be useful to reduce thermionic emission and electron leakage while maintaining efficient carrier injection.

For samples intended to operate as quantum dots the laser performance is explored and the question as to whether dots, dashes or modulated quantum wells are formed under varying growth conditions is examined. Here performance limitations related to a small optical gain are identified.

Epitaxial structures are grown on n-type InP substrates using MOCVD, and broad-area lasers with oxide-isolated stripe widths of 50 μm are fabricated using standard photolithography. The lasers feature uncoated facets, cavity lengths ranging from 300 μm to 2000 μm, and emission wavelengths around 1550 nm. A 5-layer InAs/InP QD laser structure with 0.7 nm capping layers achieved optical gain of approximately 60 cm^{-1} and ground-state lasing up to 390 K for cavity lengths as short as 330 μm. These structures demonstrate minimal gain saturation, with a G_0 per layer similar to the quantum well lasers, showcasing their potential as optical sources for silicon-photonics.

Additionally, 3-layer and 5-layer QD structures with 4 nm capping layers are investigated, with their performance under various growth conditions evaluated, including the use of (Al)InGaAs capping layers. Three distinct laser diode structures,

each with two fabrication orientations, are analyzed to differentiate between dot and dash morphologies. A multi-section technique is employed to measure modal gain and absorption spectra. At room temperature, internal optical losses ranged from to 15±0.2 cm^{-1}, for quantum dashes (QDH) to 18±2 cm^{-1}, for quantum wells (QW). Peak modal gains of 40±2 cm^{-1} and 24±2 cm^{-1} were observed for QW and QDH lasers, respectively, under injected current densities. These findings highlight the potential of InAs/InP QDH lasers for operation on silicon at 1.55μm.

Acknowledgments

Praise be to Allah, the Most Gracious and the Most Merciful. With deep gratitude and humility, I express my heartfelt thanks to Allah, whose countless blessings have enabled me to complete this thesis.

I extend my sincere gratitude and appreciation to my primary supervisor, Prof. Peter Smowton, for his exceptional patience, insightful guidance, steadfast encouragement, and invaluable advice throughout this journey. I am also profoundly thankful to my secondary supervisor, Dr. Sam Shutts, for his generous support and for engaging in thought-provoking discussions.

I am profoundly thankful to everyone who contributed to the completion of this research, whether through knowledge, assistance, or moral support. My deepest thanks go to my colleagues, Dr. Fwoziah Albeladi, Dr. Curtis Hentschel, and Dr. Zhongming Cao, who shared this journey of knowledge and hard work with me.

Special thanks to my mentor, Dr. Ana Duarte Cabral, for her supportive words and constructive communication, as well as to my colleagues, whose presence and positive influence have enriched my academic experience. Your fruitful discussions have played a significant role in this journey.

To my dearest friends, I owe a debt of gratitude for standing by me through every challenge. Your encouragement and unwavering support have been a source of strength and motivation throughout this journey.

I would like to acknowledge my sponsor in Saudi Arabia, Taibah University, for providing me with the opportunity to do this PhD.

To my beloved parents, whose endless love, prayers, and support have been the foundation of all my achievements, I dedicate this work with heartfelt appreciation. Your unwavering belief in me has been my guiding light. To the cherished memory of those who have departed but left an indelible mark on my life, and to my beloved siblings, whose constant encouragement and love have been a pillar of support, I offer my deepest thanks and dedicate this humble work as a token of my gratitude.

Lastly, I am deeply grateful to everyone who believed in me, supported me, and inspired me to move forward. I offer my profound appreciation and thanks. Whether directly or indirectly, your contributions have helped me achieve this dream.

Contents

Contributions and Conferences:

M. S. Alsayyadi, Z.Cao, B. Salmond, Q. Li, S. Shutts and P. M Smowton, "Developing 1.55 μm quantum dot lasers compatible with epitaxy on silicon substrates", SIOE, UK, 2024.

M.S. Alsayyadi, S.Shutts and P. M. Smowton, "AlGaInAs-InP Laser Operating at 1.55 μm",UK Semiconductors Sheffield, 2023. (Poster).

S. Shutts, Z. Cao, B. Ratiu, O. Abouzaid, M. Alsayyadi, J. Nabialek, ... & P.M. Smowton (2023, March). InAs quantum dots emitting in C and L-wavelength band. In *Novel In-Plane Semiconductor Lasers XXII* (p. PC1244003). SPIE.

Z. Cao, P. Siddham, H.G.-Moys, J. Nabialek, R. Forrest, B. Salmond, M. Alsayyadi, Q. Li, S. Shutts, P. M. Smowton, "1550 nm quantum dot lasers grown on n-InP substrates", SIOE, UK, 2022.

Z. Cao, M. Alsayyadi, B. Salmond, H. Gordon-Moys, J. Nabialek, R. Forrest, ... & P.M. Smowton (2022, November). C-and L-band InAs/InP quantum dot lasers. In *2022 IEEE Photonics Conference (IPC)* (pp. 1-2).

List of Abbreviations

QD	Quantum Dots
QW	Quantum Well
QDH	Quantum dash
InP	Indium Phosphide
InAs	Arsenide Phosphide
GaAs	Gallium arsenide
DWELL	Quantum Dot in a Well system
ASE	Amplified Spontaneous Emission
NF	Near-field
SCM	Segmented Contact Method
SCH	Separate Confinement Heterostructure
MOVPE	MOVPE Molecular vapour phase epitaxy
SRH	Shockley Real Hall
CB	Conduction band

VB	Valence band
DOS	Density of states

Chapter 1: Introduction

1.1 Brief history of semiconductor lasers

Laser devices have been conceived and fabricated in many diverse ways, with arguably the most important being semiconductor diode lasers. It has been more than 60 years since the first semiconductor laser was produced in 1962. A semiconductor laser was considered to be attractive even from its initial emergence, due to the unique features of the laser diode. Of these features, the laser beam, generated by direct electrical pumping through a p-n junction, leads to the production of battery-powered, low cost, compact, coherent light sources. Semiconductor lasers are the most compact and energy-efficient form of laser [1]. The literature is too broad and vast for individual citation. The most important developments in the diode laser structure, and its effect on performance efficiency, can be detailed through the threshold current density (J_{th}) values.

In 1961, Basov and colleagues proposed the concept of a semiconductor laser [2], suggesting that stimulated radiation emission could happen in semiconductors through the recombination of carriers (electrons and holes) injected across a p-n junction. As a result, the first semiconductor laser was developed in 1962, made from a forward-biased GaAs p-n junction [2]. The recombination of electrons and holes in the depletion region of the p-n junction generated optical gain. The p-n junction plane was perpendicular to the parallel polished ends of the laser. In this way a cavity was created which allows feedback, because the polished ends of the crystal behave as partial mirrors. The bulk laser is usually called a laser with a homo-structure. A common and unwelcome feature of homo-structure injection lasers resulted in the threshold current density for lasing being very high at room temperature (RT) (> 50,000 A /cm^2), meaning that continuous RT operation was not feasible. This, coupled with low efficiency, resulted in high heat dissipation, and limited the laser to short pulses at cryogenic temperature. Subsequently, progress was slow for a multitude of reasons. One explanation was that new semiconductor technology was required. Compound

semiconductors were less prominent at this time. In the late 1960s, great strides were made towards solving this issue, and in 1969, heterostructures were introduced. This was relevant as it signified the ability to replace the simple p-n junction with multiple layers of different compositions. Heterostructure lasers can be classified as single or double heterostructure (DH) devices, and graded index (GRIN)-SCH lasers, depending on whether the active region where lasing occurs, is surrounded on one or both sides by a cladding layer of higher band gap.

DH lasers enabled continuous wave (CW) operation at RT, with J_{th} = 5 kA / cm^2, to become possible, and as a result, DH lasers were transferred from the laboratory to industry [3]. The physical cause for the reduction in the threshold current density with use of a DH device is twofold. The active layer is surrounded by two layers of top and bottom cladding, which have a higher band gap and a lower refractive index. The difference in the band gap helps to confine electrons and holes to the active layer, where they recombine to produce the optical gain. The higher bandgap cladding also significantly reduces the internal optical loss [4]. In addition, a dielectric waveguide is formed by the difference in the refractive index, which helps to confine the optical mode close to the active layer. However, this structure on its own does not provide confinement of both light and carriers in the direction parallel to the junction plane [5].

In the 1970s, the stripe geometry heterostructure laser was devised by using a stripe contact to restrict the lateral spread of the injected carriers within the active layer. This laser is often referred to as being gain guided, because it is the lateral variation of the optical gain that limits the optical mode to the electrically pumped stripe. On the other hand, heterostructure lasers where the optical mode confinement occurs mainly through lateral variations in the refraction index are referred to as being index guided. Additionally, at this time, the first quantum well (QW) laser, in which carriers are confined in one dimension, was demonstrated [6]. The advantages over the DH laser included decreased threshold current due to the reduced thickness of the active layer, and the tunability of the wavelength by changing the QW thickness.

While QWs provided excellent carrier confinement, the nanoscale thickness was too thin for effective optical confinement. In the 1990s, an additional two layers were placed outside of the core layers containing the QW layers [2]. These layers had a lower refractive index than the central layers and allowed effective confinement of the optical

field. Such a design is known as a separate confinement heterostructure (SCH) laser diode. Almost all commercial laser diodes since the 1990s have been SCH quantum well laser diodes.

In 1982, Arakawa and Sakaki proposed the concept of a quantum dot (QD) laser [7,8] QDs fabricated by patterning with e-beam lithography, followed by etching, resulting in unsuitable laser structures. The non-radiative recombination due to defects created during the etching process led to a deterioration in the quality of the material.

Self-assembled growth techniques, which can avoid nonradiative defects, were developed [9]. Particularly, the Stranski-Krastanov growth mode was found to be very efficient for the InGaAs/GaAs system. The strain mediated self-organisation of InGaAs/GaAs QDs yield threshold current densities as low as ~60 Acm^{-2} at RT [10,11]. Extensive research has been carried out on the GaAs-based QD system, which has resulted in major improvements in laser performance. An ultra-low threshold current density of 17 Acm^{-2} and high output power has been achieved, and QD lasers are now commercially available on the market. Both Molecular Beam Epitaxy (MBE) and Metal Organic Chemical Vapour Deposition (MOCVD) techniques have been developed and successfully utilised for growing QD materials.

As shown in Figure 1.1, the timeline of semiconductor laser development spans several key milestones, starting with the concept of a GaAs p-n junction in 1962, and culminating in the development of 3D carrier confinement structures in the 2000s.

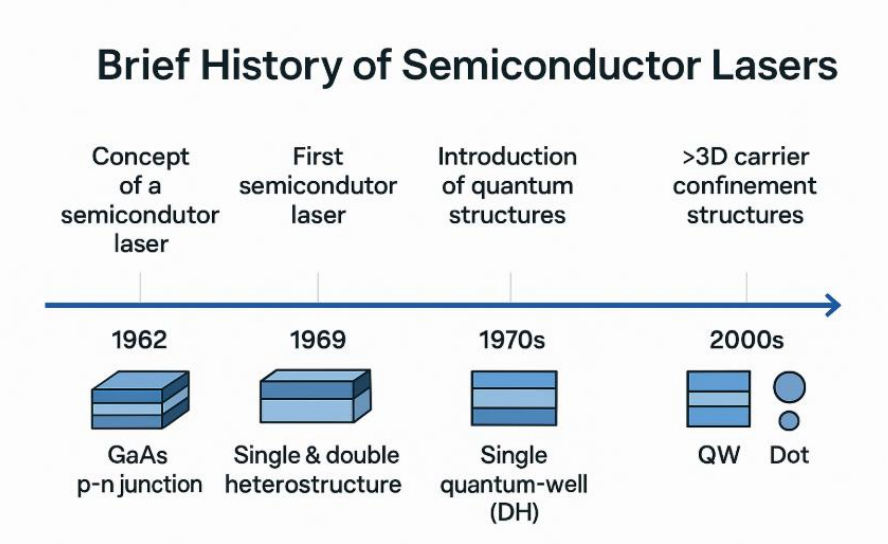

Figure 1.1: Timeline of key developments in semiconductor laser technology, highlighting milestones from the initial concept of a semiconductor laser in 1962, to the introduction of quantum structures in the 1970s, and the advancement of 3D carrier confinement structures in the 2000s.

From the 2000s to the present, laser performance has continued to improve due to advancements in the design of the laser gain medium by using carrier confinement structures with reduced dimensionality such as quantum well (2D) quantum wire (1D), and quantum dot (0D) structures. Nevertheless, semiconductor laser research faces some major challenges such as device size, energy efficiency and system integration. Numerous papers on device design and their effects on injection lasers properties have been published over the last five decades [12,13]. A key aim for many studies is a reduced threshold current density which can lead to more efficient operation of the laser diode [14].

Several orders of magnitude reductions in the threshold current of semiconductor lasers have been achieved since the demonstration of the first semiconductor laser [15]. In particular, numerous studies worldwide have shown substantial improvement in the performance of QD lasers in terms of low threshold current density with lower temperature sensitivity and reliability over their conventional quantum well laser counterparts [16].

1.2 The superior performance of quantum dot lasers

Semiconductor research and device development have seen a progressive reduction in dimensionality from bulk to quantum dots QD, as mentioned in the previous section. Unlike bulk materials, low-dimensional structures, such as QWs, quantum wires, and QDs, exhibit unique properties with localized electrons and discretely quantized energy states. The energy distribution of electrons is dependent on both the density of states and the Fermi-Dirac distribution, which is related to temperature, as explained in Chapter 2. All three different types of low dimensional structures have quantized energy states. QDs represent the last limit in carrier confinement with quantized /discrete energy states and localized carriers. This leads to the theoretical prediction that perfect QD devices can achieve lasers with improved performances [17]. In 1982, Arakawa and Sakaki forecasted that laser devices based on quantum dots would exhibit complete insensitivity to temperature, enabling them to function without the need for temperature control systems [18]. Then, in 1986, Asada forecasted that quantum dot lasers would provide a gain approximately ten times higher than that of bulk materials [19]. These predictions suggested the potential for nearly ideal laser devices. As a result, they sparked significant interest in the advancement of quantum dot technologies.

In a quantum well, the carriers are confined in one dimension, which results in a two-dimensional density of states with a step-like function of energy. Compared to bulk material, this structure leads to a relatively higher population of states at a given energy level, which means that more electrons and holes can be available to radiatively recombine at a given transition energy, allowing for larger gain. Quantum dots are zero-dimensional, meaning that carriers are confined in all three dimensions. The ideal QD has a delta-function density of states and means QD lasers need fewer carriers for population inversion, resulting in a low threshold and higher differential gain [20]. Since the energy levels are fully discretised, the QD gain should not be significantly influenced by the temperature-dependent Fermi-Dirac distribution. However, as seen later, the QDs predicted temperature stability and high gain are not usually achieved in practice.

Quantum dot lasers are less sensitive to defects compared to quantum well lasers because of the carrier localization. A defect passing through the active region will only interact with a small number of quantum dots, leaving most of them unaffected [21].

III–V compound semiconductors are alloys composed of elements from groups III and V of the periodic table. Common binary compounds include GaAs, InP, and InAs. By partially substituting atoms in a binary crystal with different group III or V elements, ternary compounds (such as InGaAs) and quaternary compounds (such as InGaAsP and InAlGaAs) can be formed. This compositional flexibility enables precise engineering of both the lattice constant and the bandgap energy of III–V materials. Figure 1 illustrates the relationship between the bandgap energy, lattice constant, and corresponding emission wavelength for various III–V semiconductors.

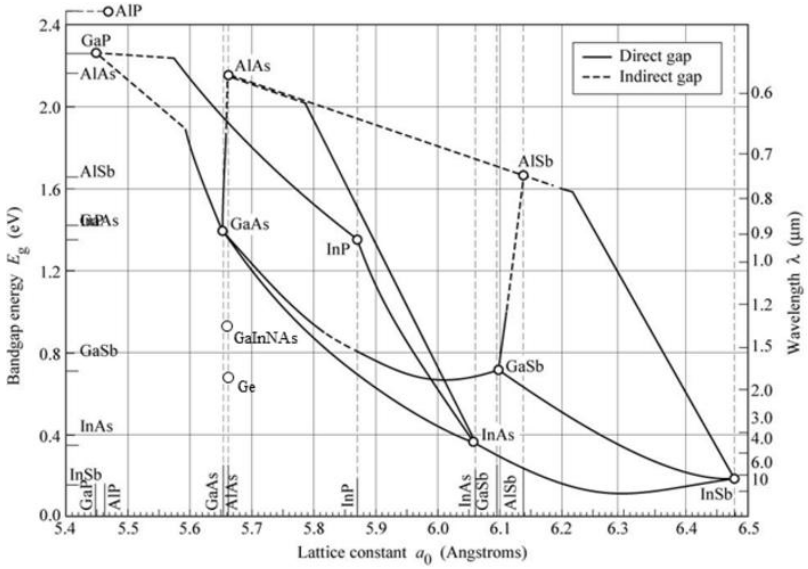

Figure 1.2: Band gap energy E_g as a function of lattice constant a_0 for III–V semiconductors [22].

The ability to tailor these properties, along with the compatibility of III–V materials for monolithic integration, makes them highly promising for advances in III–V photonics, as will be discussed in the following section.

In this study, the focus will be on indium arsenide (InAs) quantum dots grown on indium phosphide (InP), with gallium arsenide (GaAs) -based InAs quantum dots considered for comparison.

The $In_xGa_{1-x}As_yP_{1-y}$ quaternary alloy system is widely used in optoelectronic devices due to its highly tunable band gap energy and lattice constant. By varying the composition of indium, gallium, arsenic, and phosphorus, the material properties can be precisely engineered to meet the requirements of specific applications, such as lasers operating at telecommunication wavelengths (1.3 μm and 1.55 μm). The ability to independently adjust both the electronic and structural properties allows InGaAsP to be lattice-matched to an InP substrate, minimizing defects and improving device performance. From Figure 1.2, it is evident that the band gap energy decreases with increasing lattice constant, corresponding to higher indium and arsenic concentrations. This tunability allows InGaAsP alloys make it possible to design them for targeted wavelength emissions, especially near 1.3 μm and 1.55 μm, key wavelengths for efficient fiber optic communications. By precisely tuning the composition while ensuring lattice compatibility with the InP substrate, it is possible to produce high-performance devices with low defect densities and excellent optical characteristics.

The lattice mismatch between GaAs and InAs is 7.2% [23]. On this system, many reports of laser devices have been achieved, and some of the predicted advantages for QD lasers, such as lower threshold current density [24], reduced sensitivity of the threshold current density to temperature [25], and the extension of the emission wavelength achievable on GaAs have been demonstrated. The majority of reports of QD lasers have been achieved on GaAs substrates, with laser wavelengths ranging from 1 μm to 1.3 μm.

Nevertheless, longer wavelengths, for example the C band (1530 nm to 1565 nm) used in long-reach optical communication networks, are required. Using InP substrates allow an extension of the emission wavelength beyond 1.55 μm. However, the lattice mismatch between InAs and InP is about half the value of InAs and GaAs. Due to the lower lattice mismatch and strain anisotropy, the formation of nanostructures on InP is much more complex than on GaAs. This leads to the formation of either a high density of dots elongated in the lattice direction (commonly referred to as dashes) or a low density of large dots, depending on the growth conditions [26–28]. Due to these subtle

differences, most devices operating on InP substrates are optimized for longer wavelength emissions. Because of the smaller band gap in InAs/InP systems, devices can emit at telecom wavelengths (1.3 μm – 1.6 μm), making InP-based systems ideal for fiber optic communications. Using InP substrates, the material system—particularly InAs quantum dots grown on InP—naturally supports the emission of longer wavelengths of light (e.g., >1.55 μm), which is important for telecom applications like the C-band. This is primarily due to the material band gap: InAs has a small band gap (~0.36 eV), and when combined with InP, the resulting band structure allows the quantum dots to emit lower-energy photons, i.e., longer wavelengths. The lattice mismatch between InAs and InP is smaller than that between InAs and GaAs, which affects quantum dot formation. On GaAs, more uniform dots can be formed more easily, while on InP, the formation process is more complex, often leading to either elongated quantum dots (dashes) or large, sparsely distributed dots. These nanostructure differences influence the electronic energy levels within the quantum dots, which in turn affects the wavelength of emitted light. In essence, the choice of InP substrates and InAs quantum dots enables long-wavelength emission due to the interaction of their band structures and strain profiles, but these same differences make growth and control more challenging, which is why this remains an active area of research. InAs on InP quantum dot lasers have already been demonstrated and reported in the literature. However, several key questions remain unanswered, such as the precise growth conditions that favour the formation of dots versus dashes, and the performance limitations associated with each. Addressing these uncertainties is the main motivation for this research.

1.3 Integration of III-V lasers on Silicon substrates

Silicon has an important role in electronic devices due to its electronic properties and can also be used for passive optical devices. Silicon (Si) is abundant on earth; thus, making it cheap, and has good thermal and mechanical properties. Additionally, it possesses an insulating native oxide (SiO_2), which can be used to create optical waveguides. However, it is not suitable as an efficient light emitter because silicon has an indirect band gap, as will be discussed further in Chapter 2.

Si-based photonic integrated circuits (PICs) have wide applications in optical communication, light detection and ranging (LIDAR), bio-photonics, and mid-infrared sensing. Especially in datacom and telecom communication, silicon photonics has attracted intense interest driven by the unprecedented data capacity in global network traffic. Silicon photonics complement metal-oxide-semiconductor (CMOS) fabrication processes. However, because electrically pumped silicon lasers, which are the most important building blocks in silicon photonics, are difficult to realize, many alternatives are under intensive study.

On the other hand, III–V semiconductors like GaAs and InP have unique electronic and optical properties, including higher intrinsic mobility of electrons and lower effective electron mass compared to Si and Ge, making them very suitable for high-speed electronics. In photonic applications, they can efficiently produce light because many III–V compounds are direct band gap materials [29]. However, they are subject to some difficulties in product manufacturing with weak mechanical features. III-V materials are more fragile than Si and therefore the wafers are typically smaller than Si. In addition, these materials are less abundant, and thus, they are expensive compared to Si. As a result of these properties, the integration between III-V semiconductors and silicon, as a promising integration platform, is the best solution to combine their benefits. Combining Si substrates with compound semiconductors should enable higher optoelectronic functionality and at larger scale than typically used with compound semiconductors on their own [29]. The next section reviews the main methods of integration of III–V materials on Si.

1.4 Approaches for III-V and Si integration:

The development of photonic integrated circuits PICs has progressed through two main approaches: hybrid and monolithic integration. The hybrid approach involves growing III-V components, such as GaAs or InP, on their native substrates and then transferring them to silicon. The transfer process includes bonding III-V semiconductor devices, such as lasers, onto silicon wafers, which enables the use of high-performance components without the complexities of directly growing III-V materials on silicon. Although this method provides flexibility, and simplifies integration by avoiding heteroepitaxial growth, it has some limitations. These include the need for precise alignment during bonding, which can be complex and costly, as well as thermal and mechanical mismatches between III-V materials and silicon, which can affect the overall reliability of the integrated system.

The second approach is monolithic integration by heteroepitaxy. Monolithic integration involves growing III-V materials directly on silicon wafers using methods such as Metal-Organic Chemical Vapor Deposition (MOCVD) or Molecular Beam Epitaxy (MBE), even in the face of lattice mismatch. This integration method results in higher integration density, reduced manufacturing costs by utilizing standard silicon processes, and enhanced scalability and thermal management. However, the major challenge is the lattice mismatch between silicon and III-V materials, which can create defects such as dislocations that impair device performance [30].

Despite these challenges, significant advancements have been made, particularly with QD lasers, which demonstrate superior defect resistance compared to quantum well lasers. QD lasers, due to their better carrier localization and resistance to defects such as threading dislocations, have emerged as strong candidates for monolithic integration with silicon.

Recent progress has focused on improving the epitaxial growth of QDs on silicon, minimizing defects, and enhancing the performance of integrated photonic systems. Consequently, QD lasers are becoming a promising solution for monolithic silicon integration, enabling scalable and high-performance PICs suitable for industrial applications.

1.5 Quantum dot lasers and III–V/ Si integration

The integration of quantum dot lasers with silicon photonics represents a significant development in optoelectronic devices. By epitaxially growing InAs/GaAs and InAs/InP quantum dots on silicon, researchers are overcoming challenges in integrating III-V materials onto Si platforms. This technology aims to improve the efficiency and scalability of silicon photonic circuits, linking optical and electronic components in an effective way.

1.5.1 InAs/GaAs QDs Lasers epitaxially grown on silicon

The development of InAs/GaAs quantum dot lasers epitaxially grown on silicon has seen significant advancements in reducing threshold current density and increasing maximum lasing temperature. The University of Michigan was the first to demonstrate the operation of a quantum dot laser grown on silicon, achieving pulsed lasing at 80 K with a high threshold current density of 3.85 kA/cm² in 1999 [31]. Subsequent innovations, including strained-layer superlattice (SLS) dislocation filters, dot-in-well (DWELL) structures, and optimized nucleation layers, significantly improved performance. Then, in 2014, record-breaking performance was achieved with 1.3 μm InAs quantum dot lasers epitaxially grown on silicon, demonstrating low threshold currents (16 mA), high continuous-wave output power (176 mW), elevated lasing temperatures (up to 119 °C), and a high characteristic temperature (T_0 > 200 K). [32]. Later, in 2016, UCL and Cardiff achieved a milestone by reporting the lowest threshold current density for room-temperature operation [33]. Recent methods, such as antiphase boundary (APB)-free GaAs films and innovative silicon-patterning techniques, enabled defect suppression, enhanced thermal performance and the development continues to this day, making it challenging to enumerate all the contribution in this field that highlight the promise of QD lasers as reliable, cost-effective solutions for silicon photonics integration [34–37] .

1.5.2 InAs/InP QDs Lasers epitaxially grown on silicon:

InAs/InP quantum dot lasers epitaxially grown on silicon offer significant potential for optical communication at the 1.55 μm wavelength, but their development faces notable

challenges. Although the lattice mismatch between InAs and InP is relatively small (~3%) compared to InAs/GaAs systems (~7%), this does not necessarily simplify quantum dot formation. Instead, the reduced strain energy and differing surface kinetics on InP often lead to the formation of elongated quantum dashes rather than uniform quantum dots, accompanied by large size and shape dispersion, inhomogeneous broadening, and elevated threshold current densities. Furthermore, integrating InP onto silicon is inherently difficult due to a significant lattice mismatch (~8%), which is roughly twice that of GaAs to Si, along with mismatches in thermal expansion coefficients and the challenges of polar-on-nonpolar epitaxy. These issues contribute to high defect densities that further impact device performance and reliability.

Strategies to overcome these growth challenges include using dislocation filters, thin intermediate buffers like GaAs, and nano-patterned V-groove substrates to reduce defects and improve crystalline quality. Progress in epitaxy, buffer engineering, and device design, demonstrated by recent efforts from Matsumoto et al., Zhu et al., and Shi et al. [38–41], have shown promising results, such as room-temperature lasing and improved threshold current densities

However, further optimization of growth techniques and laser structures is essential to reduce defects, improve optical gain, address internal optical losses, and enhance performance to achieve reliable, high-performance monolithic integration with silicon photonics.

1.6 Current status and scope of the research

Further research into enhancing the material quality, reliability, and overall performance of InAs/InP QD lasers is essential to make them competitive with InAs/GaAs systems. This progress is particularly critical for meeting the growing demand for high-performance optical devices, especially for C-band applications in optical communication. Such advancements will ultimately facilitate the seamless integration of these lasers into silicon photonic circuits. Despite the challenges, the initial development of electrically pumped InAs/InP QD lasers on native InP substrates is an important goal, and it serves as the focus of the present study.

1.7 Aims of Research

The aim is to develop high-quality InP-on-Si substrates for silicon photonics by improving InAs/InP quantum dots (QDs) to minimize threshold current density and enhance temperature stability of InAs QDs on InP lasers with operation wavelengths in the C- and L-bands (1530-1625nm). The primary focus will be on optimizing active materials to help create improved lasers for integrated optoelectronic devices.

The objectives are:

1-Provide a benchmark for the study using AlGaInAs/InP quantum well oxide-isolated stripe lasers.

2-Evaluate an idea for an electron blocking layer for use in such lasers.

3. Investigate the performance and potential of InAs/InP quantum dot/dash lasers.

4. Develop the design and characterization of 1.55 μm InAs/InP quantum dot lasers, specifically analyzing how the capping layer influences dot formation and studying the development of gain materials. Understanding the influence of subtle design changes such as in the capping layer is important for developing InAs/InP QDs that can be grown reproducibly and that perform well in QD-based lasers and integrated devices.

Work will involve analyzing various structures, measuring key parameters including as a function of temperature, and examining gain and absorption spectra.

1.8 Thesis Structure

The remainder of this thesis is organized as follows: the second chapter provides a general overview of key concepts related to semiconductor lasers and some of the analysis that I will use later in the thesis. It discusses various types of confinement structures in lasers, including current confinement, carrier confinement, and optical confinement. Important operating parameters such as the threshold current, optical loss, and external and internal quantum efficiencies of a semiconductor laser are introduced. The chapter concludes with an overview of quantum dot systems. The third

chapter describes the experimental equipment and set-up used to investigate the laser structures analyzed in this thesis. The fourth chapter presents an experimental study on the characterization of 1.5 μm AlGaInAs/InP quantum-well lasers to provide an indication of the performance that the QD lasers need to demonstrate. It examines structures with two different numbers of quantum wells QWs in the active region through initial measurements and their interpretation at room temperature.

The fifth chapter focuses on the design of multiple-QW (MQW) AlGaInAs/InP 1.55 μm lasers incorporating an AlInGaAs barrier and waveguide, along with an additional electron stopper layer on the p-side. Using the Next Nano software package, simulations were performed to compare structures with and without electron stopper layer, monitoring leakage current density as a function of Fermi-level separation, which serves as an indicator of optical gain. The sixth chapter presents an experimental study on the dependence of threshold current on temperature in InAs quantum dot-based lasers on InP. Gain and absorption measurements using the multi-section method are also introduced in this chapter. The seventh chapter presents an experimental study of InAs/InP (100) Quantum Dot lasers, focusing on key parameters such as the threshold current, gain coefficient, internal loss, and quantum efficiency. Experimental investigations on the threshold current and sensitivity to temperature are also discussed. Additionally, gain and absorption measurements are presented. The eighth chapter provides an overall summary of the thesis and offers suggestions for future research.

References

1. Ning, C.-Z. Semiconductor nanolasers and the size-energy-efficiency challenge: a review. *Advanced Photonics* 1, 14002 (2019).

2. Agrawal, G. P. & Dutta, N. K. *Semiconductor Lasers*. (Springer Science & Business Media, 2013).

3. Uchiyama, S., & Iga, K, Consideration on Threshold Current Density of GaInAsP/InP Surface Emitting Junction Lasers. *IEEE Journal of Quantum Electronics*, 22 302-309 (1986).

4. Chow, W. W. & Koch, S. W. *Semiconductor-Laser Fundamentals: Physics of the Gain Materials*. Springer Science & Business Media, (2013).

5. Wang, T., Liu, H., Lee, A., Pozzi, F. & Seeds, A. 1.3-μm InAs/GaAs quantum-dot lasers monolithically grown on Si substrates. *Optics express,* 19(12), 11381–11386 (2011).

6. Grave, I., Kan, S. C., Griffel, G., Wu, S. W., Sa'Ar, A., & Yariv, A. Monolithic integration of a resonant tunneling diode and a quantum well semiconductor laser. *Applied Physics Letters* 58, 110–112 (1991).

7. Chow, W. W. & Koch, S. W. *Semiconductor-Laser Fundamentals: Physics of the Gain Materials*. Springer Science & Business Media, (2013).

8. Michon, A., Patriarche, G., Beaudoin, G., Saint-Girons, G., Gogneau, N., & Sagnes, I. Density of InAs⁄ InP (001) quantum dots grown by metal-organic vapor phase epitaxy: Independent effects of InAs and cap-layer growth rates. *Applied Physics Letters* 91, (2007).

9. Arakawa, Y., Nakamura, T. & Kwoen, J. Quantum dot lasers for silicon photonics. in *Semiconductors and Semimetals* vol. 101 91–138. Elsevier, (2019).

10. Casey, H. C. & Panish, M. B. *Heterostructure Lasers*. vol. 1. Academic press, (1978).

11. Casey, H. C., Somekh, S. & Ilegems, M. Room-temperature operation of low-threshold separate-confinement heterostructure injection laser with distributed feedback. *Applied Physics Letters* 27, 142-144 (1975).

12. Gunnarsson, W. B., Roh, K., Zhao, L., Murphy, J. P., Grede, A. J., Giebink, N. C., & Rand, B. P. Toward Nonepitaxial Laser Diodes. *Chemical Reviews* vol. 123 7548-7584. doi.org/10.1021/acs.chemrev.2c00721 (2023).

13. Mawst, L. J., Tansu, N. & Rahman, A. Quantum-Well Lasers and Their Applications. in *Reference Module in Materials Science and Materials Engineering*. Elsevier, (2016). doi:10.1016/b978-0-12-803581-8.00825-0.

14. Baranov, A. & Tournié, E. *Semiconductor lasers: Fundamentals and applications*. Elsevier. (2013).

15. Chen, S., Liao, M., Tang, M., Wu, J., Martin, M., Baron, T., Seeds, A. & Liu, H., Electrically pumped continuous-wave 1.3 μm InAs/GaAs quantum dot lasers monolithically grown on on-axis Si (001) substrates. *Optics express*, 25(5), pp.4632- 4639 (2017).

16. Kageyama, T., Nishi, K., Yamaguchi, M., Mochida, R., Maeda, Y., Takemasa, K., Tanaka, Y., Yamamoto, T., Sugawara, M. & Arakawa, Y. Extremely high temperature (220 C) continuous-wave operation of 1300-nm-range quantum-dot lasers. in The European Conference on Lasers and Electro-Optics PDA_1. *Optica Publishing Group*, (2011).

17. Chen, T. & Liu, Y. *Semiconductor Nanocrystals and Metal Nanoparticles: Physical Properties and Device Applications*. CRC Press. (2016).

18. Arakawa, Y. & Sakaki, H. Multidimensional quantum well laser and temperature dependence of its threshold current. *Applied Physics Letters* 40, 939-941 (1982).

19. Asada, M., Miyamoto, Y. & Suematsu, Y. Gain and the Threshold of Three-Dimensional Quantum-Box Lasers. *IEEE Journal of quantum electronics,* 22(9), 1915-1921. (1986).

20. Shi, B. *Epitaxial Growth of III-V Quantum Dot Lasers on Silicon Substrates*. Hong Kong University of Science and Technology. Hong Kong, 2018).

21. Zhu, S., Shi, B. & Lau, K. M. Electrically pumped 1.5 μm InP-based quantum dot microring lasers directly grown on (001) Si. *Optics letters,* 44(18), 4566-4569, (2019).

22. Jain, P., & Honnungar, R. V. (2022). A review on materials for integrated optical waveguides. In Proceedings of Fourth International Conference on Inventive Material Science Applications: ICIMA 2021 (pp. 55-66). Springer Singapore.

23. Tsai, Y. L., Fang, J. H. & Wu, C. H. A novel coalesced quantum dot buffer approach to mitigate large lattice mismatch in III-V epitaxy. *AIP Advances,* 14(11), (2024).

24. Shi, B., Han, Y., Li, Q. & Lau, K. M. 1.55-μm lasers epitaxially grown on silicon. *IEEE Journal of Selected Topics in Quantum Electronics* 25, 1-11 (2019).

25. Yang, W., Li, Y., Meng, F., Yu, H., Wang, M., Wang, P., Luo, G., Zhou, X. & Pan, J. III–V compound materials and lasers on silicon. *Journal of Semiconductors* .40(10), 101305 (2019).

26. Grillot, F., Duan, J., Dong, B. & Huang, H. Semiconductor quantum dot lasers: Genesis, prospects, and challenges. in *Quantum Photonics* 191-266. *Elsevier*, 2024). doi:10.1016/B978-0-323-98378-5.00008-8.

27. Paranthoen, C., Bertru, N., Dehaese, O., Le Corre, A., Loualiche, S., Lambert, B. & Patriarche, G. Height dispersion control of InAs/InP quantum dots emitting at 1.55 μm. *Applied Physics Letters, 78(12),* 1751-1753 (2001).

28. Yadav, A., Chichkov, N. B., Avrutin, E. A., Gorodetsky, A. & Rafailov, E. U. Edge emitting mode-locked quantum dot lasers. *Progress in Quantum Electronics* vol. 87. doi.org/10.1016/j.pquantelec.2022.100451 (2023).

29. Kwoen, J., Jang, B., Watanabe, K. & Arakawa, Y. High-temperature continuous-wave operation of directly grown InAs/GaAs quantum dot lasers on on-axis Si (001). *Optics express* 27(3), 2681–2688 (2019).

30. Lee, A., Jiang, Q., Tang, M., Seeds, A. & Liu, H. Continuous-wave InAs/GaAs quantum-dot laser diodes monolithically grown on Si substrate with low threshold current densities. *Optics express* 20(20), 22181-22187 (2012).

31. Linder, K.K., Phillips, J., Qasaimeh, O., Liu, X.F., Krishna, S., Bhattacharya, P. & Jiang, J.C., Self-organized In 0.4 Ga 0.6 As quantum-dot lasers grown on Si substrates. *Applied physics letters* 74(10), 1355-1357 (1999).

32. Liu, A.Y., Zhang, C., Norman, J., Snyder, A., Lubyshev, D., Fastenau, J.M., Liu, A.W., Gossard, A.C. & Bowers, J.E. High-performance continuous wave 1.3 μm quantum dot lasers on silicon. *Applied Physics Letters 104(4)*, (2014).

33. Chen, S., Li, W., Wu, J., Jiang, Q., Tang, M., Shutts, S., Elliott, S. N., Sobiesierski, A., Seeds, A, J., Ross, I., Smowton, P. M., & Liu, H. Electrically pumped continuous-wave III-V quantum dot lasers on silicon. *Nature photonics* 10(5), 307-311 (2016). doi .10.1038/nphoton.2016.21

34. Zhu, S., Shi, B., Li, Q. & Lau, K. M. 1.5 μm quantum-dot diode lasers directly grown on CMOS-standard (001) silicon. *Applied Physics Letters* 113(22), (2018).

35. Tang, M., Chen, S., Wu, J., Jiang, Q., Dorogan, V.G., Benamara, M., Mazur, Y.I., Salamo, G.J., Seeds, A. & Liu, H. 1.3-μm InAs/GaAs quantum-dot lasers monolithically grown on Si substrates using InAlAs/GaAs dislocation filter layers. *Optics express* 22(10), 11528-11535 (2014).

36. Liao, M., Chen, S., Park, J.-S., Seeds, A. & Liu, H. III–V quantum-dot lasers monolithically grown on silicon. *Semiconductor Science and Technology* 33, 123002 (2018).

37. Wei, W.-Q., Wang, T. & Zhang, J.-J. InAs QDs monolithically grown on CMOS compatible Si (001) and SOI platform with strong emission at 1300 nm

and 1550 nm. in *2019 IEEE 16th International Conference on Group IV Photonics (GFP)* 1-2 *IEEE*, (2019).

38. Shi, B., Han, Y., Li, Q. & Lau, K. M. 1.55-μm lasers epitaxially grown on silicon. *IEEE Journal of Selected Topics in Quantum Electronics,* 25(6), 1-11 (2019).

39. Zhu, S., Shi, B. & Lau, K.M., Electrically pumped 1.5 μm InP-based quantum dot microring lasers directly grown on (001) Si. Optics letters, 44(18),.4566-4569. (2019).

40. Abdollahinia, A., Banyoudeh, S., Rippien, A., Schnabel, F., Eyal, O., Cestier, I., Kalifa, I., Mentovich, E., Eisenstein, G. & Reithmaier, J.Á. Temperature stability of static and dynamic properties of 1.55 μm quantum dot lasers. *Optics express,* 26(5), 6056-6066 (2018).

41. Matsumoto, K., Zhang, X., Kishikawa, J. & Shimomura, K. Current-injected light emission of epitaxially grown InAs/InP quantum dots on directly bonded InP/Si substrate. *Japanese Journal of Applied Physics,* 54(3), 030208 (2015).

Chapter 2: Background theory

2.1 Introduction

This chapter provides the theoretical foundation required to comprehend the research presented in this thesis. It commences with an overview of essential principles concerning semiconductor lasers, starting with an introduction to semiconductor band structures. This is followed by an exploration of optical transitions and recombination mechanisms within semiconductors. The impact of confinement structures on semiconductor lasers is also examined. Furthermore, the characterization of quantum well and quantum dot lasers is discussed.

2.2 Semiconductors band structure

The fundamental band structure consists of two energy bands. One band is filled with electrons, and this band is called the valence band (VB). The other group is empty of electrons, and this band is called the conduction band (CB). Electron states with energies between the valence band edge energy (Ev) and the conduction band edge energy (Ec) are forbidden and this energy range is called the bandgap energy (Eg), as shown in Figure 2.1 [1]

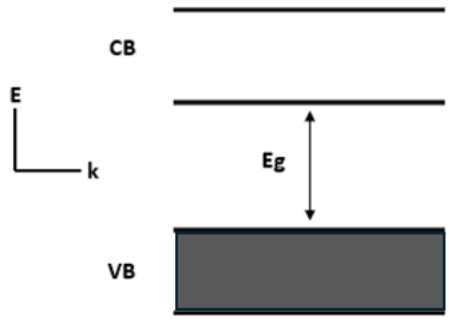

Figure 2.1: Simplified diagram of semiconductor band structure showing the valence band (VB), conduction band (CB), and the bandgap energy (Eg).

Adding energy to a system whether thermal energy, optical energy, or another form can excite electrons from the valence band to the conduction band, creating holes in the valence band and conduction electrons in the conduction band. When optical energy is involved, a photon must have energy greater than or equal to the bandgap energy to excite an electron across the bandgap. On the other hand, when thermal energy is considered, and the material is in thermal equilibrium, electrons will follow a specific energy distribution described by the Fermi-Dirac distribution. At temperatures above absolute zero, some electrons will have sufficient thermal energy to be excited to the conduction band. The energy level that characterizes this statistical distribution of electrons is known as the Fermi energy. Any transition of electrons between the valence band and conduction band is controlled by energy conservation and momentum. This can be illustrated on the plot of electron energy versus k for a semiconductor material shown in Figure 2.2. Compared to the momentum of the conduction electrons and holes in the semiconductor, photons carry negligible momentum. Thus, for optical transitions where only photons are involved, this means the transition between the conduction band and valence band must have the same wavenumber vector, so the only optical transitions that occur on this diagram are the vertical transitions. Electrons make a downward transition and lose their energy to an emitted photon. Transitions can also involve phonons. Phonons carry momentum comparable to the crystal momentum of the electron and holes, so there may be transitions which aren't just downward. Photon emission is essential in the technology of optoelectronic devices such as lasers. [2,3]

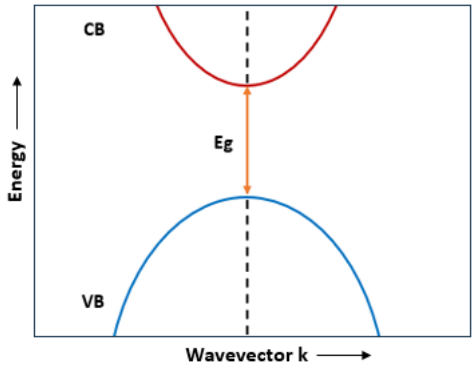

Figure 2.2: The optical transition of electron and hole between conduction and valance band is allowed only in vertical direction.

The energy, E, of electrons and holes near the band edges of the conduction and valence bands can be roughly estimated as [4] $E = \frac{\hbar^2 k^2}{2m^*}$, where $\hbar$ is the Planck constant divided by 2π, k represents the wave vector, and m^* is the effective mass of the carrier within a band.

2.3 Energy band gap

The energy bandgap is defined as the energy range in a solid where no electron states can exist. From the bandgap energy diagram, the bandgap energy generally refers to the energy difference between the top of the valence band and the bottom of the conduction band in insulators and semiconductors [5], as shown in Figure 2.1. Typically, the energy is given in electron volts. The electrons that gain energy greater than the bandgap can escape from the valence band and move into the conduction band. In this band, they move freely throughout the crystal lattice and are directly involved in the conductivity of semiconductors. The empty states that are left behind by the conduction electron carry a net positive charge and are referred to as holes.

To calculate the temperature-dependent bandgap energy E_g of a semiconductor material or alloy, the model of Varshni [6] is used. This is written as

$$E_g = E_{g,0} - \frac{\alpha T_L^2}{\beta + T_L} \qquad (2.1)$$

where $Eg_{,0}$ is the bandgap energy at zero kelvin, α and β are fitting parameters, and T_L is the temperature.

2.4 Direct and indirect band gap semiconductor

The energy band gap has been defined as the minimum energy difference between top of valence band and bottom of conduction band. The maximum value of valence band and the minimum value of the conduction band do not always exist at the same value of the crystal momentum p, which is related to the wave number k as [1].

$$k = \frac{p}{\hbar} \qquad (2.2)$$

where $\hbar$ is the reduced Planck constant.

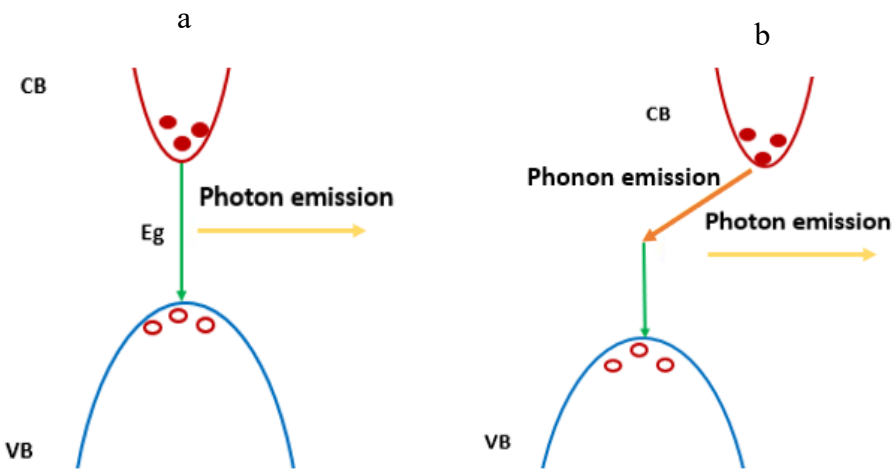

Figure 2.3 (a) Direct band gap and (b) Indirect band gap.

When the valence band maximum happens at the same momentum, k, as the conduction band minimum, the semiconductor is known as a direct band gap semiconductor, as shown in Figure 2.3 a. It is important for radiative recombination, where an electron in the in the lowest energy state in the conduction band can recombine with a hole in the highest energy state in the valence band without a change in the crystal momentum value. The transition energy is then released as a photon. However, when the upper and the lower electronic states of the valence and conduction bands, respectively, do not occur at same crystal momentum value, the semiconductor is known as an indirect band gap semiconductor, as shown in Figure 2.3 b. In this case, an electron cannot transition between the highest energy state in the valence band and the lowest energy state in the conduction band, without a change in the crystal momentum value. For radiative recombination to happen in an indirect band gap material, the process must also involve the absorption or emission of a phonon in order to conserve momentum, where the difference between the electron and hole momentum equals the phonon momentum. An electron in the upper state cannot relax to the valence band, and recombine with a hole, until a phonon with the right momentum is present. Electrons in the upper states may also lose energy by non-radiative recombination with the energy being dissipated as heat. Although phonons can provide the necessary momentum conservation to allow electrons to radiatively recombine with holes, this three-particle interaction is not as probable in comparison

with the radiative transition in direct bandgap semiconductors. This means that the radiative recombination rates are typically small in comparison to the undesired non-radiative recombination. Therefore, in direct bandgap materials such as GaAs and InP, radiative recombination happens on a shorter timescale and more efficiently, by a simple two particle process. This is the reason why laser diodes and light emitting diodes are made from direct band gap materials, and not indirect band gap such as silicon [7].

2.5 Temperature Dependence of Semiconductor Materials

In bulk semiconductors, the bandgaps of both direct and indirect semiconductors are impacted by temperature. This relationship can be expressed using the empirical Varshni formula Equation (2.1) [6] . This formula shows that as temperature rises, the bandgap of the material tends to decrease. This effect is primarily due to the thermal expansion of the crystal lattice, which leads to a reduction in the bandgap. Meaning at higher temperatures, the ions that make up the crystal lattice gain more kinetic energy, causing the average distance between them to increase (thermal expansion). As the electronic states associated with each ion move further apart, the energy splitting tends to decrease.

2.6 Lattice Constants and Lattice Matching

The lattice constant of a solid corresponds to the dimensions of the conventional unit cell at equilibrium. It has been widely studied for many materials and obtained experimentally using X-ray diffraction techniques [8]. The lattice constant is normally dependent on both temperature and pressure [9]. It is also noted that the lattice constant is influenced by the crystalline quality, such as impurities, dislocations, and surface damage [10]. Typically, the lattice constant of semiconductor crystals is approximately several angstroms.

Lattice Matching

In order to avoid any defects in the structure during the growth processes of thin layers of materials grown on top of one another, lattice matching should be taken into account. When the lattice constant differs between the layers, a strain will exist, and that may lead to the epitaxial growth of layers containing defects [11]. Lattice matching is defined as the matching in lattice constant between two different semiconductor materials, and this is the ideal scenario, where the bandgap energy can be changed without a change in the lattice constant. This typically requires quaternary alloys (InAlGaAs or InGaAsP) for the InP material system and is often required for structures suitable for optoelectronic devices such as laser diodes [12]. When the strain or the percentage difference between the lattice constants of two different materials is much less than 0.1%, then the lattice match is considered to be achieved. However, if the strain is more than that, then the material is lattice mismatched [13]. Lattice mismatch refers to the difference in lattice constants between an epitaxial film and its substrate. When this mismatch or strain is less than about 0.1%, the materials are typically considered lattice-matched, as the strain can be elastically accommodated without introducing significant defects. However, when the mismatch exceeds this threshold, the strain energy in the growing film increases with thickness, this ultimately makes it energetically favorable for the system to alleviate the strain by forming misfit dislocations. The Matthews and Blakeslee model quantitatively describes this behavior, introducing the concept of critical thickness (h_c), which is the maximum thickness at which an epitaxial film can remain coherently strained without defect formation. As the lattice mismatch increases, the critical thickness h_c decreases rapidly. Therefore, the 0.1% mismatch guideline corresponds to a regime where the critical thickness is large enough for typical epitaxial films to remain coherently strained and defect-free. Beyond this threshold, misfit dislocations are more likely to form, signaling a transition to a lattice-mismatched system. The critical thickness h_c is influenced by factors such as the lattice mismatch, the elastic properties of both the film and substrate, and the film's thickness. The critical thickness can be expressed by the formula $h_c = \frac{C}{\Delta_a}$, where C is a constant and Δ_a is the lattice mismatch. A larger mismatch results in a smaller h_c meaning dislocation will form thinner film

thicknesses. Understanding and controlling this Critical thickness is essential for designing high-quality films, as exceeding this threshold can degrade the film's properties.

The interest of better semiconductor laser performance has led to the use of strain within their structure. Contrary to the original belief that strain-free materials were ideal, researchers found that adding small amounts of strain to the active layer of semiconductor lasers could enhance their performance [14] . Since then, incorporating strain has yielded substantial improvements and enabled the production of very high-performance devices [15].

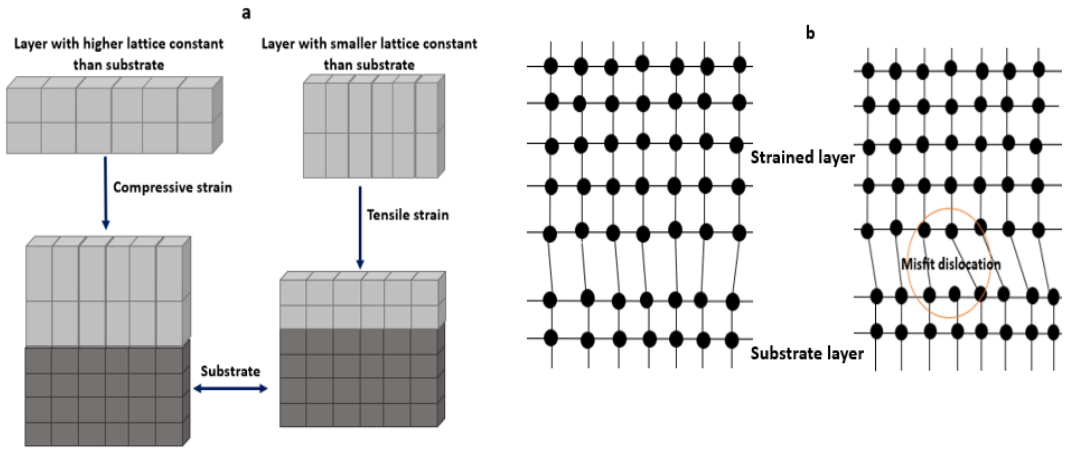

Figure 2.4. a) Comparison of a compressive and tensile strained layer on a substrate, and b) the deposited material and the substrate with a coherent interface (left) and an interface with a misfit dislocation due to strain relaxation (right).

The degree of strain (ϵ_m) between the layer with lattice constant (a_L) and the substrate with lattice constant (a_s) is expressed as follows, [16]

$$(\epsilon_m\ \%) = \frac{a_L - a_s}{a_s} \qquad (2.3)$$

The mismatch between the lattice constants of a layer a_L and a substrate a_s in epitaxial growth induces built-in strain. If the layer is very thin, the strain can be adapted

elastically without forming dislocations, up to a critical thickness. Beyond this critical thickness, misfit dislocations can occur.

Semiconductor lasers experience two types of strain. Compressive strain arises when the lattice constant of the epilayer is larger than that of the substrate, causing the material to stretch in the growth direction. In contrast, tensile strain occurs when the epilayer's lattice constant is smaller than that of the substrate, leading to stretching in the plane, as shown in Figure 2.4.a.

Strain that can be accommodated elastically is termed coherent strain, whereas strain managed by dislocations is called relaxed strain. In Si integrated photonics, the large mismatch between III-V materials and Si-substrates necessitates buffer wafers to relieve strain in the III-V quantum dot layers for monolithic integration on Si. In Figure 2.4.b (left), the picture shows no strain relief in the deposited material that is lattice matched to the substrates. The right shows that the strain caused by a small mismatch between the layers can be accommodated as a defect.

2.7 Radiative Transitions in Semiconductor Lasers

In semiconductor lasers, electrons can transition between the conduction band and the valence band through three primary radiative processes: absorption, spontaneous emission, and stimulated emission. [17].

2.7.1 Absorption

Absorption takes place when an electron in the valence band (VB) moves to the conduction band (CB) by absorbing a photon with energy equal to or greater than the optical band gap energy between the two bands. The rate of absorption is influenced by the photon density, the electron density in the valence band, and the number of available states in the conduction band.

2.7.2 Radiative Transitions

Radiative recombination is the process in which an electron from the conduction band recombines with a hole in the valence band, emitting a photon. The rate of radiative

recombination depends on the electron and hole densities. There are two main radiative recombination processes in semiconductor lasers: spontaneous emission and stimulated emission, as shown in Figure 2.5.a [18].

2.7.2.1 Spontaneous Emission

Spontaneous emission happens when an electron in the conduction band spontaneously recombines with a hole in the valence band, emitting a photon. This process/emission is random, resulting in a photon with a random phase and direction.

2.7.2.2 Stimulated Emission

Stimulated emission occurs when an incident photon interacts with an electron in the conduction band, prompting it to recombine with a hole in the valence band and emit an identical photon (same energy, phase, and direction). This process additionally depends on the photon density and leads to optical gain in semiconductor lasers.

2.8 Non-Radiative Recombination in Semiconductors

Non-radiative recombination occurs when an electron-hole pair recombines without photon emission. The energy released by the recombination process is typically converted to heat, impacting device efficiency and increasing threshold current. The major non-radiative recombination processes are Shockley-Read-Hall recombination and Auger recombination.

2.8.1 Defect-Related Recombination (Shockley-Read-Hall, SRH).

Also called trap-assisted recombination, this process happens when carriers recombine through defect states, or traps, within the band gap as in Figure 2.5.b. There are extra energy levels within the forbidden gap because of the existence of a foreign atom or a structural defect [17].

2.8.2 Auger Recombination

Auger recombination is a non-radiative, three-carrier process where the energy released by a recombining electron-hole pair is transferred to a third carrier, which is then excited to a higher energy state, as shown in Figure 2.5.c. The excited carrier eventually relaxes, with the energy converted to heat. The rate of Auger recombination depends on several factors, including temperature, bandgap, and carrier concentration.

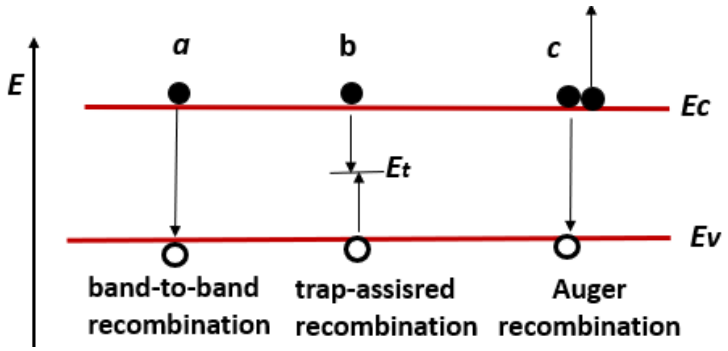

Figure 2.5. Carrier recombination processes in semiconductors.

2.8.3 Free Carrier Absorption

Free carrier absorption involves photons being absorbed by free carriers, causing them to transition to higher energy states. Free carrier absorption can occur with electrons in the conduction band and hole in the valence bands, and increases the internal optical loss, leading to higher threshold current density.

2.8.4 Carrier Leakage

Carrier leakage happens when electrons or holes, possessing sufficient thermal energy, escape from the active layer (such as a quantum well), and into surrounding barrier or cladding layers, where they may then recombine. Carrier leakage can lead to radiative or non-radiative recombination outside the active region, depending on the band offsets and thermal spread of carriers. Materials with larger conduction/valence band offsets provide better carrier confinement and reduced carrier leakage.

2.9 Fermi-Dirac distribution and Population Inversion

The conduction band of a semiconductor has many empty energy levels. In thermal equilibrium, the probability that an energy level is occupied by an electron is determined by the Fermi-Dirac distribution function. This function, which depends on energy, temperature, and the Fermi level (E_f) is shown in Equation (2.4).

$$f(E) = \frac{1}{1 + e^{\frac{E-E_f}{k_B T}}} \tag{2.4}$$

Where k_B is the Boltzmann constant, T is the temperature in Kelvin, $k_B T$ is the thermal energy (k_BT = 0.026 eV at T = 300° K), E is the energy of the carrier, and E_f is Fermi level. The Fermi level is a critical parameter that corresponds to the energy at which there is a 50% probability of a state being occupied by an electron. In intrinsic semiconductors, it is located at the middle of the band gap, while in doped semiconductors, it shifts towards the conduction band (n-type) or the valence band (p-type). In semiconductors, the bandgap energy (E_g) between the conduction and valence bands is usually larger than the thermal energy at room temperature ($E_g > K_B T$), meaning most electrons reside in the valence band under normal conditions. To achieve optical gain and laser action, a population inversion is required, which means more electrons must occupy the relevant states in the conduction band than the associated states in the valence band. This inversion can be achieved by injecting carriers, which creates a non-equilibrium state with quasi-Fermi levels, E_{fc} and E_{fv}, for the conduction and valence bands, respectively. Optical amplification requires a net emission of photons, meaning transitions from the conduction band to the valence band must be greater than the reverse. This condition is achieved by ensuring that the quasi-Fermi level separation is greater than the bandgap energy, $E_{fc} - E_{fv} > h\nu > E_g$. Injecting carriers increases the quasi-Fermi level separation until it exceeds the bandgap, allowing population inversion. When the gain matches the optical losses, laser action is initiated. Due to the high rate of stimulated emission, even though the injection of carriers increases with increasing current, Fermi-level pinning typically occurs, ensuring a stable carrier density above threshold [17]. In quantum well QW lasers, Fermi-level pinning happens above threshold because once lasing starts, most of the

injected carriers go into producing light through stimulated emission, so the carrier density stays almost constant this is called pinning. But in quantum dot (QD) lasers, this effect is not as strong. QDs have discrete energy levels like atoms, and because of things like inhomogeneous broadening (differences in dot sizes), and slow carrier capture and relaxation from higher states or the wetting layer, the carrier density doesn't stay perfectly constant above threshold. This means the Fermi levels can keep changing a bit even after the lasting start. So, while some level of Fermi-level pinning still happens in QD lasers, it's weaker and less sharp than in QW lasers. The discrete nature of the states also leads to the useful features like lower threshold currents, better performance at high temperatures, and smaller linewidth enhancement factors. Because of this, when studying or modeling QD lasers, we can't assume they behave exactly like QW lasers in terms of Fermi-level pinning.

2.10 Optical Feedback and Required Threshold Gain in Fabry-Perot Lasers

In a laser system, both stimulated emission and absorption are competing processes, as an incoming photon can either be absorbed or trigger the creation of a second photon. Since the electron population in the valence band typically far exceeds that in the conduction band, absorption prevails when the carrier injection level is low. At a certain external current, a sufficient number of electrons in the conduction band and holes in the valence band make the semiconductor optically transparent over a small range of wavelengths. As the current increases further, the active region of the semiconductor laser begins to show optical gain and can amplify the electromagnetic radiation passing through it. Spontaneously emitted photons serve as the noise input for the amplification process. Although stimulated emission can begin as soon as current is applied to the semiconductor laser, significant coherent laser light is not emitted until the current reaches the critical value, known as the threshold current (J_{th}). At the threshold current, the laser output becomes predominantly governed by stimulated emission rather than spontaneous emission [19, 20].

Optical gain by itself is insufficient for laser operation. The other component required for this is optical feedback, and this is typically achieved using a Fabry-Perot (FP) cavity. A Fabry-Perot cavity is made up of two parallel mirrors at each end, reflecting photons traveling along the cavity's length back and forth, as shown in Figure 2.6. In

semiconductor lasers, cleaved facets can form the mirrors of the FP cavity. The semiconductor-air boundary has a reflectivity of around 30%, due to the difference in refractive indices between these two media.

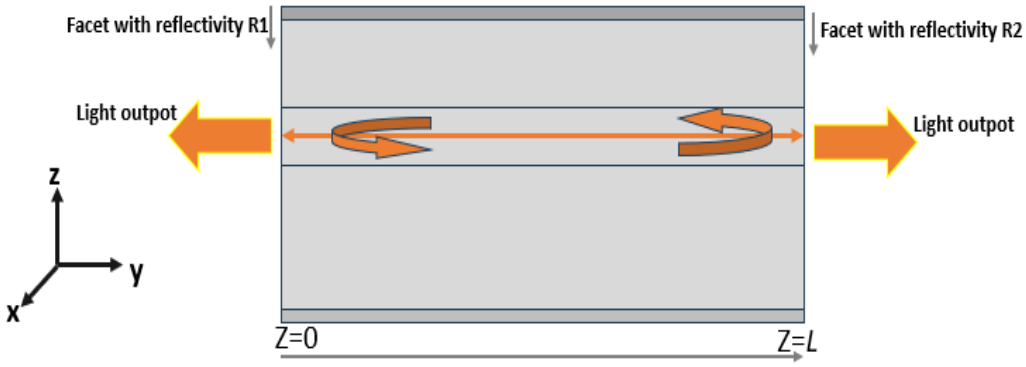

Figure 2.6. Schematic diagram showing the principle of a Fabry-Perot edge emitting laser.

Some photons passing through the cavity are lost due to absorption or scattering within the cavity. Below the threshold, optical loss exceeds optical gain, preventing stimulated emission from sustaining a continuous stream of coherent photons, resulting in an output that is mainly composed of spontaneously emitted photons [5]. At the threshold, optical gain matches optical loss, enabling stimulated emission to dominate. In the region above the threshold, the laser output increases almost linearly with the current. Almost all electrons and holes injected into the active region are now recombined via stimulated emission, creating a stable system that generates coherent laser light.

Since the light amplification or optical gain (g) competes against the internal optical losses (α_i) (e.g. free carrier absorption), and mirror losses (α_m), lasing can only occur if the system produces more light than it loses during one round trip [9].

$$R_1 R_2 \,.\, e(g_{th} - \alpha_i)2L = 1 \qquad (2.5)$$

Where R_1 and R_2 are the mirror reflectivities, L is the length of the gain medium, and g_{th} is the threshold gain. When photons pass through the length of the gain medium

L, the amount is increased by e^{gL}, but reduced by $e^{-\alpha_i L}$. The photons not reflected by the mirrors R_1 and R_2 are coupled out of the mirror. Thus, the lasing threshold is reached when the optical gain of the laser medium balances all the losses ($\alpha_i + \alpha_m$) that light encounters during a complete round trip of the optical cavity of the laser. This can be described as:

$$g_{th} = \alpha_i + \alpha_m \tag{2.6}$$

$$\alpha_m = \frac{1}{2L}\ln\left(\frac{1}{R_1 R_2}\right) \tag{2.7}$$

$$g_{th} = \alpha_i + \frac{1}{2L}\ln\left(\frac{1}{R_1 R_2}\right) \tag{2.8}$$

This means that minimising the threshold gain g_{th} requires low optical losses and high reflectivity mirrors. The presence of L in the denominator implies that by lengthening the gain medium, the necessary threshold gain (per unit length) will be reduced [9].

In addition to the gain elements, a laser diode has contacts and p- and n-doped cladding layers for electrons and holes injection, which will recombine inside the undoped active region. Therefore, when designing the entire structure, consideration must be given to the doping concentrations and thicknesses of these doped materials, not only to restrict the optical field but also to reduce the processes such as current diffusion and free carrier absorption caused by the dopants, that may reduce the efficiency.

2.11 Quantum confinement: Density of states

The electronic and optical characteristics of semiconductor lasers are influenced by the density of states (DOS). The density of states $\rho(E)$ is a function of energy E and is defined as the number of electronic states per unit volume per unit energy. It is used to calculate the energy distribution of electrons and holes in the conduction and valence bands by multiplying the density of states by the state's occupation probability. When a forward bias is applied, the electron and hole population in the conduction and valence bands, respectively, increase. The quasi-Fermi levels that describe the electron

and hole populations shift towards the conduction and valence bands, respectively, resulting in an energy separation between them that is related to the applied voltage. For a given quasi-Fermi level shift the carrier density is increased when the density of states is higher. When the separation between the quasi-Fermi level separation is equal to the bandgap energy, the material becomes transparent at the wavelength corresponding to the bandgap energy. Figure 2.7 shows the DOS function for 3D, 2D, 1D, and 0D systems.

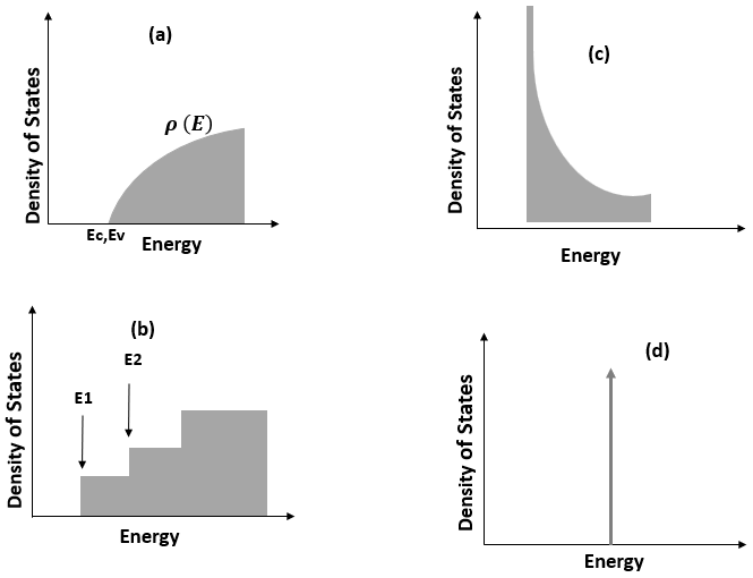

Figure 2.7. Density of states for: (a) bulk (3D), (b) quantum well (2D), (c) Quantum wire (1D), and (d) Quantum dot (0D) materials.

Density of States in Bulk Semiconductors (3-D)

In a bulk semiconductor, carriers can move freely in all three spatial dimensions. A material is considered to be 3D, when its dimensions are large (typically greater than 100 nm). The DOS in the conduction and valence bands can be expressed as:

- Conduction band:

$$\rho_c\,(E) = \frac{4\pi}{h^3}\,(\,2m_c^*)^{\frac{3}{2}}(E - E_C)^{\frac{1}{2}} \quad \text{, for} \quad \mathrm{E} \geq E_C \qquad (2.9)$$

- Valence band:

$$\rho_v(E) = \frac{4\pi}{h^3}(2m_v^*)^{\frac{3}{2}}(E - E_v)^{\frac{1}{2}} \quad \text{, for E} \geq E_v \qquad (2.10)$$

where E_C is the conduction band edge energy, and E_V is valence band edge energy. m* is the effective mass of the band.

In bulk materials, states near the band edges are mostly occupied, while higher energy states are mostly empty. Full occupancy near the band edges broadens the gain spectrum and increases the peak gain.

Density of States in Quantum Wells (2-D)

In quantum wells, carriers can move freely in two spatial dimensions (Lx, Ly), while they are confined in the third dimension (Lz). This confinement, achieved by placing a material with a smaller bandgap between two layers with larger bandgaps, leads to the formation of quantized energy levels. When the well width is on the order of the de Broglie wavelength, the carriers' energy levels become quantized into discrete values due to their confinement in one direction. The density of states (DOS) in a quantum well refers to the number of available states per unit energy per unit area. As a result, the DOS exhibits discrete steps at each quantized energy level. The DOS for both the conduction and valence bands can be described as follows:

- Conduction band:

$$\rho_c(E_n) = \frac{4\pi m_c^*}{h^2}\left(\frac{n}{L_Z}\right) \qquad (2.\ 11)$$

- Valence band:

$$\rho_v(E_n) = \frac{4\pi m_v^*}{h^2}\left(\frac{n}{L_Z}\right) \qquad (2.\ 12)$$

where n is the nth energy level, and m* is the effective mass for the nth energy level in the conduction band or valence band.

The confinement effect in quantum wells increases the DOS near the band edge. This, in turn, increases the peak gain achievable with lower injection levels (which also narrows the gain spectrum), resulting in more efficient devices.

Density of States in Quantum Wires (1-D)

In quantum wires, carriers are free to move only in one direction (Lx), while they are quantized in the other two dimensions (Ly, Lz). This effectively forms a one-dimensional (1-D) system, where the DOS has distinct peaks at each quantized energy level, often referred to as having a shark-fin form. The DOS in a quantum wire is given by:

$$\rho_{1D}(E) = \frac{1}{\pi h} \sqrt{\frac{m^*}{(E - E_{ny} - E_{nZ})}} \qquad , E \geq E_{ny} + E_{nZ} \quad (2.13)$$

The quantization in two dimensions leads to sharper peaks in the DOS compared to bulk and quantum well structures, potentially enhancing the efficiency of devices.

Density of States in Quantum Dots (0-D)

When carriers are confined in all three spatial dimensions (Lx, Ly, and Lz), as in quantum dots, a zero-dimensional (0-D) system is formed. The energy states become completely discrete, and the DOS is represented by a delta function:

$$\rho(E) = 2\delta(E - E_n) \qquad (2.14)$$

The DOS of quantum dots lead to a high peak gain and a narrower gain spectrum, which are desirable for efficient devices. However, due to the inherent asymmetry and inhomogeneous size distribution of quantum dots, a perfect 0D DOS distribution has

yet to be fully achieved in practice, often resulting in a broader gain peak than theoretically expected.

2.12 Confinement Structures in Semiconductor Lasers

Confinement structures are critical to the performance of semiconductor lasers. They maximize carrier recombination, improve optical efficiency, and control the light output to ensure effective laser operation. There are three primary types of confinement: optical, carrier, and current, each serving a specific role in enhancing the laser's performance.

2.12.1 Optical Confinement

In the laser cavity, the optical field extends along both the growth direction (z-axis) and the transverse direction (y-axis). To maximize the probability of stimulated emission, the laser structure is designed to ensure high photon density within the active region while still allowing sufficient light output.

Two methods are employed to guide the propagating optical wave within the laser cavity: gain-guiding and index-guiding.

Gain-guiding results from a spatially varying gain profile caused by a non-uniform carrier distribution. Greater optical amplification occurs in regions with higher optical gain, effectively guiding light along these areas. However, the gain-guiding approach provides relatively weak confinement of the optical field. This limitation arises from the small refractive index change induced in the electrically pumped region, through the Kramers-Kronig relation [5]. Despite these shortcomings, early semiconductor lasers predominantly used gain-guiding due to their simpler fabrication process.

Index-Guiding confines most of the optical field within the active region by utilizing total internal reflection. Index-guiding along the growth direction is achieved by surrounding the active region with cladding material that has a lower refractive index, so that only a minimal portion of the optical field extends into the cladding layers. The extent of the optical confinement is determined by the refractive index difference between the active region and the surrounding cladding layers.

2.12.2 Carrier Confinement

To improve laser device performance, it is essential to effectively confine electrons and holes, which increases the likelihood of radiative recombination. Here is an outline of the evolution in carrier confinement within semiconductor laser structures. For more details, see chapter 1 (1-1).

Semiconductor lasers have evolved significantly through various structural improvements, beginning with high-threshold, low-efficiency, p-n junction lasers, followed by p-i-n structures that improved carrier confinement and the recombination. The introduction of double heterostructure (DH) lasers provided both optical and carrier confinement. Then, Separate Confinement Heterostructure (SCH) lasers allowed the design of confinement layers for the carriers and the optical field to become decoupled, becoming the commercial standard due to improved efficiency.

Quantum well (QW) lasers made use of QWs which provided quantum confinement along one dimension. Improved efficiency was achieved due to the more favorable DOS. Quantum dot (QD) lasers introduced three-dimensional quantum confinement, which promised even lower threshold currents. However, this is still challenging due to limitations in the growth method, which results in shape and size variations of the quantum dots. Finally, Dot-in-Quantum Well (DWELL) lasers, which combined QWs and QDs to further improve efficiency, where QWs help with the capture of carriers, as the carriers can otherwise move between the QDs and away before being captured. The QWs keep the carriers close to the QDs, increasing the likelihood of capture into the dots. They are also used to extend emission wavelength, which is probably the main motivation for using them in GaAs-based 1300nm QD lasers. The DWELL structure is used in the structures of this study.

2.12.3 Current Confinement

To enhance semiconductor laser performance, various current confinement techniques have been developed to minimize the electrically pumped area of the active region, thereby reducing the threshold current and improving device efficiency. The main methods include:

1. Oxide Stripe: This is the simplest method, where the p-side contact is deposited onto dielectric material with a stripe window, as illustrated in Figure 2.8. The oxide stripe limits the region where current is injected from the p-side. However, the stripe doesn't prevent current spreading in the cladding layer. It is used in gain-guided designs and was employed in the 1.55 μm InAs/InP quantum dot lasers studied in this thesis.

2. Ridge Waveguide: Ridge structures provide weak index-guiding. The current is injected into the ridge as shown in Figure 2.9, traveling through a narrow path directly into the active region. The optical field is confined by the interface between the semiconductor and air.

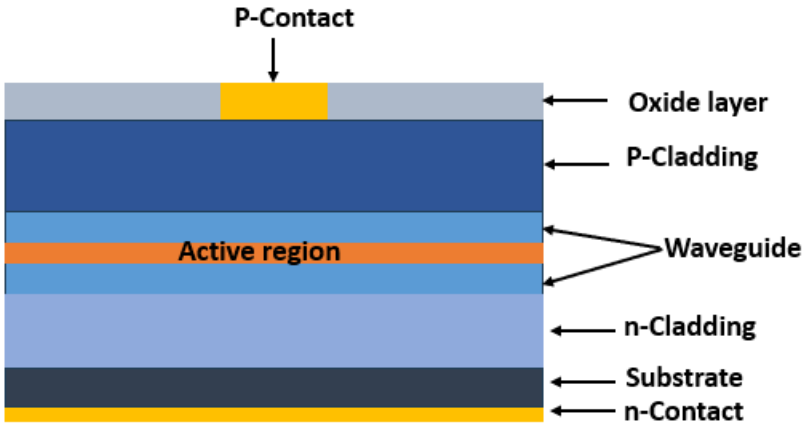

Figure 2.8. Schematic of oxide stripe laser.

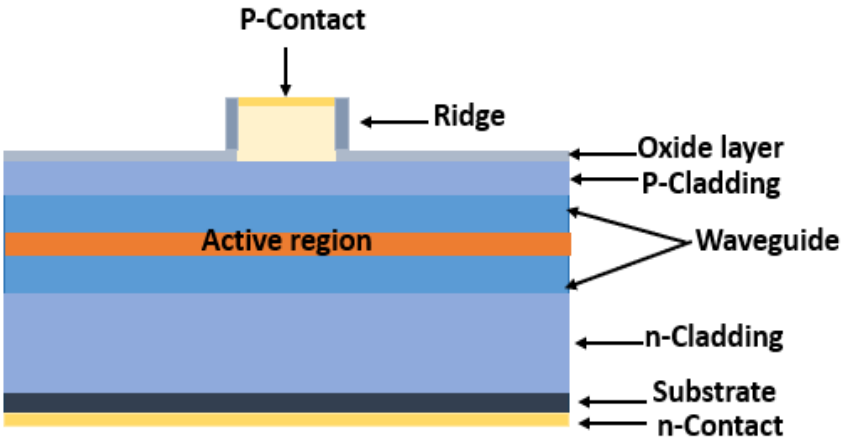

Figure 2.9 Schematic of ridge structure laser.

2.12.4 Optical Confinement Factor

The optical confinement factor is the ratio of the square of the electric field confined within the active region to the total optical field power. It reflects the reduction in optical gain caused by the spreading of optical modes outside the active region. This factor indicates the portion of photons in the guided wave that interact with the active layer. The overall amplification of the optical field per unit length is given by the product of the confinement factor and the material gain per unit length.[9].

2.13 Semiconductor laser threshold current and threshold current density

The threshold current in a semiconductor laser is the current, I_{th}, necessary to provide sufficient gain to overcome losses and achieve lasing. As shown in Figure 2.10, the threshold current can be found from the light output power versus current characteristics (P-I), where the light output starts to dramatically increase with current. The threshold current is an important device parameter where a low value is desired. When $I < I_{th}$, the optical output is mainly from spontaneous emission. When $I > I_{th}$, stimulated emission starts to dominate, a rapid increase in output power is also typically observed.

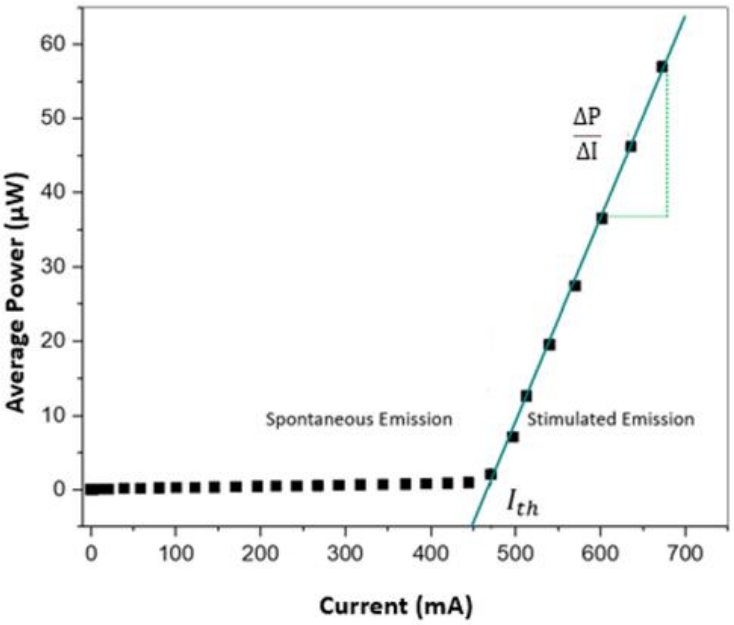

Figure 2.10. Optical Power vs. Current characteristic.

The threshold current is influenced by the quality of the semiconductor material used to fabricate the device and the overall design of the waveguide structure. However, it also depends on the size and area of the laser device. Therefore, a longer laser typically requires more current to initiate laser action compared to a shorter one. When comparing threshold currents of devices with different lengths, it is more meaningful to refer to the threshold current density rather than the threshold current itself. The threshold current density (J_{th}) is calculated by dividing the experimentally determined threshold current I_{th} by the effective area of the pumped region, which is usually measured through near-field techniques and the device's length, as detailed in Chapter 3. A lower threshold current density is always preferable for a laser. This value is also a key parameter that directly reflects the quality of the semiconductor material used in the device.

2.14 External Differential Quantum (Slope) Efficiency

Another important parameter of the laser diode is the external differential quantum efficiency (η_{ext}), and it is defined as the number of photons generated and coupled out of the laser cavity per electrons injected into the device. It can be expressed as,

$$\eta_{ext} = \eta_i \frac{\alpha_m}{\alpha_m + \alpha_i} \qquad (2.15)$$

Where, η_i is internal quantum efficiency, which accounts for injected carrier to photon conversion efficiency, α_m is the mirror loss, and α_i is the internal optical loss.

It can be experimentally determined from the slope of the optical power versus current (P–I) curve above the threshold current. We have recorded the P-I curves for laser diodes with different cavity lengths under pulsed operation. The ΔP/ΔI slope was multiplied by 2 because the laser diode with cleaved mirror facets emits equal amounts of light from both the front and back mirror facets and then multiplied by $[\frac{q\lambda}{hc}]$ to convert the optical power into photons per electron, as demonstrated in Equation (2.16) [9].

$$\eta_{ext} = 2 \frac{\Delta P}{\Delta I} \frac{q\lambda}{hc} \qquad (I > I_{th}) \qquad (2.16)$$

where h represents Planck's constant, λ is the wavelength of the emitted light, q is the electric charge of a single electron, and c is the speed of light [1].

Ideally, the slope efficiency remains constant with current; however, in practical devices, the slope efficiency changes, and the output power tends to saturate at higher current injections [1]. Power saturation is primarily caused by leakage current at higher injection levels, internal optical losses, and junction heating, all of which can increase as the laser power rises.

Using Equation (2.15) the external differential efficiency η_{ext} can be related to the laser cavity length L_C, and internal differential quantum efficiency η_i by,

$$\frac{1}{\eta_{ext}} = \frac{1}{\eta_i}\left[\frac{\alpha_i}{\ln(R^{-1})}L_c + 1\right] \qquad (2.17)$$

where α_i refer to internal optical loss, and R is the reflectivity of the facets, assumed to be the same. For the semiconductor materials used in the laser devices in this study, R is 0.28. The external differential efficiency, η_{ext}, will be lower than the internal differential quantum efficiency, η_i.because some of the light is lost due to internal optical loss, rather than being coupled out through the mirrors [5].

2.15 Internal Differential Efficiency and Internal Optical Loss

The internal differential efficiency reflects how effectively injected electrical current is converted into photons within the laser diode's active region. This efficiency is influenced by carrier processes such as current spreading, carrier injection, and non-radiative processes. To determine the internal differential efficiency (η_i) and internal optical loss (α_i) for various structures, we will apply Equation (2.17). By plotting $\frac{1}{\eta_{ext}}$ against cavity length L_c, we can extract values for the internal differential quantum efficiency η_i and the internal optical loss α_i. The y-intercept provides internal quantum efficiency, while the slope allows us to calculate the internal optical loss. The mirror loss (α_m) can be determined using equation (2.7). This approach assumes that the internal quantum efficiency η_i and internal optical loss α_i are independent of the laser cavity length.

2.16 Gain-Current density relation

In laser materials, the relationship between the peak gain and current density is commonly represented by Equation (2.18). The curve in Figure 2.11 represents this Equation [9],

$$G_{pk} = G_0 \ \ ln\left(\frac{J_1}{J_{trans}}\right) \qquad (2.18)$$

Where G_{pk} is peak gain, G_0 and J_{trans} are fitting parameters. The equation as shown gives the current for one layer J_1. For N identical layers, the total gain parameter is $G_{No} = NG_0$ and the total current density is $J_N = NJ_1$.

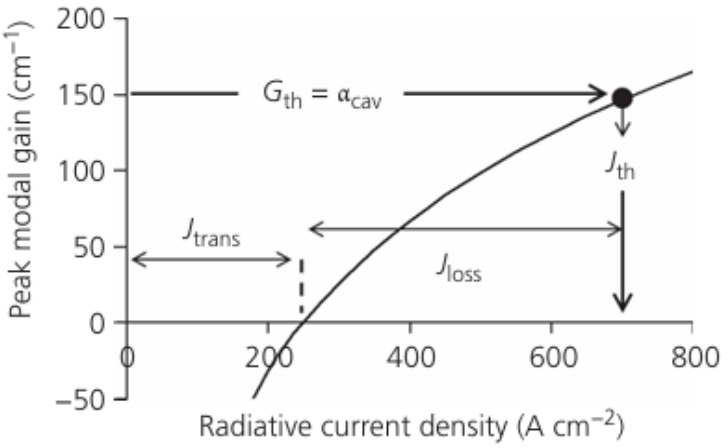

Figure 2.11 Gain-Current curve [9].

Lasing takes place when the optical gain is sufficient to surpass the optical losses. Thus, at the threshold, the optical gain will match the total optical loss, which can be divided into internal optical loss and mirror loss. Furthermore, for a basic Fabry-Perot laser, this typically happens at the peak of the gain. By substituting in the total optical losses at threshold for G_{th} we can derive an equation for ln (J_{th}) from Equation (2.8).

$$ln\ J_{th} = \frac{1}{L}\left[\frac{ln\ (R^{-1})}{NG_0}\right] + \frac{\alpha_i}{NG_0} + ln(NJ_{trans}) \qquad (2.19)$$

Where J_{th} is the threshold current density, R is the mirror reflectivity, N is the number of QW/QD layers, α_i is the internal optical loss, and the transparency current density is J_{trans}.

From this equation, we can plot the experimentally determined threshold current density against the inverse cavity length to obtain the gain coefficient parameter G_0. This is used in Chapters 4, 6 and 7.

2.17 Temperature Dependence of Threshold Current Density

The variation in threshold current density with temperature is an important characteristic of diode lasers, which is why considerable effort is devoted to designing devices with a threshold current that is less affected by temperature changes. This helps reduce the costs and power consumption associated with cooling the device. Key processes involved include Auger recombination, carrier leakage from the confined region, barrier recombination, and current spreading through the cladding layers due to drift and diffusion [21,22].

Various factors can contribute to the temperature sensitivity of the threshold current and the high threshold current density in 1.55 μm InAs/InP quantum dot laser devices. These factors include thermal escape of carriers into the wetting layer [23–25], gain saturation, defect-related non-radiative recombination, and non-radiative Auger recombination [26,27]. The relative significance of these physical factors in influencing the temperature dependence of the threshold current is still under investigation.

2.18 Quantum Dots Applied as Optical Gain Medium

A quantum dot is a nanoscale semiconductor structure where charge carriers (electrons and holes) are confined in all three spatial dimensions, resulting in discrete, atom-like energy levels. This quantum confinement produces unique optical and electronic properties that are size-tunable and different from those of bulk materials. Because carriers are confined in all three dimensions, the quantum effects become prominent. As a result, the electron energy levels can no longer be considered continuous and must

be treated as discrete [1]. This characteristic has led to theoretical predictions that quantum dots are an ideal active medium for optoelectronic devices.

QD lasers have achieved increased importance after significant progress in nanostructure growth, especially the self-assembled growth techniques for QDs. Self-assembled quantum dots (QDs) are commonly produced using the Stranski-Krastanow (SK) growth method, which is based on heteroepitaxy involving a lattice mismatch. This approach enables the formation of self-organized QDs [28,29]. During the epitaxial deposition of layers onto a substrate, three-dimensional islands begin to develop once a critical layer thickness is surpassed. These islands form spontaneously as a result of the lattice mismatch between the deposited material and the substrate. When the deposited material has a larger lattice constant, strain accumulates as it attempts to match the substrate's lattice structure. Rather than relaxing this strain through the formation of dislocations, which would introduce defects, the system minimizes its total energy by forming three-dimensional islands, as mentioned in Section 1.3. This transition reflects a competition between the strain energy (which favours island formation to allow partial relaxation) and surface energy (which favours flat, layer-by-layer growth). At the island base, the material remains strained to match the substrate, but the upper regions can elastically relax toward the bulk lattice constant. Over time, these strain-driven 3D islands evolve into quantum dots QDs.

Three-dimensional quantum confinement would give quantum dots QDs a nearly delta-function-like density of states DOS, making them an ideal gain medium, as population inversion can be achieved with a reduced carrier density. Therefore, quantum dot lasers can theoretically achieve lasing with a low threshold current. Additionally, QD lasers are predicted to be less sensitive to temperature variations compared to quantum well lasers. This reduced sensitivity is due to the large energy state separation which would limit the ability of carriers to transition to higher energy states. As a result, the threshold current is expected to be temperature insensitive. Moreover, because of their quantum confinement effects, QDs are often referred to as artificial atoms, which allow their properties, such as emission wavelength, to be tuned by controlling the size, shape and composition of the dots. This feature gives QDs exceptional versatility and allows them to produce highly monochromatic light.

However, the problem is that the QDs are not identical due to the statistical distribution of island sizes, i.e., the formation of quantum dots is influenced by statistical variations in dot size, which results in inhomogeneous broadening of the energy levels. As a result, the emitted spectra tend to be broader than those produced by the best QW active regions. Lasers can then have high threshold current densities and a temperature-sensitive current threshold. Inhomogeneous broadening in QD lasers, caused by size variations among quantum dots, reduces peak gain by spreading the optical gain over a wider energy range. This leads to higher threshold current densities, as more carriers are required to achieve sufficient gain. Additionally, carriers may populate non-lasing QDs, further reducing efficiency. While QD lasers can exhibit high T_0 if lasing remains in the ground state, inhomogeneous broadening can degrade temperature stability by promoting carrier redistribution, escape, or excitation to higher energy states, thereby increasing the temperature dependence of the threshold current. Nevertheless, some performance improvements can still be observed compared to quantum well lasers, particularly with regard to carrier localization and insensitivity to defects. Current performance was mentioned in Chapter 1 and further research is required to make further progress.

2.19 Quantum dash system

Quantum Dashes (QDHs) are elongated nanostructures, giving them a wire-like appearance. They have confinement in two dimensions and extended length in the third dimension. They are often compared to stretched quantum dots. Quantum dashes are grown using a self-assembled Stranski-Krastanow epitaxial growth mode, a process where the quantum dash structures form spontaneously on the the wetting layer substrate during deposition [30].

Due to the elongated, wire-like structure of QDHs, the electronic and optical properties differ along the length of the dash compared to the directions perpendicular to it.

To better illustrate this concept, we refer to Figure 2.12, which is taken from a study on a quantum dash quantum cascade photodetector (QDash -QCD). In this work, self-assembled InAs quantum dashes were incorporated into the active region of a long-wavelength infrared QCD. The quantum dashes exhibit dimensions of approximately 17 nm along the [110] axis and around 2.3 nm along the [001] axis. On average, the length along the $[1\bar{1}0]$ direction extends to about a hundred nanometers [31].

Figure 2.12 shows QDHs elongated in the [1$\bar{1}$0] direction, which means the quantum confinement is reduced along that direction [31]. This anisotropy leads to different emission characteristics depending on whether the electric field of the light is polarized parallel or perpendicular to the length of the dash.

The ability to control and select these modes makes QDHs especially useful in applications where polarization control is critical, such as telecommunications, optical sensors, and other advanced photonic applications to enhance performance [32,33].

The quantum dot and/or dash used in this study is composed of InAs, and we will discuss this in detail in Chapter 7.

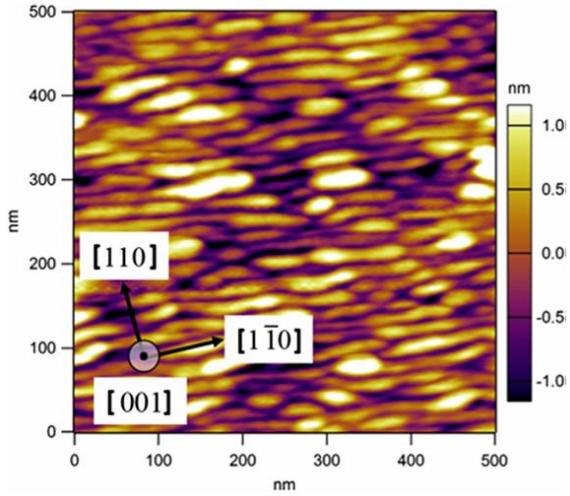

Figure 2.12. AFM image of uncapped InAs self-assembled Dashes, adapted from 31 . Note: This figure is provided solely to illustrate the concept that the quantum dash extension is longer along the [1$\bar{1}$0] direction.

2.20 Summary

This chapter provided an overview of basic semiconductor theory, starting with the semiconductor band structure. It then examined the impact of strain on semiconductor lasers. The chapter continued by discussing the density of states for both bulk and quantum structures. It also explained the electronic transitions in semiconductor lasers, beginning with photon absorption, followed by spontaneous emission, stimulated emission, and non-radiative recombination processes, such as SRH and Auger recombination. The concept of population inversion was also covered. The chapter then explored the mechanisms of optical feedback and threshold gain in Fabry-Perot lasers. Lastly, it defined the concept of threshold current in semiconductor lasers and discussed external and internal quantum efficiency, along with how these can be derived from experimental measurements.

References

1. Coldren, L. A., Corzine, S. W., & Mashanovitch, M. L. *Diode lasers and photonic integrated circuits*. Vol. 218. John Wiley & Sons. (2012).

2. Sibilia, C., Marciniak, M., Benson, T. M. & Szoplik, T. *Introduction. Photonic Crystals: Physics and Technology* Springer Milan.,1-4 (2008) doi:10.1007/978-88-470-0844-1_1.

3. Elkaramany, E. M. A., Hameed, M. F. O. & Obayya, S. S. A. *Fundamentals of photonic crystals*. Computational Photonic Sensors, Springer 29-52 (2019) doi:10.1007/978-3-319-76556-3_2.

4. Hamaguchi, C. and Hamaguchi, C., *Basic semiconductor physics.* (Vol. 9. 443-510). Berlin: springer. (2010).

5. Agrawal, G.P. and Dutta, N.K., *Semiconductor lasers*. Springer Science & Business Media. (2013).

6. Varshni, Y.P., Temperature dependence of the energy gap in semiconductors. *physica*, *Elsevier*, 34(1),.149-154. (1967).

7. Brennan, K. F.The physics of semiconductors: with applications to optoelectronic devices. *Cambridge university press*. (1999).

8. Misra, P. *Physics of condensed matter*. Academic Press. 37. (2011)

9. Blood, P. Quantum Confined Laser Devices: Optical gain and recombination in semiconductors (Vol. 23). *OUP Oxford*. (2015).

10. Adachi, S. *GaAs and related materials: bulk semiconducting and superlattice properties.*1-6. WorldScientific.(1994).doi.org/10.1142/9789812705709_0001

11. Hamaguchi, C., & Hamaguchi, C. *Basic semiconductor physics* (Vol. 9, pp. 443-510). Berlin: springer. (2010).

12. Tamargo, MariaC. II-VI Semiconductor Materials and Their Applications. II-Materials and Their Applications. *Taylor and Francis, New York*. (Vol. 12)., (113-170). (2002) doi:10.1201/9780203751305.

13. Wada, O. Optoelectronic Integration - Overview. *Optoelectronic Integration: Physics, Technology and Applications* 1-16 (1994) doi:10.1007/978-1-4615-2686-5_1.

14. Adams, A. R. Strained-layer quantum-well lasers. *IEEE Journal of Selected Topics in Quantum Electronics*, 17(5), 1364-1373. (2011).

15. Ghiti, A., Silver, M., & O'Reilly, E. P. Low threshold current and high differential gain in ideal tensile-and compressive-strained quantum-well lasers. *Journal of applied physics*, 71(9), 4626-4628. (1992).

16. Hussin, R. J. & Karomi, I. B. Progressing in III-V Semiconductor Quantum Dot Lasers Grown Directly on Silicon: A Review. *Springer*. *Silicon* (2024) doi:10.1007/S12633-024-03098-2.

17. Bernard, M. The history of laser conditions in semiconductors. *Semiconductor Science and Technology*, 27(9), 090201 (2012).

18. Brennan, K. The Physics of Semiconductors: With Applications to Optoelectronic Devices. *Cambridge university press*. (1999).

19. Fukuda, M. *Optical Semiconductor Devices*. Vol. 46. John Wiley & Sons. (1998).

20. Morgan, D. V., & Williams, R. H. *Physics and Technology of Heterojunction Devices*. Physics and technology of heterojunction devices (No. 8). IET. (1991).

21. Blood, P. Temperature dependence of threshold current. *Quantum Confined Laser Devices* 284–306, OUP Oxford (2015) doi:10.1093/ACPROF: OSO/9780199644513.003.0016.

22. Jarvis, L. Active Region Doping Strategies in O-Band InAs/GaAs Quantum-Dot Lasers. (Doctoral dissertation, Cardiff University). (2022).

23. Blood, P., Pask, H., Summers, H. D., & Sandall, I. Localized Auger recombination in quantum-dot lasers. *IEEE journal of quantum electronics*, 43(12), 1140-1146. (2007).

24. Matthews, D. R., Summers, H. D., Smowton, P. M., & Hopkinson, M. Experimental investigation of the effect of wetting-layer states on the gain–current characteristic of quantum-dot lasers. *Applied Physics Letters*, 81(26), 4904-4906. (2002).

25. Rossetti, M., Fiore, A., Sęk, G., Zinoni, C., & Li, L. Modeling the temperature characteristics of InAs/GaAs quantum dot lasers. *Journal of Applied Physics*, 106(2). (2009).

26. Pask, H. J., Summers, H. D., & Blood, P. Light-current characteristics of quantum dots with localized recombination. *Applied Physics Letters*, 87(8). (2005)

27. Marko, I.P., Masse, N., Sweeney, S.J., Adams, A.R., Sellers, I.R., Mowbray, D.J., Skolnick, M.S., Liu, H.Y. & Groom, K.M. Effect of gain saturation and nonradiative recombination on the thermal characteristics of InAs/GaAs 1.3/spl mu/m quantum dot lasers. In 2005 *IEEE* LEOS Annual Meeting Conference Proceedings (pp. 402-403). (2005).

28. Henini, M., & Bugajski, M. Advances in self-assembled semiconductor quantum dot lasers. *Microelectronics Journal,* 36(11), 950-956. (2005).

29. Baskaran, A., & Smereka, P. Mechanisms of stranski-krastanov growth. *Journal of Applied Physics*, 111(4). (2012).

30. Chu, R. J., Kim, Y., Woo, S. W., Choi, W. J. & Jung, D. Punctuated growth of InAs quantum dashes-in-a-well for enhanced 2-μm emission. *Discover Nano* 18(1), 31, (2023).

31. Wang, F.J., Ren, F., Liu, S.M., Zhuo, N., Zhai, S.Q., Liu, J.Q., Liu, F.Q. & Wang, Z.G., Normal incident long wave infrared quantum dash quantum cascade photodetector. *Nanoscale research letters,* 11, 1-6. (2016).

32. Grillot, F., Duan, J., Dong, B. & Huang, H. Semiconductor quantum dot lasers: Genesis, prospects, and challenges. in Quantum Photonics 191–266 *Elsevier*. (2024). doi:10.1016/B978-0-323-98378-5.00008-8.

33. Lelarge, F., Dagens, B., Renaudier, J., Brenot, R., Accard, A., Van Dijk, F., Make, D., Le Gouezigou, O., Provost, J.G., Poingt, F. and Landreau, J. Recent Advances on InAs/InP Quantum Dash Based Semiconductor Lasers and Optical Amplifiers Operating at 1.55 μm. *IEEE Journal of Selected Topics in Quantum Electronics* 13, 111–124 (2007).

Chapter 3: Experimental methodology

3.1 Introduction

The first part of the Chapter introduces the epitaxial structures used in this study and also the processes involved in fabricating the broad-area laser devices. The second part describes the experimental setups used to measure the device characteristics presented in this thesis. This includes fundamental information on device characterization, with detailed descriptions of the setups used to measure current-voltage-optical power characteristics, near-field measurements, and spectral characteristics. Finally, it covers the segmented contact method used to measure the gain and absorption of the active material.

3.2 Epitaxial structures

This work presents a study of different InAs quantum dot / dash (QD) laser structures that were grown on an InP substrate, for 1.55 μm emission in the C-band. These structures are nominally identical, except for the active region, as shown in Figure 3.1. In general, the active region for these structures consisted of dot or dash-in-well (DWELL) layers, where self-assembled InAs QDs are contained within an $In_xGa_{1-x}As$ quantum well. An $In_{0.52}Al_{0.26}Ga_{0.22}As$ barrier separated each DWELL layer. The waveguide core was formed by un-doped $In_{0.52}Al_{0.26}Ga_{0.22}As$ separate confinement heterostructure (SCH) layers and sandwiched by the InP cladding layers. The structure was capped with p-type $In_{0.53}Ga_{0.47}As$. Further details of the epi-structure can be found in chapters 6 and 7, where for example the x composition of the DWELL is specified. These structures were grown by Dr. Qiang Li of Cardiff University, using an epitaxial growth technique known as metal organic chemical vapor deposition (MOCVD). The self-assembled dots were grown using the Stranski-Krastanov process.

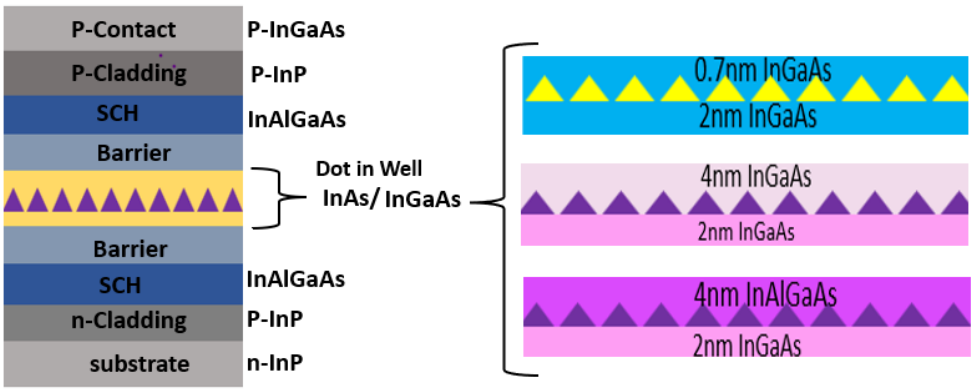

Figure 3.1: Schematic diagram of the epitaxial structures containing InAs QDs. Schematic diagram of the epitaxial structure (not to scale)

3.3 Laser Devices

The laser devices discussed in this thesis are broad-area laser devices. Specifically, these devices are described as edge-emitting or in-plane devices because the light is emitted along the plane of the gain medium.

The structure depicted in Figure 3.2 is an example of an oxide-isolated stripe laser, as described in Chapter 2. In this structure, the current is confined to flow only through the central stripe, where no oxide layer separates the metal contact from the epitaxial structure. The top layer of the device is heavily p-doped to ensure the formation of low resistance ohmic contacts. Consequently, the current spreads laterally as it flows through the device. This type of broad area laser device is often chosen over narrow ridge laser devices for wafer characterization because it does not suffer from issues such as leakage currents and recombination at the ridge sidewalls. Additionally, these devices are relatively easy and quick to fabricate.

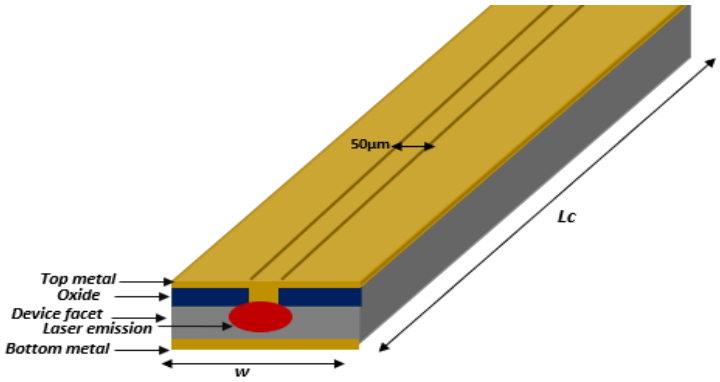

Figure 3.2: Diagram of an oxide-isolated stripe or broad area, edge emitting laser.

3.4 Device Fabrication

This section provides a brief overview of the key steps in the fabrication process used for this study. The laser devices studied were fabricated in Cardiff by Dr. Zhongming Cao. The broad area laser device is used to determine the basic electrical and optical properties of the grown material. The threshold current, internal quantum efficiency, internal optical loss, and optical emission spectrum can be obtained from the broad-area laser. The fabrication process for broad-area lasers is more straightforward than other types of devices and could thus provide relatively fast analysis for optimising growth. In this work, QD material was grown on an n-type InP substrate via MOCVD. The grown wafers were then fabricated into broad-area lasers with an oxide-isolated stripe width of 50 µm using a standard lithography process. The wafers were cleaved and then cleaned with acetone, methanol, and isopropanol for 5 minutes each. Electron beam evaporation was performed to deposit a 120 nm thick SiO_2 layer. A 50-um oxide isolation stripe was then defined by photolithography and reactive ion etching (RIE). Ti/Pt/Au p-electrodes were deposited by evaporation and annealed at 380 ^{o}C. The samples were then lapped down to a 150 µm thickness before AuGe/Ni/Au n-contacts were deposited by evaporation, as shown in Figure 3.3. The fabricated devices were cleaved into a range of cavity lengths, typically varying between 2000 µm and 300 µm in this study. The devices had uncoated and parallel facets, which reflected approximately 28% of the light at the lasing wavelength. The cleaved chips were

mounted on copper heat sinks, that were placed on TO-8 headers, using silver-loaded epoxy and were then gold-wire-bonded as shown in Figure 3.4.

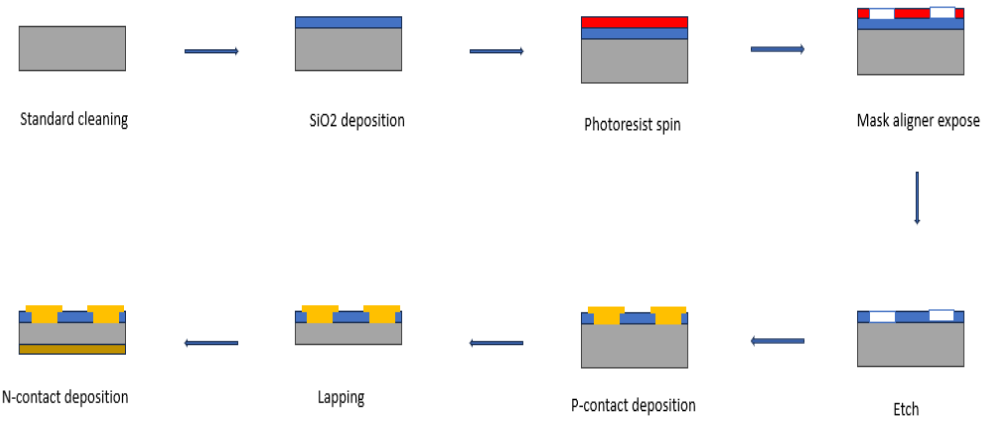

Figure 3. 3: A flow chart to illustrate the fabrication process for oxide-isolated broad area lasers.

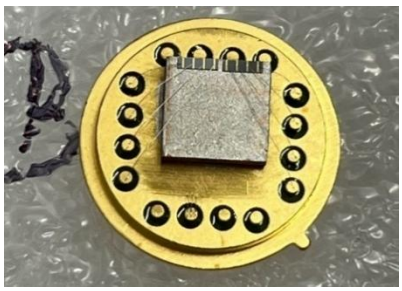

Figure 3. 4: A TO-8 header with lasers mounted onto a copper block to facilitate testing. Each header typically has twelve lasers mounted n-side down with silver epoxy, and wire-bonded with a 50 µm diameter wire connecting the upper p-contact to a pin.

3.5 Experimental Setup

This section provides a description of the experimental apparatus used to conduct measurements of power-current-voltage (PIV), lasing wavelengths, current-voltage-light-temperature (I-V-L-T) characteristics and near-field, as well as the gain and

absorption spectra using the multi-section technique. Note: L is used to indicate that the power is collected by an uncalibrated detector.

3.5.1 Near-Field measurements of laser diode devices

The nearfield (NF) measurement is used to image the optical beam emitted from the facet of a laser. The near-field of a device is a useful tool for testing laser diodes as it can identify imperfections in the facet quality, waveguide or contacts. In addition to quality analysis, the lateral spreading of current, as it flows from the top contact between the oxide stripe to the active area, can be determined by measuring the full-width half maximum (FWHM) of the spontaneous emission profile at the facet [1].

To measure the near-field, the device is placed in a holder that supplies electrical current via a pulse generator. The light from the facet is focused onto a camera using a microscope lens to image the laser's front facet directly on the sensor array of an infrared (IR) camera; this alignment is an important step to ensure the image is in focus. The infrared camera used in this experiment is controlled by the 'X-Vision' camera software. The next step involves using the pulse generator to inject current into the devices, so that they begin to lase. An infra-red viewing card is used to ensure that the emitted light is aligned to the centre of the lens and guided to the centre of the camera aperture. At this stage, one should start to see a white patch appear on the camera video output and alignment is continued until the near-field is in focus and positioned at the centre of the image.

To get an accurate representation of the beam profile, the use of neutral-density (ND) filters are sometimes necessary. ND filters are used before the light is collected by the camera to reduce its intensity, preventing saturation of the camera. When the optimum line profile has been achieved, the data can be saved. An image is shown in Figure 3.5(a). Measurements are conducted at a current 10% below the laser threshold to minimize the effect of stimulated emission, which could lead to an underestimation of the device width. The line profile along the x-axis, at the y-position where the intensity is maximum, gives the near-field image, and the resulting intensity profile is expressed in pixels. The full-width half maximum FWHM is then measured and converted from pixels to real units through calibration. This calibration is performed by pumping two lasers simultaneously and using the known distance between them to determine the

calibration factor, as shown in Figure 3.5(b). The FWHM of the near-field intensity profile represents the width of the pumped stripe, indicating the degree of current spreading.

Because the length of the devices is known, and the width is determined by near-field measurements, the threshold current can be converted into a threshold current density (J_{th}). The current density can be calculated by dividing the threshold current by the near-field width and stripe length. Equation (3.1b) is used to calculate the current density [2].

$$I_{th} = L_c w J_{th} \qquad (3.1a)$$

$$J_{th} = \frac{I}{A} \qquad (3.1b)$$

Where I is the threshold current, L_c is the cavity length of the laser diode, w is the effective width of the electrically pumped region, and A is the active area.

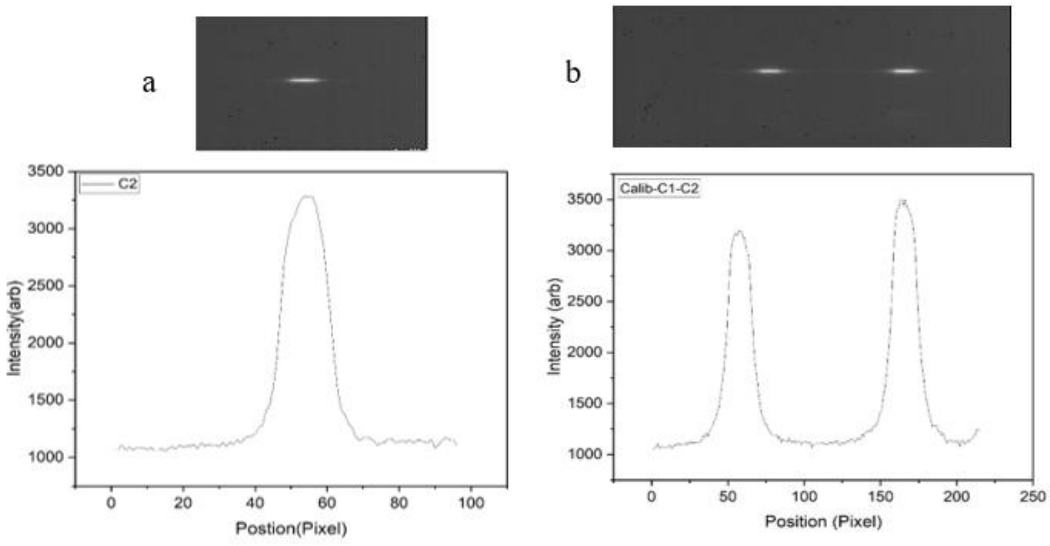

Figure 3.5: The optical near-field image (top) and the intensity profile along a line (bottom) for (a) a device measurement and (b) a calibration measurement.

3.5.2 The Current, Voltage, and Light characteristics (I-V-L).

The voltage, and optical power characteristics are measured as a function of current, and the resulting curves provide several key parameters for the diode characteristics, including the threshold current and the slope efficiency. To record these characteristics, laser devices are loaded on the holder and placed directly in front of the integrating sphere to capture as much light as possible. This integrating sphere allows for the calibrated measurement of the optical output power from a device. The integrating sphere was set to use a calibration factor for a wavelength of 1550 nm. A laser mounted on a temperature-controlled holder is pumped using a pulse generator. The current is incrementally increased, and the resulting voltage and optical power output are recorded. When making this measurement, the I-V-P characteristics of the laser device can be set up simultaneously to assess the characteristics of the device. This setup is shown in Figure 2.10.

These curves provide the threshold current; it is the point at which the device starts to predominantly emit stimulated photons [3]. It corresponds to the turning point where the light output begins to increase sharply, this concept is explained in detail in Chapter 2.

The threshold current is marked by the dashed green line, and the solid green line is a linear fit to the curve above threshold, as shown in Figure. 2.10.

The slope efficiency ($\Delta P/\Delta I$) is determined by taking the gradient of the above-threshold P-I curve [4,5]. This can then be converted to external differential efficiency (η_{ext}) using Equation (2.15). Additionally, Equation (2.17) can be used to calculate the internal optical loss (α_i) and the internal quantum efficiency (η_i), as explained in Chapter 2.

During the measurement, the devices were driven by a pulsed current source, with a pulse duration of 1 μs and a repetition frequency of 5 kHz, to avoid self-heating effects.

3.5.3 Lasing wavelength measurement (Optical emission spectra)

The lasing wavelength is measured using an optical spectrum analyser with a resolution of 0.2 nm as shown in Figure 3.7. The device being measured is mounted on a temperature-controlled stage. A lens is used to focus the laser beam directly onto a multi-mode optical fibre, which is connected to the spectrum analyser. To achieve the maximum power coupled into the fibre, for alignment a detector card is used to locate the laser beam and optimise the laser beam position and focus and then a fine alignment is completed by maximising the spectrum analyser signal while on a low-resolution setting. A pulse generator is used to inject the necessary current into the device. The spectrum is then measured at the threshold current and at 10% above the threshold current ($1.1 \times I_{th}$).

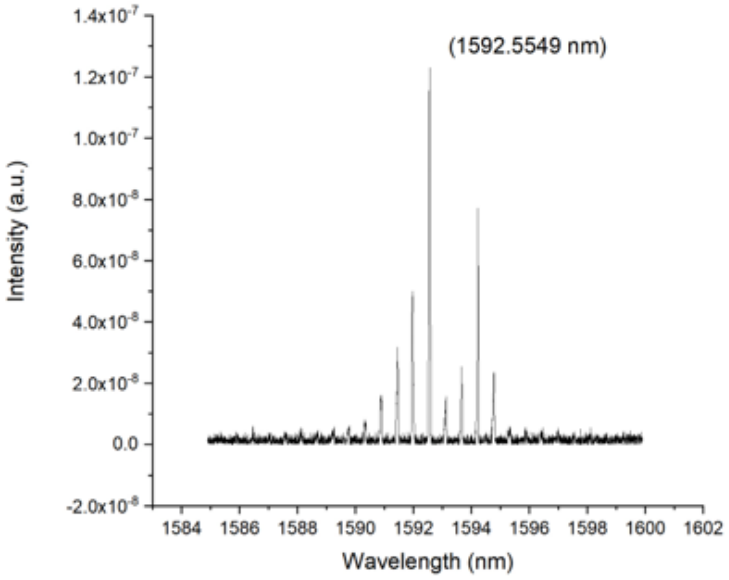

Figure 3.6: Figure 3.6: Optical emission spectra of the laser device with a cavity length of 0.666 mm, measured at $1.1 \times I_{th}$ using an optical spectrum analyser with 0.2 nm resolution.

3.5.4 I-V-L-T Laser measurements (Temperature Dependent Measurements)

The experimental setup for measuring the current-voltage-light characteristics as a function of temperature (I-V-L-T) uses a cryostat and a temperature controller. The

device is mounted inside an evacuated cryostat chamber, with one or two devices electrically connected at a time. The temperature of the device is controlled by a temperature controller, which allows the temperature to be varied between 300 K and 380 K. Current is provided to the device by a constant-current pulse generator. The chamber operates at reduced pressure, up to 4 x 10^{-4} mbar. A simple uncalibrated photodiode is used to collect the light signal.

3.5.5 Segmented Contact Method

The segmented contact method, which is a type of stripe-length method, is a technique used to measure the net-modal gain and absorption from the amplified spontaneous emission (ASE) emitted from the edge of a multi-segmented device [9]. Typically, this technique utilizes two equally long segments, referred to as section 1 (S1) and section 2 (S2), as illustrated in Figure 3.7. Figure 3.7 depicts the segmented contact device.

In this method, the ASE is measured as a function of the length of the pumped stripe. Therefore, a stripe with segmented contacts is used as it allows the stripe length to be varied. Each segment is electrically isolated and can be individually pumped. The ASE when sections are pumped individually and collectively are measured.

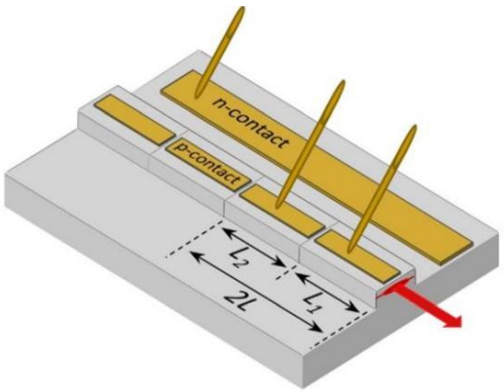

Figure 3.7: Diagram of the segmented contact device. Section 1 and section 2 have been bonded and can be pumped to produce ASE. Adapted from [6].

The segmented contact devices are fabricated from the same wafer used to fabricate the lasers and allows for representative characterization of the gain material. The gain measured using the segmented contact device should be representative of the gain within the fabricated lasers.

To measure the ASE, preventing cavity round-trip amplification is necessary to ensure that the light emitted from the front facet results from a single pass of the gain material. Therefore, this method is referred to as a single-pass measurement. To reduce optical feedback, additional steps are often taken, such as damaging the rear facet or cleaving the structure to have angled facets. Additionally, the segments near the rear facet are either unpumped or reverse biased to absorb any photons emitted in the backwards direction that may cause optical feedback.

The ASE is measured, allowing the extraction of gain and absorption from the ASE spectra [7]. The rate of electrical pumping significantly influences the population inversion level, and thus, the gain. For accurate measurement, it is crucial that the near-field, current, and voltage (IV) characteristics are identical for both sections. The device is placed on a holder, and the gain and absorption are measured across a range of bias currents provided by a pulse generator. These measurements are recorded using an oscilloscope as part of a semi-automated setup. An absorption filter wheel, controlled by a computer, is used to prevent the camera from becoming oversaturated. The incident light is focused onto a monochromator, which is then captured by an IR camera, calibrated using a reference [8].

The modal gain and absorption can be calculated from the ASE spectra by comparing the light intensity emitted from both segments. The modal gain is proportional to the ratio of the ASE spectra from pumping sections 1 and 2 combined, to the ASE from pumping section 1 with the same current density. The modal absorption is proportional to the ratio of the ASE spectra from pumping section 1 to the ASE from pumping section 2. The typical net gain and absorption are derived from Equations (3.2) and (3.3), with the complete derivation provided in reference [9],

$$(G - \alpha_i) = \frac{1}{L}\left[\frac{I_{S12}}{I_{S1}} - 1\right] \qquad (3.2)$$

$$(A + \alpha_i) = \frac{1}{L}\left[\frac{I_{S1}}{I_{S2}}\right] \qquad (3.3)$$

where, G is the modal gain, A is the modal absorption, α_i is the cavity loss, L is the cavity length and I_{S1}, I_{S2}, and I_{S12} are the measured ASE intensity spectra with section 1, section 2 and sections 1 and 2 pumped respectively.

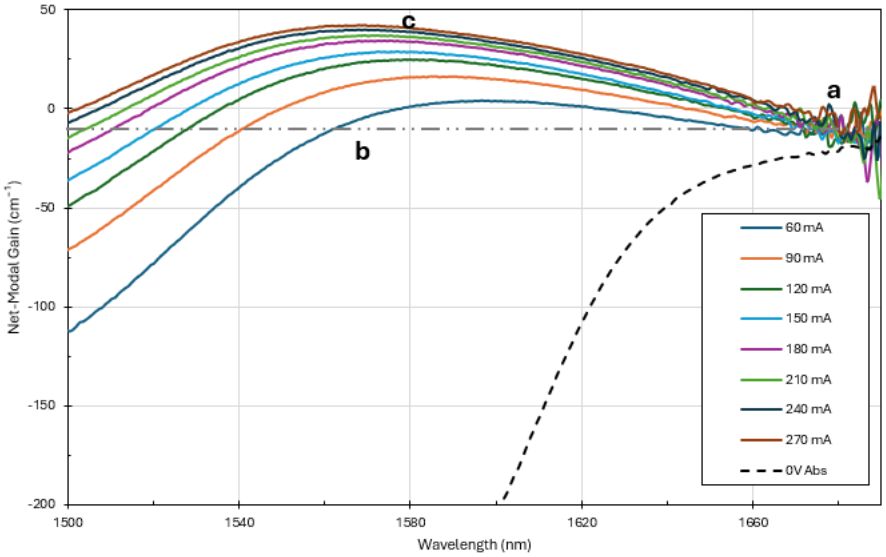

Figure 3.8 Shows the net modal gain and absorption from the ASE spectra.

The internal optical loss is determined from the long-wavelength region where the absorption and gain curves intersect (point *a* in the Figure above). The peak of the gain corresponds to the lasing wavelength (or what the lasing wavelength would be in an edge emitting laser) at the applied current. The point where the gain curve intersects the extended line of the absorption and gain curves in the short-wavelength range represents the transparency point (point *b*), while the peak of the net gain curve indicates the maximum gain (point *c*).

3.6 Chapter Summary

This chapter gave an overview of the epitaxial structures and fabrication processes of the devices utilized in this study. It details the experimental setup employed to gather the results presented in this thesis, which will be used in subsequent chapters to evaluate the performance of the materials under investigation. The chapter also describes the experimental setups used to measure power-current-voltage characteristics, wavelength, and near-field properties. Furthermore, it discusses the segmented contact technique used to measure modal gain.

References

1. Agrawal, G. P. & Dutta, N. K. *Semiconductor Lasers*. Springer Science & Business Media, (2013).

2. Blood, P. *Quantum Confined Laser Devices: Optical Gain and Recombination in Semiconductors*. vol. 23, OUP Oxford, (2015).

3. Ning, C.-Z. What is laser threshold? *IEEE Journal of Selected Topics in Quantum Electronics* 19, 1503604 (2013).

4. Rezende, S. M. *Optoelectronic Materials and Devices. In Introduction to Electronic Materials and Devices.* (pp. 261-344). Cham: Springer International Publishing. (2022).

5. Coldren, L. A., Corzine, S. W. & Mashanovitch, M. L. *Diode Lasers and Photonic Integrated Circuits*. vol. 218 John Wiley & Sons, (2012).

6. Li, Z., Shutts, S., Xue, Y., Luo, W., Lau, K.M. and Smowton, P.M. Optical gain and absorption of 1.55 μ m InAs quantum dash lasers on silicon substrate. *Applied Physics Letters,* 118(13). (2021).

7. Blood, P. Quantum Efficiency of Quantum Dot Lasers. *IEEE Journal of Selected Topics in Quantum Electronics* 23(6), 1-8, (2017).

8. Jarvis, L. *Active Region Doping Strategies in O-Band InAs/GaAs Quantum-Dot Lasers*. (Doctoral dissertation, Cardiff University). (2022).

9. Blood, P., Lewis, G.M., Smowton, P.M., Summers, H., Thomson, J. & Lutti, J. Characterization of Semiconductor Laser Gain Media by the Segmented Contact Method. in *IEEE Journal on Selected Topics in Quantum Electronics* vol. 9(5), 1275-1282 (2003).

Chapter 4: Characterization and understanding of 1.5 µm AlGaInAs/InP Quantum-Well Lasers

4.1 Introduction

While commercial 1.3µm quantum well (QW) lasers are still dominated by Aluminum Gallium Indium Arsenide (AlGaInAs) and Indium Gallium Arsenide Phosphide (InGaAsP) materials, grown on InP substrates some progress has been made with materials grown on GaAs [1-4], but such GaAs based lasers are even less effective at longer wavelengths.

At 1550 nm Aluminum Gallium Indium Arsenide (AlGaInAs) and Indium Gallium Arsenide Phosphide (InGaAsP) materials, grown on InP substrates, dominate Semiconductor lasers utilising strained quantum well QWs are still most used for optical fibre communications [5]. In this chapter QW InP based lasers are reported as a benchmark for the performance of the lasers of Chapters 6 and 7.

The aim of this chapter is to characterize 1.55 µm AlGaInAs/InP quantum-well lasers by conducting initial measurements at room temperature .This will involve examining structures with two different numbers of multi-quantum-well (MQW) in the active region, specifically, 6QW and 9QW oxide-isolated stripe lasers with varying cavity lengths (1000 µm, 666 µm, 500 µm, 400 µm, 333 µm, 285 µm, and 250 µm). In the next chapter, simulations of these structures using Nexnano software will be conducted to understand and improve their performance.

AlGaInAs can be grown on InP by using several methods including metal-organic chemical vapor deposition MOCVD techniques, which are the common growth methods. In this work, AlGaInAs 6QWs and 9QWs were grown by MOCVD.

4.2 Device structure

The epitaxial layers for the 6 and 9 QW structures were designed by Dr. Sam Shutts, grown by IQE Ltd and were fabricated into oxide isolated stripe lasers by Dr. Zhongming Cao. The geometry of the active region for the structure was chosen so that the maximum emission was in the spectral range of 1.55 µm using $Al_{0.070}Ga_{0.220}In_{0.71}As$ quantum wells separated by $Al_{0.240}$ $Ga_{0.280}In_{0.48}As$ barriers and InP cladding layers. The doping concentration and thicknesses for sample 6QW is shown in Table 4.1

Table 4.1: The structure details for sample 6QW

Layer No.	Repeats	Material	Thickness (nm)	Strain (%) t (+) c (-)	Doping(cm^{-3})
11	1	$InGa_{0.470}As$	140	0	2.00E+19
10	1	InP	1000		1.00E+18
9	1	InP	500		5.00E+17
8	1	$Al_{0.261}Ga_{0.210}In_{0.529}As$	150	0	
7	1	$Al_{0.240}Ga_{0.280}In_{0.48}As$	9	0.34	
6	6	$Al_{0.070}Ga_{0.220}In_{0.71}As$	6	-1.2	
5	6	$Al_{0.240}Ga_{0.280}In_{0.48}As$	9	0.34	
4	1	$Al_{0.261}Ga_{0.210}In_{0.529}As$	150	0	
3	1	InP	500		1.00E+18
2	1	InP	1000		1.50E+18
1	1	InP	100		3.00E+18

From bottom to top, the sample is grown on InP substrate followed by an InP buffer layer (100 nm) that is heavily n-doped with silicon (Si) dopants of 3.0×10^{18} cm^{-3}. This highly doped layer should facilitate good ohmic contacts. The InP lower cladding layer and guided layer is grown before the first barrier. The active region consists of a narrow bandgap in the QW and a higher bandgap for barrier materials with a QW width

of 6-nm and composition of $Al_{0.070}Ga_{0.220}In_{0.71}As$ separated by 9-nm $Al_{0.240}Ga_{0.280}In_{0.48}As$ barrier material and an InP top cladding layer. Finally, a highly p-doped layer, with Zinc (Zn) dopants of 2.0 x 10^{19} cm^{-3}, contact layer completed the device structure.

4.3 Device Fabrication

The fabrication of the devices used in this work was completed and processed at the cleanroom facility at Cardiff University. The oxide isolated stripe structure is illustrated in Figure 4.1.

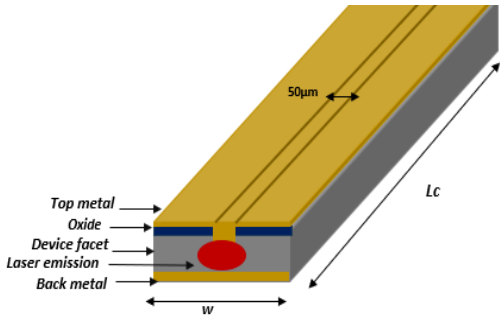

Figure 4.1. Oxide stripe laser.

Table 4.2: Basic processing steps for the oxide-isolated stripe QW laser diode.

No.	Steps
1	Wafers were cleaved into 12 x 12 mm tiles.
2	Tiles were cleaned via standard cleaning process (acetone, methanol and isopropanol)
3	A thin SiO_2 isolation layer was deposited via electron beam physical vapor deposition.
4	Device pattern was defined through a standard photolithography process.
5	A p-type metallization layer of Ti/Pt/Au was deposited via electron beam physical vapor deposition.
6	Unwanted metal was removed by lift-off process.
7	The substrate was thinned to 120 µm by lapping tool.
8	A n-type metallization layer of AuGe/Ni/Au was deposited on the backside of tiles using thermal evaporation.
9	The tiles were annealed at 380 °C to form ohmic contact
10	Laser bars were cleaved into different cavity lengths, ranging from 250 to 3000 µm, without facet coating.
11	cleaved samples were mounted to TO header and characterized under pulsed generator.

4.4 Measurement of P-I-V characteristic

The properties of the AlGaInAs laser diodes were studied using key techniques, as detailed in the third chapter and at room temperature. The measurement focused on the optical power-current-voltage P-I-V characteristics of the laser devices and near-field measurements. The current source is used in pulse mode with a pulse width of 1 us and pulse rate /frequency of 5 kHz.

4.4.1 I-V characteristic at the room temperature

The I-V characteristics of the 9 QW structure measured at 300 K are illustrated in Figure 4.2. Initially, the diode shows a very low current, demonstrating typical diode

behaviour. However, as the voltage increases, the current rises significantly, starting at approximately 0.7 V. This sharp increase is attributed to the voltage exceeding the built-in potential within the p-i-n junction, enabling higher carrier injection and thus leading to a rapid increase in current.

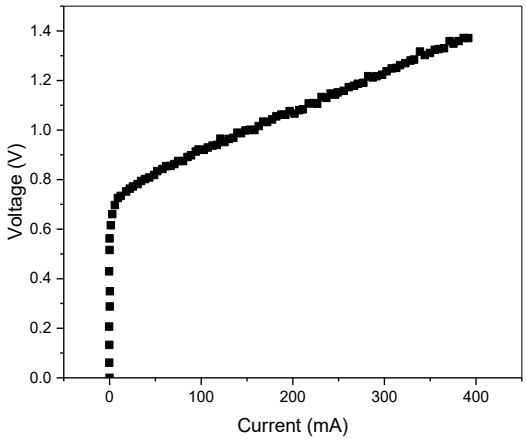

Figure 4.2: The I-V characteristic for structure 9QW laser diode.

4.4.2 P-I characteristics at room temperature

The P-I characteristic for 9QW OS laser diode at a temperature of 300 K is presented in Figure 4.3 for determining key laser properties of the studied structures such as the threshold current. At low current levels, a small amplitude of light output is observed, which is attributed to spontaneous emission. This emission occurs as the initial injection current begins to excite the laser diode. Threshold is achieved when the optical gain equals the optical losses within the cavity. Beyond this point, the laser transitions into its lasing mode, and the light output increases super-linearly, as depicted in Figure 4.3. The specific current at which laser emission begins is referred to as the threshold current. This critical parameter marks the point where stimulated emission dominates, and the laser becomes fully operational.

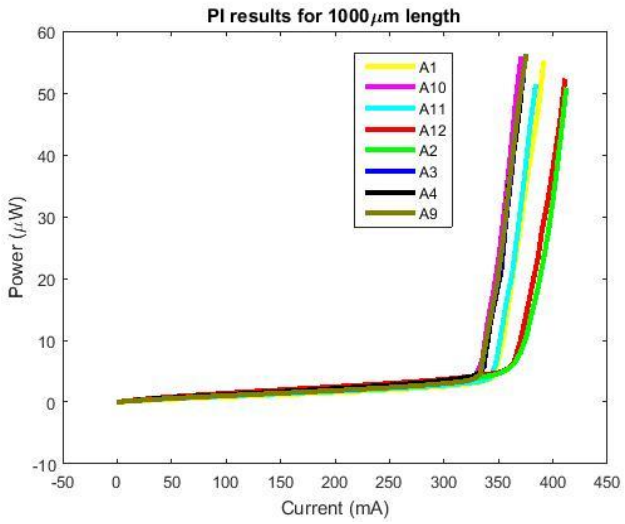

Figure 4.3: Power-current characteristic for 9QW-OS taken at 300 K.

4.4.3 Determination of threshold current from P-I characteristic

The threshold current is determined from the P-I (or L-I) characteristic curve by drawing a straight line along the linear region of the curve above the threshold. The point where this line intersects the current axis corresponds to the threshold current, as illustrated in Figure 4.4. For the laser diode under study, the threshold current obtained from the graph is I_{th}=323 mA.

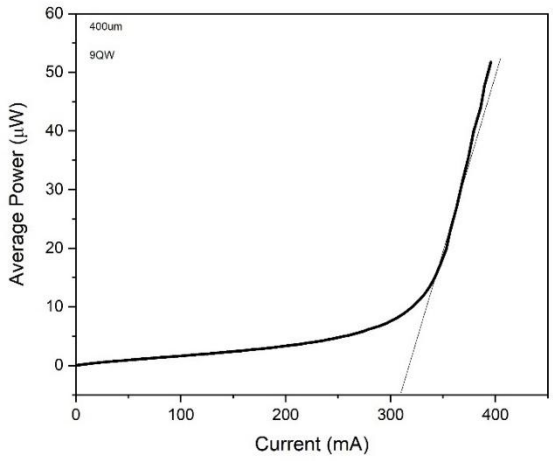

Figure 4.4: Threshold current determination from the P-I characteristic for 9QW-OS laser at 300 K.

4.4.4 Threshold Current as a Function of Cavity Length

Figure 4.5 illustrates the relationship between threshold current and cavity length for OS structures with different numbers of quantum wells QW. The data show that the threshold current increases with cavity length. For all cavity lengths, except the shortest, the 9 QW structure exhibits a higher threshold current compared to the 6 QW structure. The increase in threshold current with cavity length is simply because there is more material to drive to population inversion.

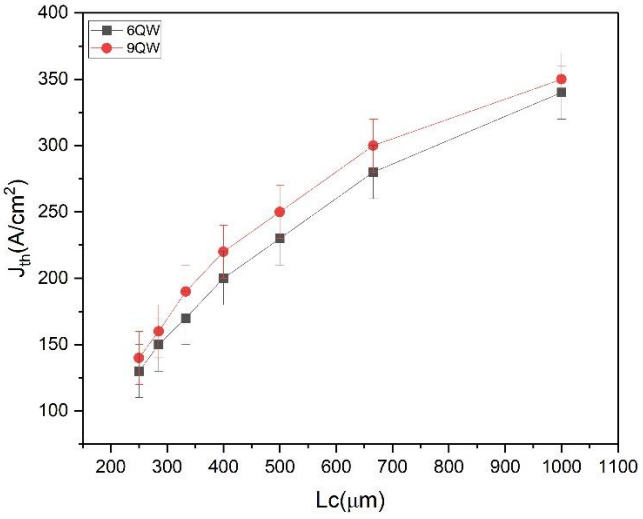

Figure 4.5: Threshold current vs. cavity length for 6QW and 9QW-OS.

4.4.5 Calculation of threshold current density

The threshold current density J_{th} is defined as the threshold current per unit area and provides a better description of material quality. The current of Figure 4.5 is transformed into current density in Figure 4.6, by determining the current spreading using Equation (3.1) and near-field measurements, as mentioned in Chapter 3.

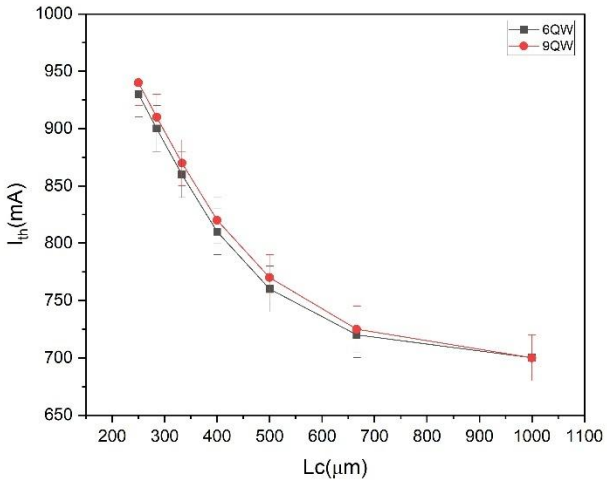

Figure 4.6: Threshold current density vs. cavity length for 6QW and 9QW-OS.

4.5 Determination of Gain Parameter (Go)

The relationship between threshold current density versus the reciprocal of the cavity length L_C, the slope is obtained. With knowledge of the mirror reflectivity, and the number of QW the gain parameter, G_0, can be calculation using the following Equation (2.19) [6].

And by plotting the threshold current density against the reciprocal of the cavity length the slope of the linear fit provides a means to calculate Go. Figures 4.7 and 4.8 illustrate these plots and the derived gain parameters.

The gain parameter was determined for each structure as follows (per QW layer):

The gain parameter obtained using the Equation (2.19) and data for all structure (per layer) is 72.88 ±7.92 (12.15±1.32) cm^{-1} for the 6QW and 94.36±18.48(10.48+2.05) cm^{-1} for the 9QW. The higher gain parameter for the 9 QW structure reflects the increased volume of the gain medium, which enhances optical amplification [7,8].

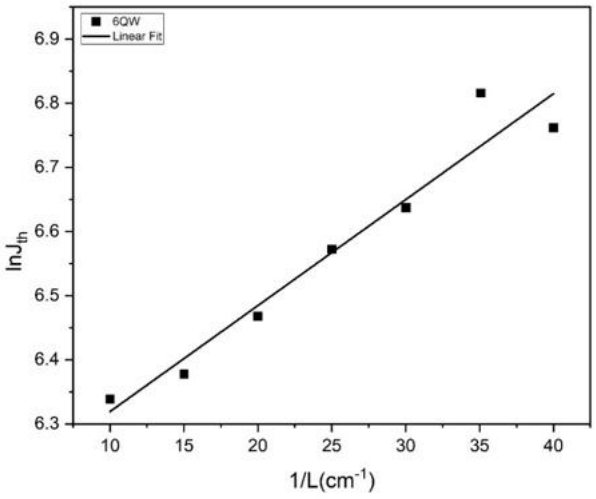

Figure 4.7: Threshold current density versus the reciprocal of the cavity length for 6QW- OS

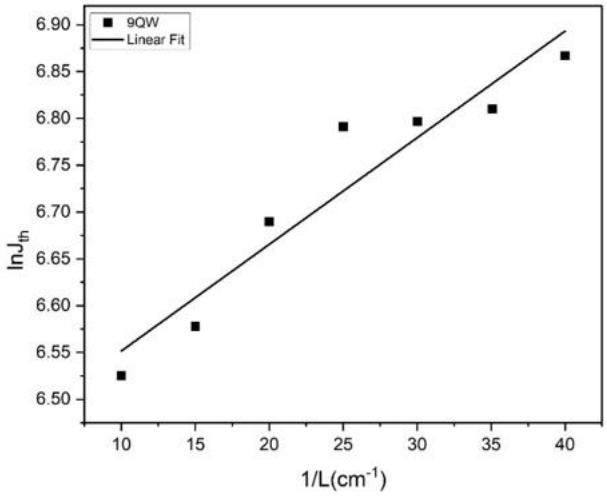

Figure 4.8: Threshold current density versus the reciprocal of the cavity length for 9QW OS.

4.6 Summary

In this chapter, the power-current characteristics of quaternary AlGaInAs/InP multi-quantum-well MQW laser diodes with six and nine quantum well QW layers were analyzed. The investigation revealed that the gain parameters were highly dependent on the number of quantum wells in the active region. The structures with six and nine QW layers exhibited high gain coefficients, measured at 72.9 cm^{-1} and 94.4 cm^{-1}, respectively and the values per layer of 12.2±1 cm^{-1} for the 6QW and 10±2 for the 9QW give a benchmark for the results in later Chapters.

The results presented in this chapter, specifically the high gain coefficients for the 6QW and 9QW AlGaInAs/InP MQW laser diodes, align with the general trends reported in literature [1-4]. As expected, an increase in the number of quantum wells leads to an enhancement in the overall gain. This is because more quantum wells typically provide a larger number of available states for electron-hole recombination, thereby increasing the overall gain in the active region. The observed values of 72.9 cm^{-1} for the 6QW and 94.4 cm^{-1} for the 9QW laser diodes are consistent with the higher gain values typically seen in multi-quantum-well structures compared to single quantum well lasers, where the gain coefficient is generally lower due to the limited number of available states for recombination. Furthermore, the per-layer gain coefficients of 12.2 ± 1 cm^{-1} for the 6QW structure and 10 ± 2 cm^{-1} for the 9QW structure are consistent with trends observed in similar MQW systems. In these systems, adding additional quantum wells typically leads to a proportional increase in gain, but with diminishing returns as the number of quantum wells increases. This is due to factors such as decreased confinement factor per QW, increased carrier leakage and recombination losses in thicker quantum well structures, which can slightly reduce the per-layer gain as the number of wells increases. In the literature, similar MQW structures, particularly those based on III-V compounds like AlGaInAs/InP have demonstrated higher performance characteristics, with reported high gain coefficients[1-4]. The gain values observed in this study 72.9 cm^{-1} for 6QW and 94.4 cm^{-1} for 9QW are therefore in good agreement with these results, supporting the notion that these particular MQW structures are well-suited for high-performance laser applications.

References

1. Liu, G. T., Stintz, A., Pease, E. A., Newell, T. C., Malloy, K. J., & Lester, L. F. 1.58-µm lattice-matched and strained digital alloy AlGaInAs-InP multiple-quantum-well lasers. *IEEE Photonics Technology Letters*, *12*(1), 4-6. (2000).

2. Selmic, S. R., Chou, T. M., Sih, J., Kirk, J. B., Mantle, A., Butler, J. K., ... & Evans, G. A. Design and characterization of 1.3-/spl mu/m AlGaInAs-InP multiple-quantum-well lasers. IEEE Journal of selected topics in Quantum Electronics, 7(2), 340-349. (2001).

3. Kuo, Y. K., Yen, S. H., Yao, M. W., Chen, M. L., & Liou, B. T. Numerical study on gain and optical properties of AlGaInAs, InGaNAs, and InGaAsP material systems for 1.3-µm semiconductor lasers. *Optics communications*, 275(1), 156-164. (2007).

4. Peng, T. C., Huang, Y. H., Yang, C. C., Huang, K. F., Lee, F. M., Hu, C. W., ... & Ho, C. L. Low-cost and high-performance 1.3-µm AlGaInAs-InP uncooled laser diodes. *IEEE photonics technology letters*, 18(12), 1380-1382. (2006).

5. Akram, M. N., Silfvenius, C., Kjebon, O., & Schatz, R. Design optimization of InGaAsP–InGaAlAs 1.55 µm strain-compensated MQW lasers for direct modulation applications. *Semiconductor science and technology*, 19(5), 615. (2004).

6. Blood, P. *Quantum Confined Laser Devices: Optical gain and recombination in semiconductors* (Vol. 23). OUP Oxford. (2015).

7. Li, E. H. Material parameters of InGaAsP and InAlGaAs systems for use in quantum well structures at low and room temperatures. *Physica E: Low-dimensional systems and Nanostructures*, *5*(4), 215-273. (2000).

8. Celebi, F. V. A different approach to gain computation in laser diodes with respect to different number of quantum-wells. *Optik,* 116(8), 375-378. (2005).

Chapter 5: AlGaInAs-InP Lasers Operating at 1.55 µm

5.1 Introduction

The demand for high-performance active optical components, such as semiconductor lasers, light-emitting diodes, mode-locked lasers, semiconductor optical amplifiers, and modulators, is growing significantly[1-3]. This is driven by the demand for large bandwidths in the 1.55 µm C-band optical communication window to meet the requirements of the exponentially growing internet and mobile connectivity market. Quantum well QW laser structures based on the InP material system are predominantly used for this wavelength and typically feature one of two different barriers and waveguide materials: (i) AlGaInAs and (ii) InGaAsP. Under high-temperature operation AlGaInAs structures are expected to have reduced carrier leakage, and therefore improved efficiency, resulting from the larger conduction band offset (ΔE_C=0.72Eg) at the heterojunctions compared to the smaller conduction band offset (ΔE_c =0.4Eg) of GaInAsP /InP [4-6].

The goal of this section is to design multiple-quantum-well (MQW) AlGaInAs–InP 1.55 µm lasers that incorporate an AlInGaAs barrier and waveguide, along with an additional electron blocker layer (EBL) on the p-side. The stopper layer should not obstruct carrier injection into the active region but should minimize the thermionic emission of carriers from the active region. As a result, the use of stopper layers in laser structures can enhance the performance of AlInGaAs-based lasers by reducing leakage current from the active region and increasing the internal quantum efficiency. [7].

To compare structures with and without electron stopper layer on the p-side, we simulate performance using the NextNano software package and monitor leakage current density as a function of Fermi-level separation, which we use as an indicator of optical gain.

5.2 Device structure

5.2.1 Original structure

The structure of Table 4.1(from the previous chapter) for the 6QW sample is used. The schematic band diagram for this device structure is shown in Figure 5.1.

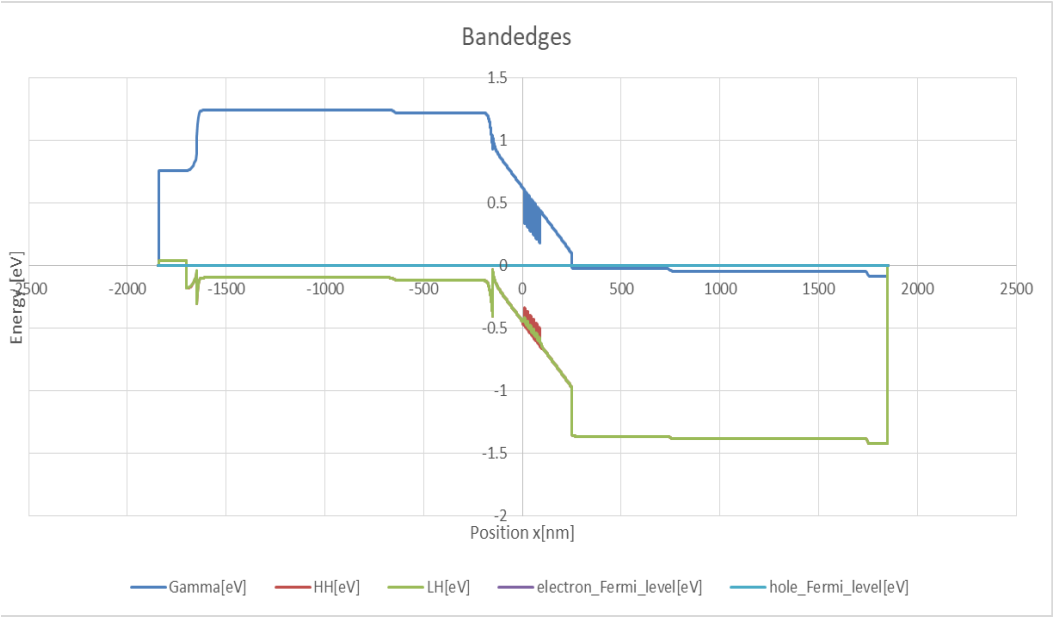

Figure 5.1: Schematic band edges for AlInGaAs/InP QWs from NextNano.

5.2.2 Simulation

Nextnano is a simulation software designed for electronic and optoelectronic semiconductor nanodevices, focusing on quantum effects in quantum wells. It supports 1D, 2D, and 3D simulations of various semiconductor materials and uses a quantum mechanical approach based on the 8-band k·p model, considering factors such as strain, piezoelectric charges, and magnetic fields [8].

The software handles both equilibrium and nonequilibrium conditions, solving Schrödinger-Poisson and current continuity equations. Input files define device geometry and materials, while output results include electrostatic potential, electric

fields, and recombination rates. Nextnano has been used to model the effects of gain materials and barriers on device performance, particularly for analysing leakage currents and optical gain.

5.2.3 Simulation to optimization of the structure

The main objective is to improve performance of original structure in terms of optical gain through a simple way by adding an electron-stopper (e-stopper) layer to increase the electron confinement in the MQW of long-wavelength lasers is proposed by introducing an $Al_{0.05}In_{0.05}As$ electron stopper with 12nm width and p-doped, 2.0 x $10^{17}cm^{-3}$ on the p-side. Figure 5.2 and Table 5.1 appear the comparison of the band diagram of laser structures with and without e-stopper. The doping level in the EBL affects the valence band barrier, where higher p-type doping enhances band bending and raises the VB edge, reducing the barrier for hole injection. This improves radiative recombination and optical gain.

Table 5.1 a-structure details for sample 6QW without EBL and b- structure 6QW with EBL

a

Description	Material
Contact-metal	InGaAs
U-cladding	InP
Waveguide	AlGaInAs
Barrier×6	**AlGaInAs**
QW×6	**AlGaInAs**
Barrier×	**AlGaInAs**
Waveguide	AlGaInAs
L- cladding	InP
Substrate	InP

b

Description	Material
Contact-metal	InGaAs
U-cladding	InP
Waveguide	AlGaInAs
EBL	**AlInAs**
Barrier×6	**AlGaInAs**
QW×6	**AlGaInAs**
Barrier×	**AlGaInAs**
Waveguide	AlGaInAs
L- cladding	InP
Substrate	InP

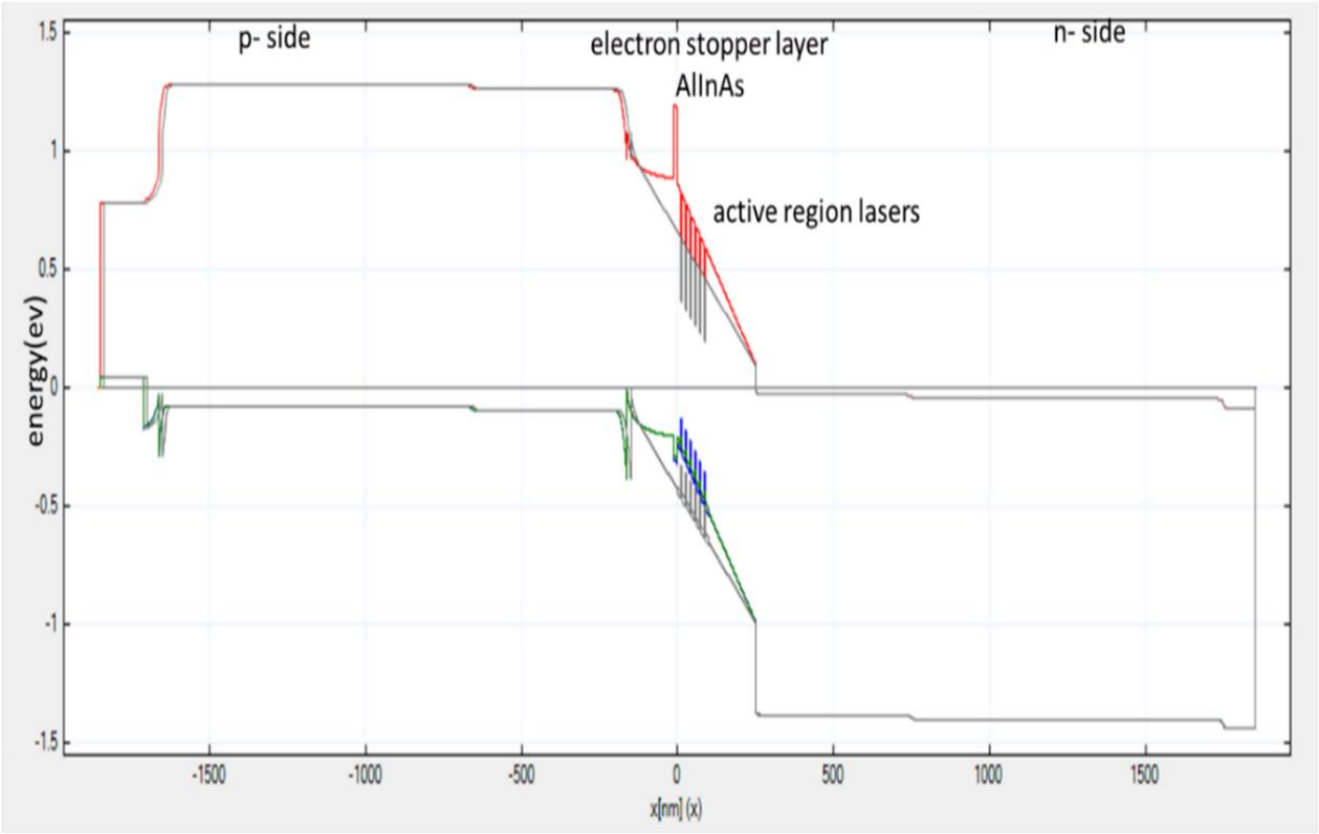

Figure 5.2: Band diagram of a laser structure with and without e-stopper at zero bias.

Electrons are injected into the MQW from n-InP on the left side and mostly recombine within the MQW. However, a small portion of the electron current remains on the right side, suggesting electron leakage into the p-InP cladding, as shown in Figure 5.3.

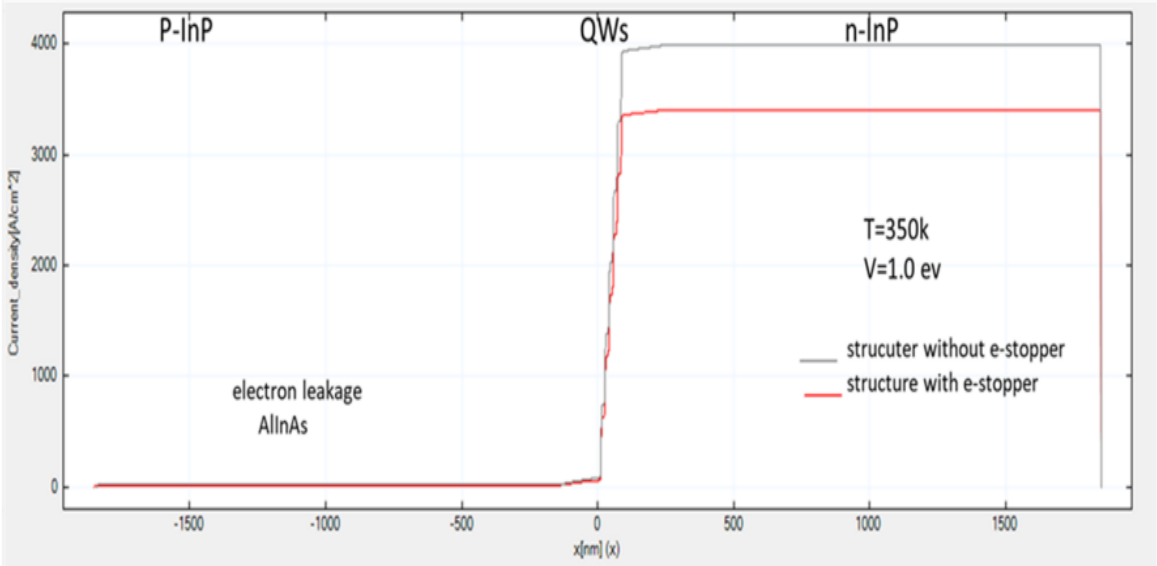

Figure 5.3: Electron current density without and with e-stopper as a function of the position.

Figure 5.4. shows the radiative recombination rate of the MQW with and without EBL vs. bias for different temperatures.

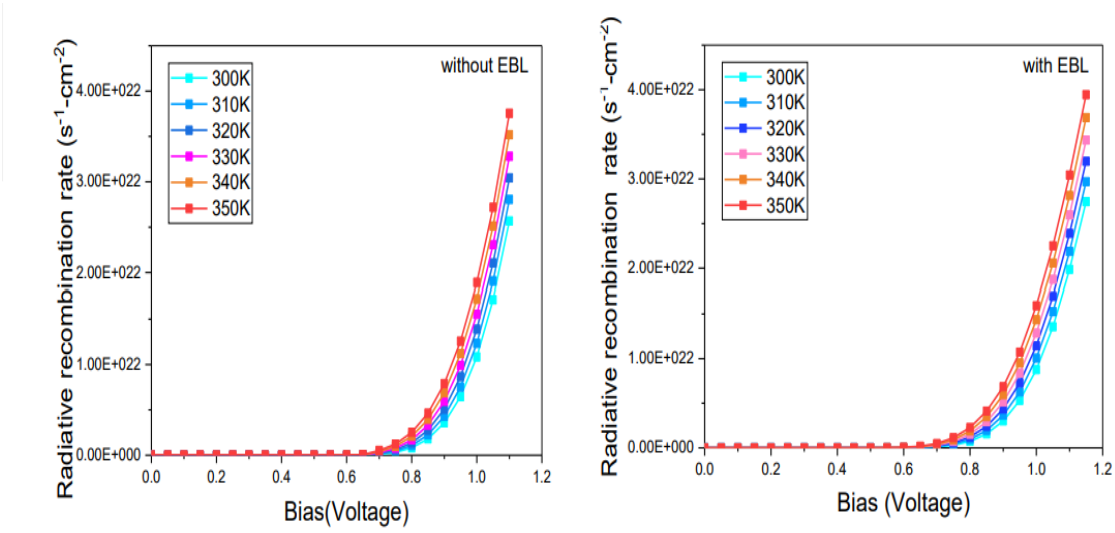

Figure 5.4: Radiative recombination rate of the MQW with and without EBL vs. bias for different temperatures.

In Figure 5.4, we observe the radiative recombination rate for the MQW (Multiple Quantum Well) structure with, and without the EBL (Electron Blocking Layer) as a function of bias voltage for different temperatures. It is evident that the radiative recombination rate is consistently higher when the EBL is present (right graph) compared to when it is absent (left graph). For all temperatures (300K to 350K), the presence of the EBL leads to an increase in the radiative recombination rate. The enhancement is more noticeable at higher bias voltages; for instance, at around 1.0V or higher, the difference in recombination rates between the two conditions (with and without EBL) becomes significantly large. The enhancement in the radiative recombination rate with the EBL is consistent across the different temperatures. At lower temperatures (300K-320K), the difference in the recombination rate is relatively smaller, but as the temperature increases (330K-350K), the enhancement becomes more pronounced. This suggests that EBL plays a more significant role at higher temperatures, potentially due to improved carrier confinement and recombination characteristics. Overall, the radiative recombination rate is clearly enhanced with EBL, and this enhancement becomes more significant as the temperature increases, which aligns with the physical expectation that the EBL would improve recombination efficiency at higher temperatures due to better electron confinement and reduced non-radiative losses.

5.3 Simulation results and Discussion

Leakage current increases with temperature due to the larger number of carriers at higher energy but is reduced by EBL as shown in Figure 5.5.

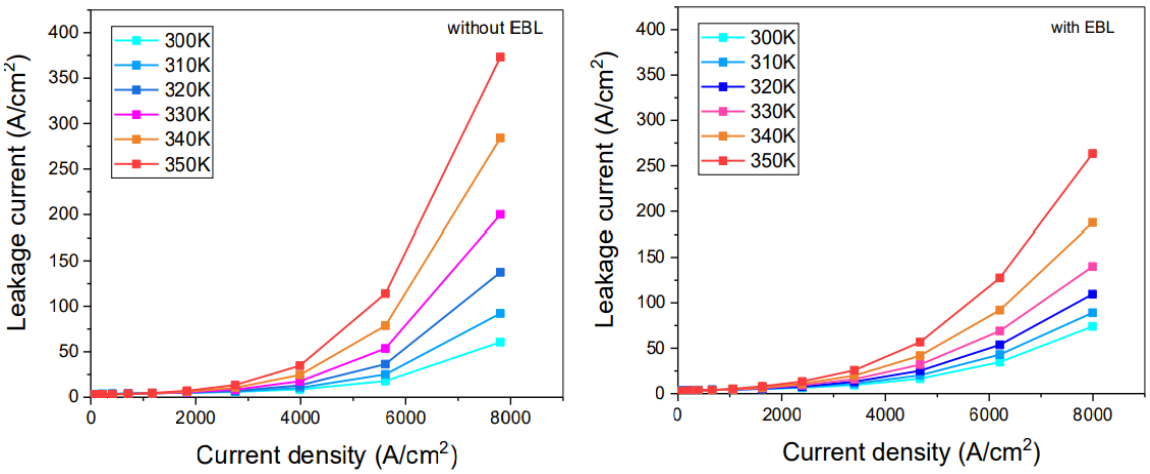

Figure 5.5: Leakage current vs current density with and without EBL for different temperatures.

Figure 5.5 shows that leakage current increases with temperature due to more carriers at higher energy, but the presence of the Electron Block Layer (EBL) reduces this increase. Without the EBL, the leakage current rises sharply with both temperature and current density, particularly at higher temperatures (340K and 350K). However, with the EBL, the leakage current is significantly reduced, especially at high temperatures and current densities, indicating that EBL effectively mitigates the temperature-dependent rise in leakage current and stabilizes device performance.

However, this does not necessarily translate into better laser performance. It may be that the EBL is also increasing current density or reducing the carrier density in the active region. Thus, to be sure we use radiative recombination within the QWs as an indicator of the gain in the QWs is shown in Figure 5.6 as the two processes are intimately related. A lower leakage current at the same radiative current density should indicated better performance in real devices.

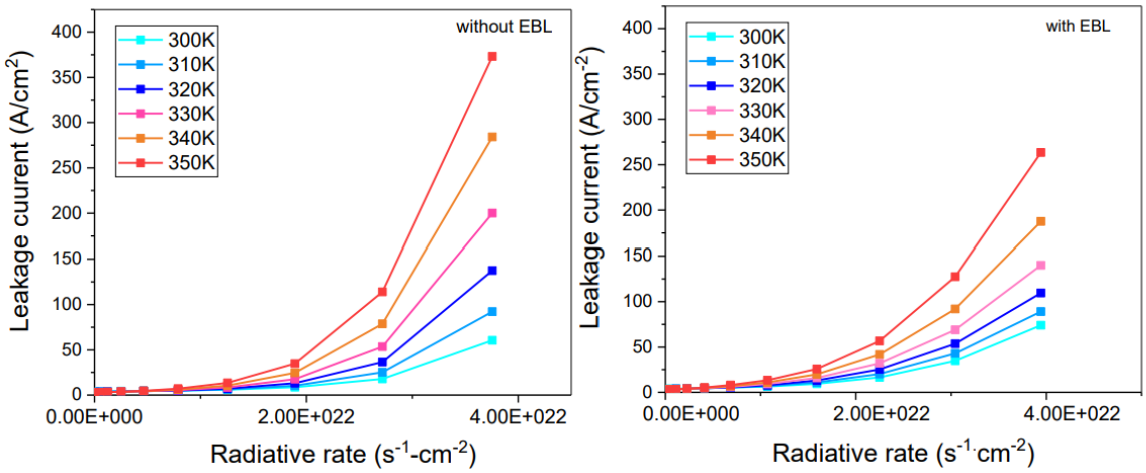

Figure 5.6: Leakage current vs radiative recombination rate with and without EBL for different temperatures.

The figure shows the relationship between leakage current and radiative recombination rate under two conditions: without and with the EBL (Electron Barrier Layer), across different temperatures (ranging from 300K to 350K). The left graph displays the leakage current without the EBL, where a marked increase in leakage current is observed with rising temperature and radiative rate. This suggests that at higher temperatures, the material experiences an increased recombination rate, leading to a higher leakage current. In the right graph, where EBL is present, the leakage current is notably lower across all temperatures. This indicates that the EBL effectively reduces the leakage current by limiting the recombination process, particularly at higher radiative rates. The comparison between the two graphs highlights the significant role of EBL in mitigating leakage current, especially at higher temperatures.

5.4 Summary

The AlInGaAs/InP multiple quantum well (MQW) laser structure shows strong potential for achieving optimized performance at long wavelengths, particularly when incorporating an electron-stopper (e-stopper) layer. Introducing a thin, p-doped AlInAs e-stopper on the p-side significantly improves electron confinement without impeding carrier injection into the active region. This added layer enhances the band structure by increasing the valence band edge, thereby improving hole injection and promoting stronger radiative recombination within the MQWs. As a result, the optical gain of the structure is noticeably increased, particularly at elevated temperatures and higher bias conditions, where performance typically degrades. The simulations show that the e-stopper layer effectively suppresses electron leakage into the cladding region, a common issue that reduces efficiency in high-temperature operation. Furthermore, the radiative recombination rate, which directly correlates with laser output, remains consistently higher when the e-stopper is included, indicating better utilization of injected carriers. In addition to enhancing gain, the e-stopper substantially reduces leakage current, which otherwise rises with temperature and current density due to increased carrier energy. This reduction in leakage current, especially when compared at equal levels of radiative recombination, reflects a more efficient carrier confinement and recombination process within the active region. To evaluate the operation of the laser diode, AlInGaAs/InP MQW highlights a good structure to achieve a highly optimized laser performance suitable for long wavelengths. The results show that the use of an electron stopper layer in the AlInGaAs laser structure does not hinder the injection of carriers into the active region, while simultaneously significantly reducing the thermionic emission of carriers from the active layer, particularly at elevated temperature; this will lead to improving threshold current density and efficiency of devices. While this idea will not be implemented in real devices in this thesis, it does offer potential as a way to further improve the performance of the samples that will be studied in the next two chapters. These findings provide valuable guidance for future design strategies aimed at enhancing the thermal stability and overall efficiency of long-wavelength MQW laser diodes.

References

1. Selmic, S. R., Chou, T. M., Sih, J., Kirk, J. B., Mantle, A., Butler, J. K., ... & Evans, G. A. Design and characterization of 1.3-/spl mu/m AlGaInAs-InP multiple-quantum-well lasers. *IEEE Journal of selected topics in Quantum Electronics*, *7*(2), 340-349. (2001).

2. Coldren, L. A., Corzine, S. W., & Mashanovitch, M. L. *Diode lasers and photonic integrated circuits*. John Wiley & Sons. (2012).

3. Blood, P. *Quantum Confined Laser Devices: Optical gain and recombination in semiconductors.* (Vol. 23). OUP Oxford. (2015).

4. Kazarinov, R. F., & Belenky, G. L. Novel design of AlGaInAs-InP lasers operating at 1.3um. *IEEE journal of quantum electronics*, *31*(3), 423-426. (1995).

5. Takemasa, K., Munakata, T., Kobayashi, M., Wada, H., & Kamijoh, T. 1.3-μm AlGaInAs-AlGaInAs strained multiple-quantum-well lasers with a p-AlInAs electron stopper layer. IEEE Photonics Technology Letters, 10(4), 495-497. (1998).

6. Jin, J., & Tian, D. Improved performance of 1.3 μm InGaAsP–InP lasers with an AlInAs electron stopper layer. *Semiconductor science and technology*, 18(11), 960. (2003).

7. Abraham, P., DenBaars, J., & Bowers, J. E. Improvement of Internal Quantum Efficiency in 1.55 μm Laser Diodes with InGaP Electron Stopper Layer. Japanese journal of applied physics, 38(2S), 1239. (1999).

8. https://www.nextnano.de/manual

Chapter 6: Characterisation of InAs/InP Lasers and Gain Material: Growth 1

6.1 Introduction

This chapter describes the work done to develop InAs quantum dot/dash (QD) structures on InP substrates, with the goal of eventually growing InAs QDs directly on silicon substrates. As discussed in Chapter 1, growing QDs on silicon is more difficult than on their native III-V substrates like InP, due to technical challenges such as the lattice mismatch [1–3]. Therefore, we began by examining QD structures on native III-V (InP) substrates to better understand how design and growth conditions affect device performance before, in future work, moving on to growth on silicon. To optimize the performance of epitaxial laser structures with the desired characteristics, such as low threshold current density, high modal gain, high efficiency, and the correct operating wavelength, it is important to know how changes in the design and growth process impact these properties. Although the focus here was to develop suitable InAs QD laser structures on InP, this research built upon findings from a previous study characterising the optical gain and absorption of 1.55 μm InAs/InGaAs structures grown directly on a silicon substrate [4]. The aim of that study was to understand their intrinsic performance, but it became clear that a more thorough study was required. In addition, the growth of the material for this study was done in Cardiff University by colleagues in the group of Dr Qiang Li. The active region previously used consisted of 3 layers of InAs dash-in-well (DWELL) layers, separated by InAlGaAs barriers, and grown on (001) Si substrates. The optical net gain and absorption was measured using the variable stripe-length method at temperatures ranging from 20 °C to 80 °C. It showed that as the temperature was increased, the peak optical net gain decreased, with a drop from 22.2 cm^{-1} at 20 °C to 0.2 cm^{-1} at 80 °C, for an injection current density of 1.67kA/cm^2. At 20°C, the internal optical loss was measured to be ~17 cm^{-1} [4]. The threshold current densities were high, probably due to a number of factors such as high defect density and further optimization was needed to the design and growth to reduce the defect density, to improve laser performance and reduce the threshold current density.

In this chapter we investigate the performance of lasers using similar designs but where there is an additional $In_{0.45}Ga_{0.55}As$ capping layer above each layer of QDs, with the aim of increasing the carrier confinement and decreasing optical scattering loss. We aim to investigate the temperature dependence of various laser characteristics, such as the emission wavelength and threshold current density, for different cavity lengths. This chapter is organized as follows: first, the design and composition of the epitaxial layers used in this study is described. The next section presents laser results showing the temperature dependence of the threshold current density and emission wavelength, for different cavity lengths. Finally, measurements of optical gain and absorption using the segmented contact method are reported.

6.2 Epitaxial Structure

The InAs QD laser structure, used to fabricate the devices discussed in this chapter, was grown by Dr. Qiang Li's group at Cardiff University on n-InP (001) substrates by metal organic chemical vapor deposition (MOCVD). A dot/dash-in-well (DWELL) structure was used for the active region, which consisted of self-assembled InAs dots/dashes embedded in $In_{0.45}Ga_{0.55}As$/InAlGaAs strained QWs for carrier confinement similar to the previous study [4]. InAs QDs were grown, via the Stranski-Krastanov process, onto a 2nm $In_{0.45}Ga_{0.55}As$ pre-layer which helps address issues related to surface quality, strain, and defects to improve the quality of the subsequent layers. The QD structures were capped with a 0.7 nm $In_{0.45}Ga_{0.55}As$ layer. This capping layer should help in controlling strain, reducing surface roughness, and improving the overall quality of the material [5]. These DWELL layers were separated by 40nm $In_{0.52}Al_{0.26}Ga_{0.22}As$ barrier layers and this was repeated for five QD layers. The dot density of an uncapped test structure was measured using atomic force microscopy (AFM) and found to be 2.4×10^{10} /cm^2 as shown Figure 6.1a. It should be noted that the AFM measurement is performed on structures grown under the same conditions but where growth is stopped immediately above the layer of QDs. Therefore, the result of the AFM measurement does not necessarily represent the material that will be realised in the full laser structures. The active region was surrounded by 240 nm un-doped $In_{0.52}Al_{0.26}Ga_{0.22}As$ layers which formed the separate confinement heterostructure (SCH), and the p-InP and n-InP were used as the upper- and lower-

cladding layers which formed the rest of the waveguide. P-type $In_{0.53}Ga_{0.47}As$ was deposited as the top cap layer. The structure was grown at 680 °C. A schematic diagram of the structure is provided in Figure 6.1b. The wafer was processed into broad area laser devices at Cardiff University by Dr. Zhongming Cao using standard fabrication processes. A set of 2000µm to 300µm long, 50-um wide oxide-isolated stripe Fabry-Perot FP laser devices were cleaved and were left with uncoated facets. The cleaved mirrors had a reflectivity of approximately 28%. The devices were mounted on a copper heat sinks using silver loaded epoxy and gold-wire-bonded.

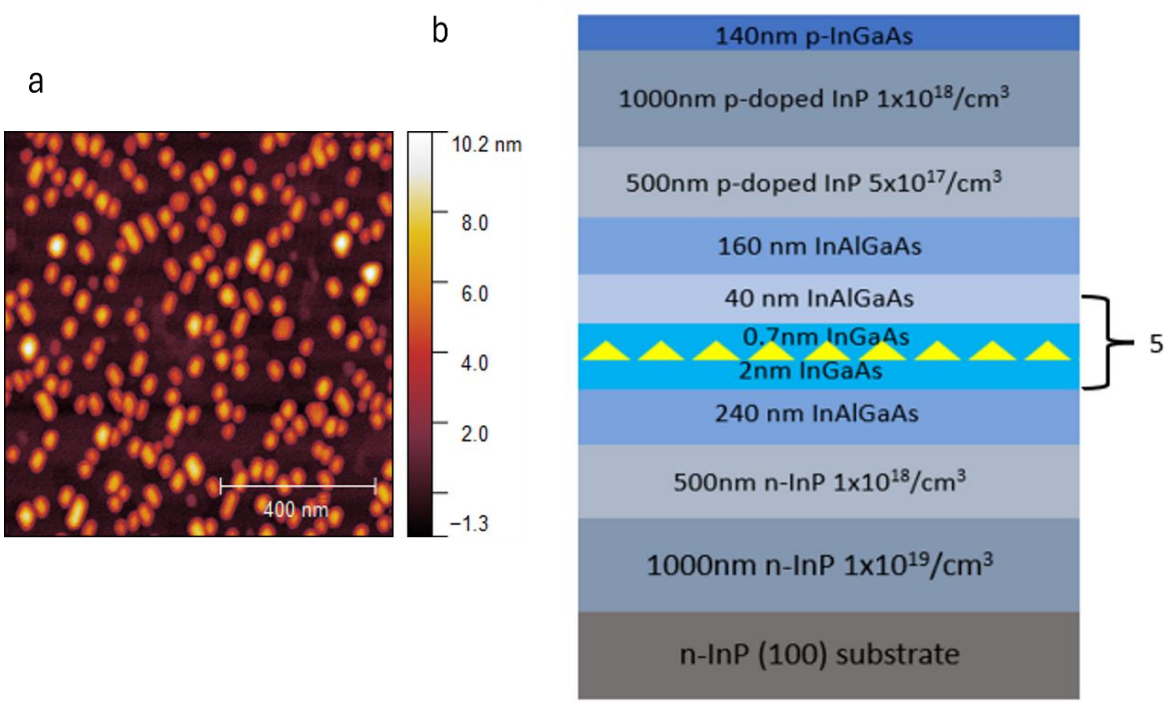

Figure 6.1: a) AFM image of uncapped InAs QDs grown on InP substrate, Images were supplied by Dr. Shangfeng Liu. b) Schematic diagram of the epitaxial structure (not to scale)

6.3 Characterisation methods of III-V semiconductors (Dots, Dashes or Wells)

Transmission electron microscopy (TEM) is used prior to device fabrication to evaluate the quality of materials grown by MOCVD. The TEM Images are shown in Figure 6.2.

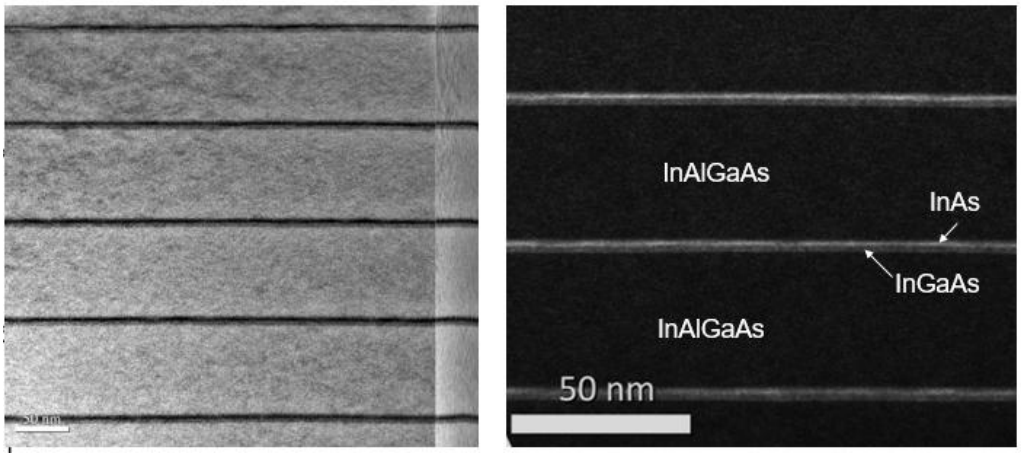

Figure 6.2: TEM images showing the bright field (left) and dark field (right) of the active layer of structure. Images were supplied by Dr. Qiang Li. TEM and AFM measurements are measured on samples grown under similar conditions.

Transmission electron microscopy TEM is used to image the structure formed during material growth and to identify whether quantum dots QDs, quantum dashes QDHs, or quantum wells QWs have been created. TEM works by transmitting electrons through the sample to produce an image, which can be captured in either "bright field" or "dark field" mode. The mode selection depends on whether the electrons are collected directly or at a small angle to capture scattered electrons. With its extremely short electron wavelength, TEM can achieve nanometer-scale resolution, enabling the direct observation of atomic arrangements within the crystal structure.

The TEM images presented in Figure 6.2 reveal the five layers of material in the active region of the device. While quantum dots can be challenging to identify in TEM images, the use of dark field imaging provides enhanced resolution. However, the

results are not really clear, and the presence of dots and dashes cannot be confirmed although there is some variation in the layer that should contain them.

6.4 Measurement Results

The fabricated devices were measured using the techniques defined in Chapter 3 and include Light-Current-Voltage-Temperature (L-I-V-T) measurements and the segmented contact method (SCM). All measurements are performed in pulsed operation to limit self-heating, using a pulse width of 1000 ns with a 5 kHz repetition rate, corresponding to a duty cycle of 0.005.

6.4.1 Laser Measurements

6.4.1.1 Room Temperature Performance

This section covers how the threshold current density and emission wavelength of the lasers, operating at room temperature, vary with different cavity lengths ranging from 2 mm to 0.3 mm.

Power -Current Characteristics

For each cavity length, the optical power output at room temperature (the room is temperature controlled to 21±1°C), was measured as a function of drive current using the setup described in Chapter 3. Figure 6.3 presents a plot of the resulting P-I curve, illustrating how the laser's output power varies as the input current increases. This curve can be used to identify the threshold current, which is the minimum current required for lasing action to occur. From this, the threshold current density, which is the current per unit area needed for the laser to emit coherent light, can be determined. This is an essential factor in evaluating the laser performance. Near-field measurements were used to assess the current spreading using the method outlined in Chapter 3, to determine the effective area of the device and calculate the threshold current density. As shown in Figure 6.4, the threshold currents density is plotted as a function of cavity length.

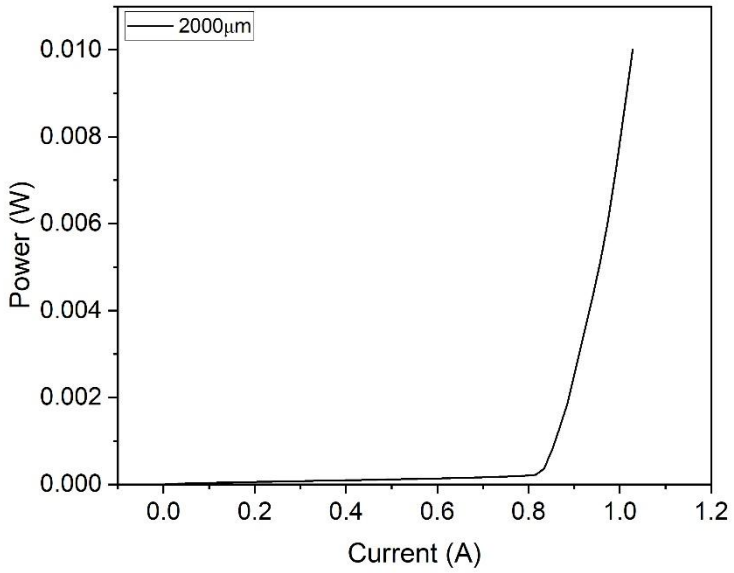

Figure 6.3. Power-current curve of a 2000 μm cavity length laser.

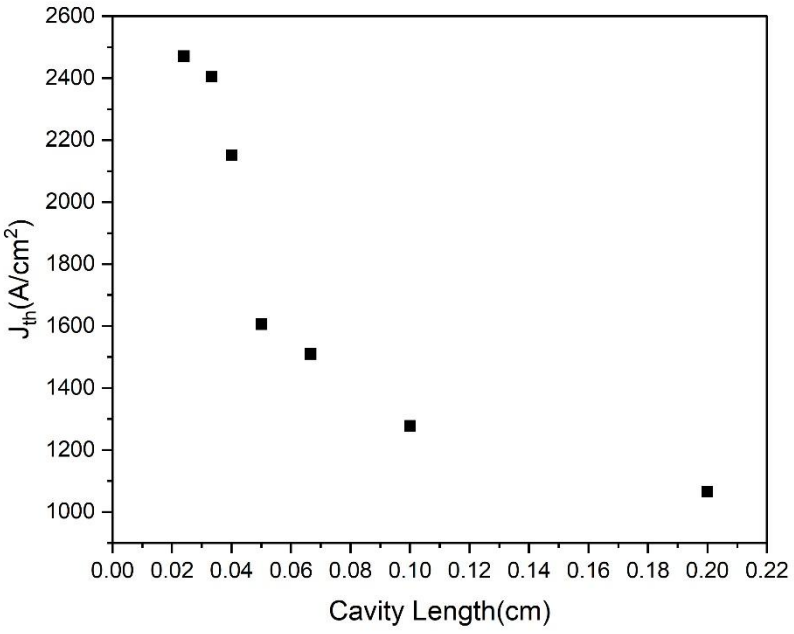

Figure 6.4. Threshold current density vs cavity length, for cavity lengths ranging from 2mm to 0.24mm.

Semi-logarithmic plot of threshold current density vs 1/cavity length

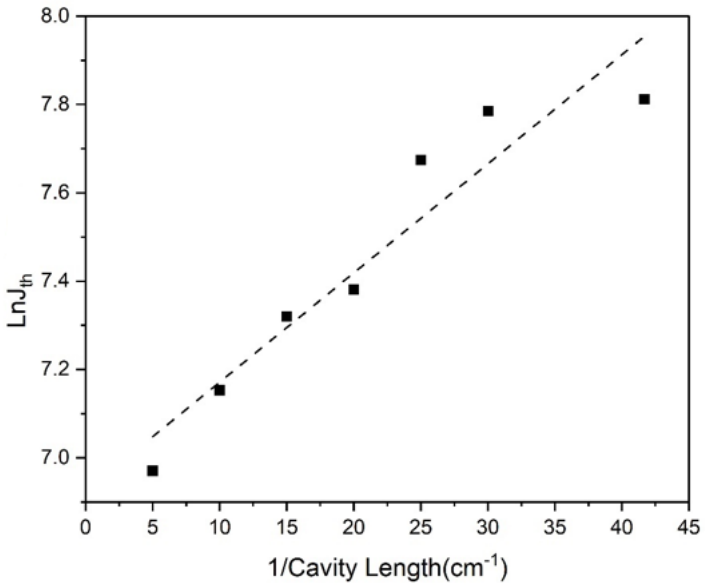

Figure 6.5. Threshold current density vs inverse cavity length, for cavity lengths ranging from 2mm to 0.24mm.

Figure 6.5 illustrates a plot of current density versus reciprocal cavity length, where a linear fit is applied. The slope of this line, expressed as $\frac{(lnR^{-1})}{NG_0}$, is used to derive the gain coefficient, as described in Chapter 2. By applying Equation (2.19) on Figure 6.5, the gain parameter NG_0 can be extracted.

The gain parameter of NG_0=56±9.9 cm-1, corresponding to 10.8±1.9 cm-1 per layer. Notably, this value is lower overall and slightly lower per layer than the gain coefficients determined for the 6QW sample of Chapter 4. The difference in gain between quantum dots QDs and quantum wells QWs is expected, as QWs typically exhibit a higher material gain due to their continuous energy bands and higher density of states, which promote more efficient carrier recombination. Quantum dots, with their discrete energy levels and lower density of states, generally show a reduced gain. This trend is also observed when comparing InAs/GaAs QDs with InGaAs/GaAs QWs, where QDs tend to have lower gain due to their reduced carrier interaction and potential defect-related issues. The reported gain parameter of 56 ± 9.9 cm^{-1} (10.8 ±

1.9 cm^{-1} per layer) in the current sample, however, is more typical of quantum wells than quantum dots. This suggests that while the structure may be based on QDs, its gain behaviour is closer to that of a quantum well, likely due to factors such as the specific material design or experimental setup that mimics the characteristics of a QW system. Thus, the gain in this QD sample appears to be more QW-like, reflecting a higher gain coefficient than typically expected for QDs.

Peak wavelength

The peak emission wavelength at currents 10% above the threshold current ($1.1I_{th}$) is measured as a function of temperature, using the spectral measurement methods outlined in Chapter 3. Figure 6.6.(a) illustrates the intensity as a function of wavelength in the region between 1570 nm and 1640 nm, correspond to varying cavity lengths from 0.3 mm to 3 mm. The shift in the peak positions as the cavity length changes suggests that the cavity is being tuned, affecting the resonant wavelengths. Longer cavity lengths generally lead to a larger shift in the resonant wavelengths.

Figure 6.6 (b) shows the relationship between cavity length and peak wavelength, showing a shift in the emission wavelength from 1560 nm to 1590 nm. This shift, which occurs without a transition to the excited state, is approximately 30 nm (highlighted in red). It illustrates that the peak wavelength changes by around 30 nm as the cavity length increases from 0.3 mm to 3 mm. The shift in wavelength is attributed the effects of state-filling within a relatively broad density of states due to fluctuations in size, shape or composition of the dots / dashes or wells, and highlights the potential of the material for use as a tuneable laser source. We also note that the self-assembled process naturally produces material with peak wavelengths slightly longer than the 1550 nm target wavelength.

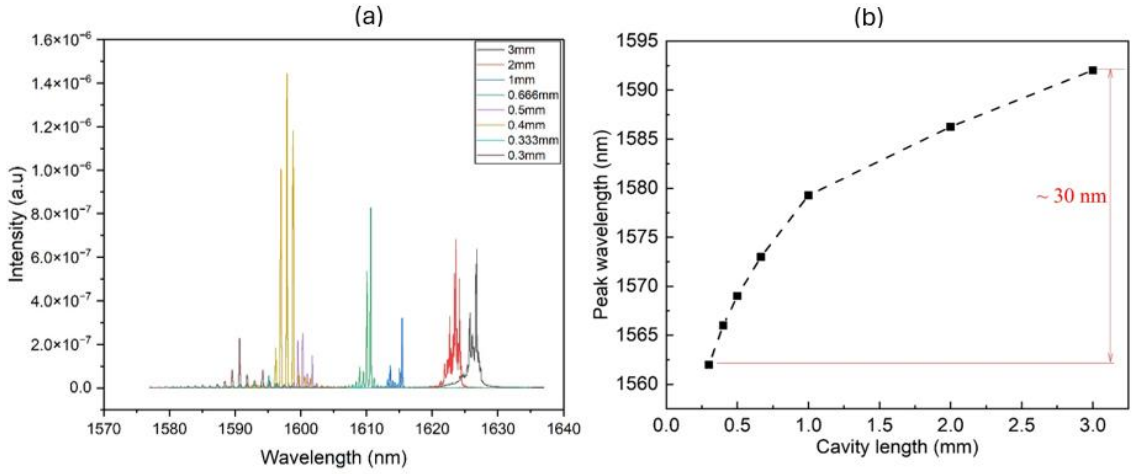

Figure 6.6. a). Emission spectra at I_{th} for laser devices with cavity length from 3000 µm to 300 µm. b). Wavelength vs. Cavity length at 21°C.

6.4.1.2 Temperature dependent measurement

This section covers how the threshold current density and wavelength of lasers changes with temperature, for cavity lengths ranging from 0.3 mm to 2 mm.

Temperature Dependence of Threshold Current

The rate of change of the threshold current density with temperature is an important indicator of the temperature stability, for temperature-insensitive laser performance. For this, light-current characteristics were measured at elevated temperatures between 300 and 380 K.

In general, as the temperature increases, the threshold current density typically increases due to the higher non-radiative recombination, and therefore reduced material gain for a given current density [6]. The response to temperature changes also depends on the cavity length. Lasers with shorter cavities generally exhibit higher threshold current densities because, they require a higher current density to achieve the higher gain per unit length, necessary to overcome the mirror loss [6,7]. The gain is required to compensate for the mirror losses, over a shorter roundtrip path length.

In this work, the threshold current density is plotted as a function of operating temperature for cavity lengths ranging from 2000 µm to 300 µm in Figure 6.7. The threshold current density is observed to increase monotonically with temperature for all cavity lengths. The threshold current density increases by a factor of 3.4 from 300 to 380 K for the longest 2000 µm cavity and by a factor of 3.8 for the shortest 300 µm cavity. Additionally, Figure 6.7 demonstrates that at 300 K, the threshold current density increases from ~1 $kAcm^{-2}$ to ~2.2 $kAcm^{-2}$ as the cavity length is reduced from 2000 µm to 300 µm. Moreover, a laser with a 0.3 mm cavity can function effectively at temperatures reaching up to 380 K. This indicates that the laser structure is suitable for operation over a wide temperature range.

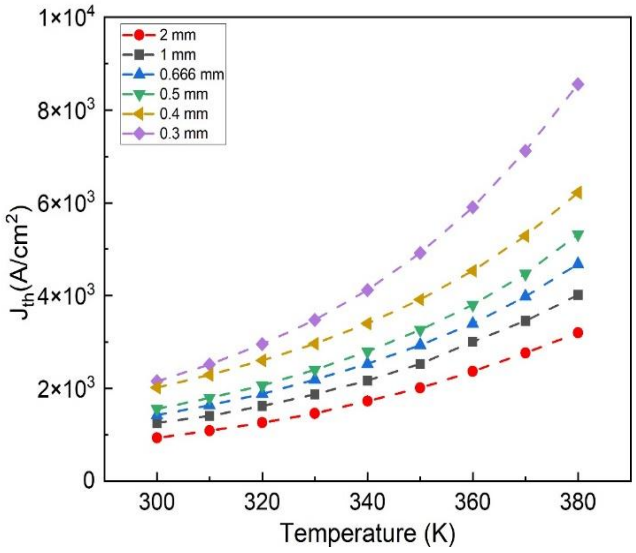

Figure 6.7: Threshold current density as a function of temperature between 300 K- 380 K, for different cavity lengths from 2000 µm to 300 µm.

Temperature Dependence of the Peak Wavelength

The peak wavelength as a function of temperature was measured over the range from 300 K to 380 K, and the wavelength's dependence on cavity length was found to be consistent at all measured temperatures. It was observed that there was no significant transition of the lasing wavelength from the ground state to the excited state. Even the shortest cavity maintained a steady increase in wavelength up to 380 K, with no visible shift to an excited state, as shown in Figure 6.8.

This lack of observable switching is an important aspect, as it can influence the performance and efficiency of the lasing process at the desired emission wavelength. Specifically, this indicates that a linear relationship between temperature and wavelength, with a temperature dependent wavelength increase of approximately 0.56 nm/K.

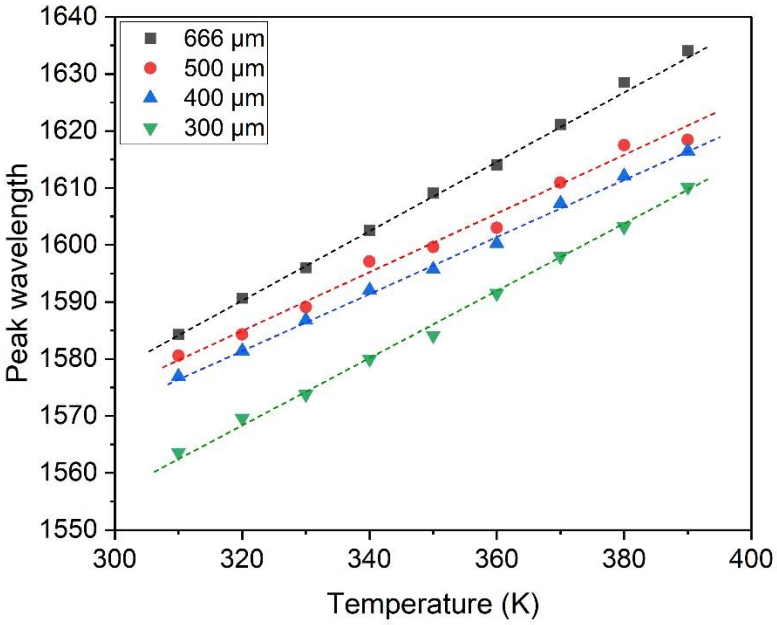

Figure 6.8: Peak wavelength as a function of temperature between 310 K- 380 K, for devices with a cavity length from 2000 µm to 300 µm operating at 1.1I_{th}.

6.4.2 Optical Gain and Loss Measurements

To better quantify the range of wavelengths that could be achievable with this material I also include measurements of the optical gain and loss, determined by analysing the amplified spontaneous emission spectra at different injection currents. By using the segmented contact technique, as outlined in Chapter 3, the optical gain-current characteristics and optical absorption at room temperature, were investigated. The segmented contact technique, which is a variable stripe length method, is the same technique used in the previous study [4] and before that on studies in other materials [8, 4].

Optical Gain

The net modal gain versus wavelength under currents varying from approximately 40 mA to 200 mA, at 21±1°C, is shown in Figure 6.9.

The internal optical loss, usually caused by free-carrier absorption or scattering within the waveguide, can be determined from the long-wavelength region, beyond the band edge, of the gain and absorption curves. The internal optical loss was determined to be approximately $\alpha_i \approx 5 \pm 3 cm^{-1}$. The loss of InAs QDs was previously seen to be much higher [4]. InGaAs and GaAs-based lasers typically have internal optical losses around 5 cm^{-1}, common for high-performance devices like edge-emitting lasers and VCSELs. In contrast, InAs quantum dot QD lasers generally have lower internal optical losses than traditional quantum well QW lasers. For InAs QDs on InP substrates, losses range from 3 to 10 cm^{-1}, depending on dot density, substrate quality, and device design. However, for InAs QDs grown on silicon Si substrates, optical losses can be significantly higher, reaching 15 to 20 cm^{-1} due to lattice mismatches and increased scattering at the interface [4].

In Figure 6.9 the lowest curve is the optical absorption when a 0V bias is applied. In this case, the material absorbs light, resulting in a negative gain. At lower injection currents (e.g. at 40 mA and 60 mA), the gain curves remain below zero, meaning the material only absorbs light and does not provide amplification. As the current is increased to around 100 mA and above, there is an onset of net optical gain. At high injection currents e.g., 160 mA to 200 mA, the gain curves reach positive values across a larger range of wavelengths, showing that the material achieves net optical gain (amplification). The peak gain is measured to be ~60 cm^{-1} (~12 cm^{-1} per layer) at the highest injection current. The arrow pointing towards higher currents illustrates that as the injection current increases, the net gain shifts upwards with the peak gain occurring near 1500-1550 nm. At higher injection currents, the device has a broader wavelength range over which it can provide positive gain. The rate of increase in peak gain with current is somewhat smaller at very high injection currents (e.g., 200 mA) but there is still an increase. Typically, quantum dot lasers show the gain-current curve appear to start levelling off at the highest currents, which is usually taken to indicate

that the material is reaching a saturation point where further increases in current will not significantly increase the gain. The gain saturation in quantum dots can occur when all the dot states become filled with carriers [6]. A broad gain bandwidth was observed at high injection current, with a positive optical gain over a 130 nm wavelength range for an injection current of 200 mA. In a simple Fabry-Perot laser the allowed longitudinal modes are close together and the lasing wavelength is determined by the wavelength of the peak of the gain curve. In a distributed feedback (DFB) laser the laser wavelength is determined by the grating period and so lasers can be created with any wavelength providing there is positive net gain. This suggests that a large number of, for example, DFB lasers could be fabricated from a single wafer with each laser wavelength selected from any point within this range of positive gain or alternatively a single laser could be fabricated where the laser wavelength is tuned over this range. Both of these options are useful for different applications.

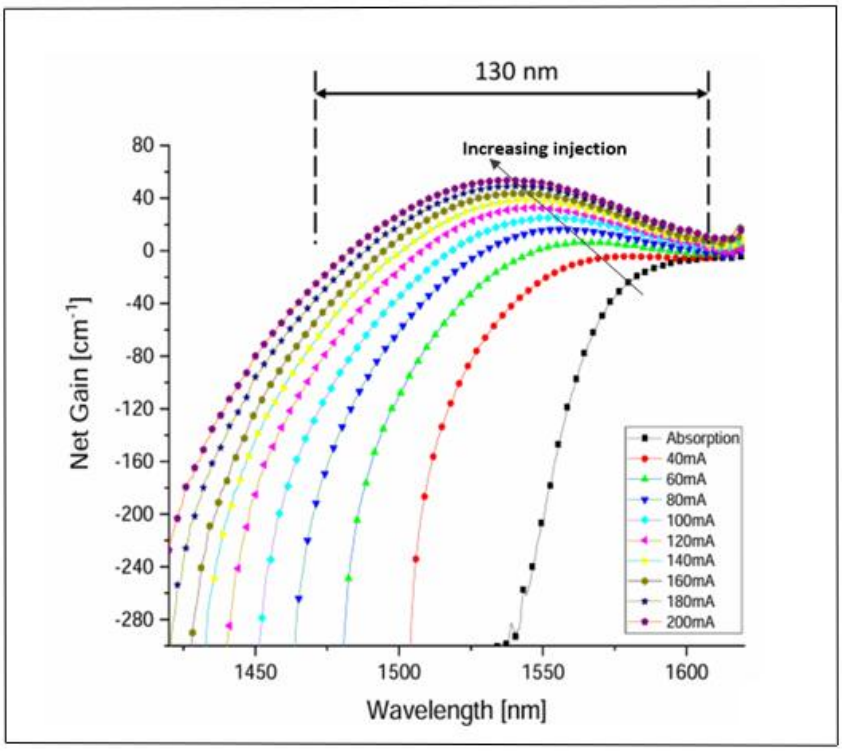

Figure 6.9: The net optical gain as a function of wavelength, from multi-section measurements, for different injection currents at 21±1°C. [Data provided by Dr. Zhongming Cao].

Figure 6.10 shows the peak net gain as a function of current density and compares the current density vs peak net gain relationship determined from laser devices data (black squares) with that measured using the segmented contact method (red squares). Clearly the data should essentially lie on the same curve for both sets of data. The graph shows the data is similar and is confirmation of the quality of the gain data. The rapid increase in gain with current density and the fact that it does not depart too much from a straight line suggests that gain saturation, which is normally seen with quantum dots, is not present here. This supports the idea that the material is actually formed from quantum dashes or modulated thickness QWs and not dots. In the next chapter I investigate material from further epitaxial growth runs where the growers have attempted to create dots rather than dashes or modulated QWs [9,10].

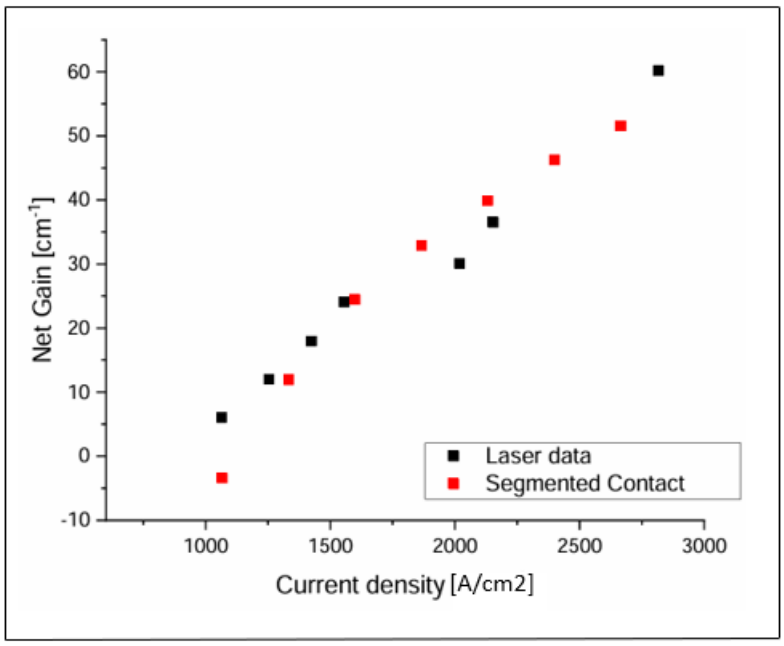

Figure 6.10: The peak net gain as a function of current density for laser and segmented contact method. [Data provided by Dr. Zhongming Cao].

6.5 Summary

This study presented quantum dot /dash / QW lasers grown on n-InP with emission wavelengths in the range of 1560 nm to 1600 nm at room temperature 21±1°C, for cavity lengths ranging from 300 µm to 3000 µm.

In this study, the threshold current density is observed to increase consistently with temperature across all cavity lengths. Between 300 and 380 K, the threshold current density rises by a factor of 3.4 for the longest cavity 2000 μm and by a factor of 3.8 for the shortest cavity 300 μm. At 300 K, the threshold current density increases from approximately 1 kA/cm² to 2.2 kA/cm² as the cavity length decreases from 2000 μm to 300 μm. Notably, a laser with a 300 μm cavity remains functional at temperatures up to 380 K, demonstrating that the laser structure is well-suited for operation over a wide temperature range.

The peak lasing wavelength shows no observable switch from ground state to excited state at temperatures up to 380 K. Even for cavity lengths as short as 300 μm, the laser maintained stable, ground-state lasing at temperatures up to 380 K.

Typically, for QD lasers, the switching to excited state from ground state laser emission occurs when the ground state gain cannot increase any further (saturates), so that the threshold gain requirement can only be met by transitions related to the excited state. Here it appears as though the ground state saturation gain is very high, (higher than the gain requirement for the shortest cavity), which means ground state emission is observed, even for the shortest cavity. This suggest that the material is actually formed of quantum dashes or modulated QWs with significant size or composition broadening where the energy separation of the ground state and excited state transitions is smaller than the broadening, causing them to merge together, and provide more gain [3,11].

From multi-section measurements at room temperature 21±1°C, with different injection currents, the internal optical loss was determined to be approximately $\alpha_i \approx 5 \pm 3$ cm^{-1}. This may be a result of the $In_{0.45}Ga_{0.55}As$ capping layer which was employed to try and reduce the optical loss. The gain peaks are measured to be ~60 cm^{-1} (~12 cm^{-1} per layer) at the highest injection current. Gain measurements also indicate a broad optical gain bandwidth of approximately 130 nm. These characteristics make the presented structures promising optical sources for integration into silicon-photonic platforms. However, we conclude that the laser performance is still constrained by the high current density needed to attain substantial gain. In the next chapter I explore the use of material, where changes in the growth are intended to create quantum dot material to see if this helps with the high current density.

In this study, the behavior of quantum wells QWs was explored, focusing on their wavelength characteristics and formation processes. For the quantum well in a deep quantum well DWELL structure, the expected wavelength is determined by the composition of the materials (e.g., InGaAs) and the thickness of the well. Typically, the wavelength of the QW without QDs falls within the range of 1.3 μm to 1.6 μm, based on the composition and material system, including InAlGaAs barriers. In the case where In from the QDs uniformly disperses into the QW, the composition of InGaAs in the well would increase, shifting the wavelength to a longer value, depending on the final indium concentration. Furthermore, atomic force microscopy (AFM) images showing no elongation suggest that QD formation likely occurred during the capping process, likely due to strain relaxation under those conditions. The absence of state switching, particularly in short cavities and high-temperature environments, further suggests that the structure exhibits quantum well behavior. Unlike QDs, which show more sensitivity to temperature and cavity length due to discrete energy states, quantum wells typically display continuous states, consistent with the observed lack of state switching. This behaviour aligns with that seen in GaAs-based QD lasers, where similar conditions result in QW-like behaviour.

References

1. Xiao, Z., Liu, W., Xu, S., Zhou, J., Ren, Z., & Lee, C. Recent Progress in Silicon-Based Photonic Integrated Circuits and Emerging Applications. *Advanced Optical Materials* vol. 11(2). doi.org/10.1002/adom.202301028 (2023).

2. Norman, J.C., Jung, D., Zhang, Z., Wan, Y., Liu, S., Shang, C., Herrick, R.W., Chow, W.W., Gossard, A.C. & Bowers, J.E. A review of high-performance quantum dot lasers on silicon. *IEEE Journal of Quantum Electronics.* 55(2),1-11. doi.org/10.1109/JQE.2019.2901508. (2019).

3. Grillot, F., Duan, J., Dong, B. & Huang, H. Semiconductor quantum dot lasers: Genesis, prospects, and challenges. in *Quantum Photonics* 191-266 (Elsevier, 2024). doi:10.1016/B978-0-323-98378-5.00008-8.

4. Li, Z., Shutts, S., Xue, Y., Luo, W., Lau, K. M., & Smowton, P. M. Optical gain and absorption of 1.55 μ m InAs quantum dash lasers on silicon substrate. *Appl Phys Lett* 118 (13), (2021).

5. Zhou, D., Piron, R., Dontabactouny, M., Dehaese, O., Grillot, F., Batte, T., Tavernier, K., Even, J. & Loualiche, S. Low threshold current density of InAs quantum dash laser on InP (100) through optimizing double cap technique. *Appl Phys Lett* 94(8), (2009).

6. Blood, P. *Quantum Confined Laser Devices: Optical Gain and Recombination in Semiconductors*. vol. 23 (OUP Oxford, 2015).

7. Shashkin, I.S., Vinokurov, D.A., Lyutetskiy, A.V., Nikolaev, D.N., Pikhtin, N.A., Rudova, N.A., Sokolova, Z.N., Slipchenko, S.O., Stankevich, A.L., Shamakhov, V.V. & Veselov, D.A. Temperature dependence of the threshold current density in semiconductor lasers (λ = 1050-1070 nm). *Semiconductors* 46, 1211-1215 (2012).

8. Blood, P., Lewis, G.M., Smowton, P.M., Summers, H., Thomson, J. & Lutti, J. Characterization of Semiconductor Laser Gain Media by the Segmented Contact Method. in *IEEE Journal on Selected Topics in Quantum Electronics* vol. 9(5), 1275–1282 (2003).

9. Reithmaier, J. P., Eisenstein, G. & Forchel, A. InAs/InP quantum-dash lasers and amplifiers. *Proceedings of the IEEE* 95(9), 1779-1790 (2007).

10. Paranthoen, C., Bertru, N., Dehaese, O., Le Corre, A., Loualiche, S., Lambert, B. & Patriarche, G. Height dispersion control of InAs/InP quantum dots emitting at 1.55 μm. *Applied Physics Letters,* 78(12),1751-1753. (2001).

11. Chuang, S. L. *Physics of Photonic Devices*. John Wiley & Sons. 27-53. (2012).

Chapter 7: Characterisation of InAs/InP Lasers and Gain Material: Growth 2

7.1 Introduction

In Chapter 1, we highlighted the challenges and progress achieved in the field of photonic integrated circuits (PICs). A key component in PICs is the semiconductor laser, primarily based on quantum well (QW) technology. While QW lasers are relatively straightforward to grow and fabricate, they possess several intrinsic shortcomings that hinder their effectiveness as ideal light sources for PICs. For instance, QW lasers are sensitive to thermal effects, so that temperature variations can significantly alter their emission wavelength and intensity [1,2]. To address these issues, quantum dot (QD) gain materials have emerged as a potentially superior alternative for PIC applications [3,4]. QD lasers offer several advantages due to their atom-like nature, (that due to the quantum confinement along all three dimensions that results in 0-dimensional density of states, which is a delta function in the ideal case) which includes low threshold current density and enhanced thermal stability. These characteristics make QDs highly desirable for on-chip laser devices. Compared to QWs, QDs are individual nanoparticles with a larger energy sublevel separation, which limits carrier escape and reduces in-plane diffusion. Additionally, because of this localisation in the dots and reduced in-plane diffusion, the carriers in a QD active material interact less with threading dislocations (TDs). Consequently, QD lasers are less susceptible to TDs when directly grown on Silicon, and this tolerance to defects when grown on Silicon is a very significant motivator of the use of QDs rather than their QW counterparts [5–7]. The formation of InAs QDs via self-organized growth (the formation of self-assembled QDs depends on strain or lattice mismatch with the underlying layer) has attracted significant interest in both fundamental research and practical applications based on GaAs O-band and on InP C-band. However, the mechanisms behind the self-organized quantum dot QD growth process of InAs on InP substrates are still not well understood [8]. For example, how to control and grow symmetric QDs with a narrow size distribution. Therefore, the performance of InAs/InP QD lasers still lingers behind that of lasers based on GaAs substrates.

Although the InAs/InP and InAs/GaAs systems use the same material for the quantum dots, they differ significantly due to lattice mismatch: 3% for InAs/InP compared to 7% for InAs/GaAs. In the case of InAs/GaAs-based QDs, the 7% lattice mismatch promotes the formation of symmetrically shaped dots. In contrast, the 3% lattice mismatch between InAs and InP results in less strain for dot formation, which, depending on the specific growth conditions, can lead to QDs with smaller height-to-diameter aspect ratios or elongated dots, referred to as quantum dashes (QDH). As mentioned in Chapter 2 these possess properties that are a hybrid of QWs and QDs[9–11]. Therefore, the primary challenge in dot formation on InP substrates is managing the reduced lattice mismatch.

To shift from the growth of dashes to QDs is challenging but achievable by careful optimisation of growth conditions. Consequently, significant efforts have been directed toward optimizing growth, starting from substrate preparation and choosing the orientation of the substrate [12]. Previous research indicates that the growth temperature significantly influences the formation of InAs nanostructures and plays a crucial role in determining the shape and size of the quantum structures. Dashes are often formed when the temperature is higher than the optimum for QD formation. Thus, the slight lowering of growth temperature can encourage the formation of QDs rather than elongated dashes. Reduced temperature reduces surface diffusion during growth, which is a key factor in forming dashes.

In this chapter, the key properties of InAs self-assembled QD semiconductor materials on native InP substrates are examined to assess their suitability for growth on Si, as a future step. Therefore, the primary focus is on investigating the active material grown on InP. Another objective of this chapter is to investigate the effects of InGaAs and InGaAlAs capping layers on the formation of InAs QDs, and to understand how these capping layers affect their properties. This is achieved by measuring the characteristics of lasers fabricated from these materials; to determine properties such as gain parameter, internal differential efficiency, and internal optical losses. These parameters are typically expected to be independent of the device geometry. We will assess their performance to analyze and highlight their similarities and differences. The measurements in this chapter were conducted either at room temperature or as a function of temperature, using broad-area edge-emitting devices with an oxide stripe to define the width of the electrically pumped region.

7.2 Epitaxial Structure

The epitaxial structures used in this study are represented in Figure 7.1. They were grown at Cardiff University by Dr Qiang Li. using a metal-organic chemical vapor deposition MOCVD growth system to achieve InAs QDs on n-InP (001) substrates. In this case, the crystal orientation of InP substrates is in the (001) plane, which is the most commonly used due to its ideal surface properties for epitaxial growth. This orientation has low surface energy, making it well-suited for uniform layer deposition. Additionally, this substrate orientation conforms to industrial processes for mass production, particularly for high-quality layers used in electronic and optoelectronic devices[12]. Dot-in-well (DWELL) structures were used for the active region, which consisted of self-assembled InAs QDs embedded in InGaAs/InAlGaAs strained QWs for carrier confinement, similar to previous studies [13-15]. InAs QDs were grown, via the Stranski-Krastanov process, onto a 2nm $In_{0.35}Ga_{0.65}As$ pre-layer which aims to improve the dot formation. The difference between the pre-layers in the three structures, A, B and C, described here is that they are formed from $In_{0.35}Ga_{0.65}As$, whereas the structure from Chapter 6 was formed of $In_{0.45}Ga_{0.55}As$. The capping layers are also different to those used in Chapter 6. The combined differences were meant to maintain a short QD emission wavelength, while increasing the amount of material in the capping layer and the strain relative to the dot material. A higher Indium content reduces the tensile strain with the substrate and underlying layers typically resulting in fewer defects and improving overall material quality for planar growth but being less of a stimulus for dot formation. In contrast, a lower Indium content increases the contrast to the substrate and dot material and may help in the formation of dots but may increase defect density.

The QDs in structures A and B were capped with a 4 nm $In_{0.35}Ga_{0.65}As$ layer, while the QDs in structure C were capped with a 4 nm $In_{0.45}Al_{0.275}Ga_{0.275}As$. The key differences between the structures arise from their capping layers and the resulting effects. This is more material than in Chapter 6, where a 0.7nm capping layer was used. Structures A and B, capped with 4 nm $In_{0.35}Ga_{0.65}As$ have a higher barrier bandgap meaning the dot states can also have a higher energy and result in a shorter emission wavelength[16]. In contrast, Structure C, capped with 4 nm $In_{0.45}Al_{0.275}Ga_{0.275}As$, has the same indium

content as Chapter 6 but the Al content is increased to try and maintain the larger bandgap and shorter emission wavelength [17].

The DWELL layers were separated by 40nm $In_{0.52}Al_{0.26}Ga_{0.22}As$ barrier layers. This process was repeated for the number of QD layers, with structures A containing three DWELL layers and structures B containing five DWELL layers, while structure C contained three DWELL layers. The active region was surrounded by 240 nm un-doped $In_{0.52}Al_{0.26}Ga_{0.22}As$ layers which formed the separate confinement heterostructure (SCH), and the p-InP and n-InP were used as the upper- and lower-cladding layers which formed the rest of the waveguide. P-type $In_{0.53}Ga_{0.47}As$ was deposited as the top cap layer to facilitate ohmic contact formation. The quantum dots and the capping layers of these structures were grown at 680°C. Samples were processed into a set of 2000µm to 300µm long Fabry-Perot (FP) laser devices, with a 50-um wide oxide-isolated stripe laser and cleaved uncoated facets.

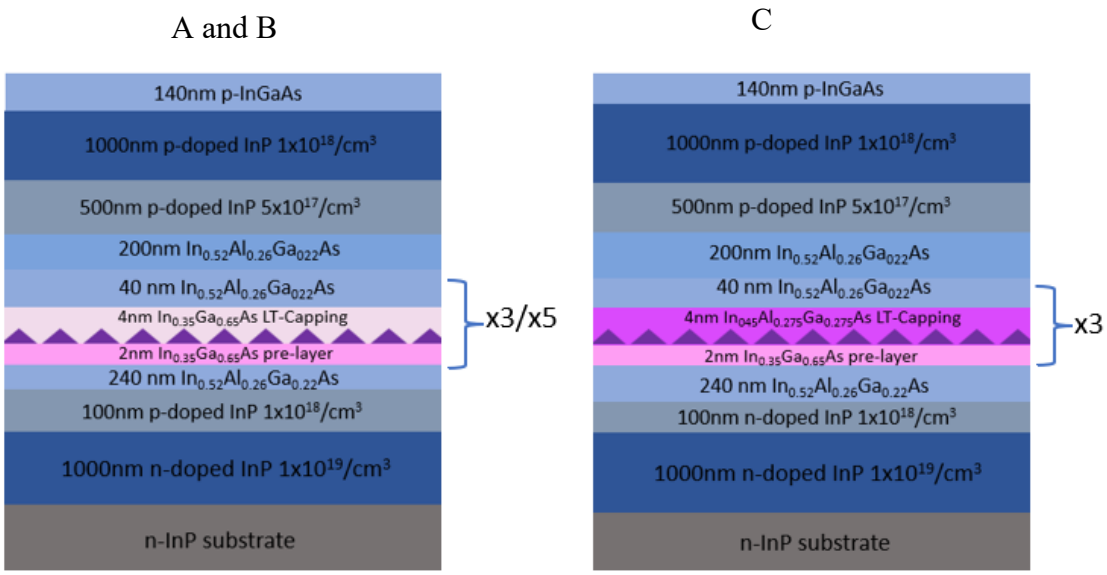

Figure 7.1: Schematic diagram showing wafer A containing three DWELL layers, B containing five DWELL layers both with capped with $In_{0.35}Ga_{0.65}As$ layer, while structure C contained three DWELL layers with capped with $In_{0.45}Al_{0.275}Ga_{0.275}As$.

7.3 Characterisation methods of III-V semiconductors (Dots, Dashes or Wells)

Photoluminescence (PL) and transmission electron microscopy (TEM) [18] are used before device fabrication to evaluate the material quality grown by MOCVD. Photoluminescence data is reported later in the chapter.

TEM is used here to observe the structure formed by the growth, and to give some indication of whether QDs, quantum dashes QDH or QWs were grown. The TEM is performed in both "bright field" and "dark field" mode to try and produce the best resolution and identify the small features.

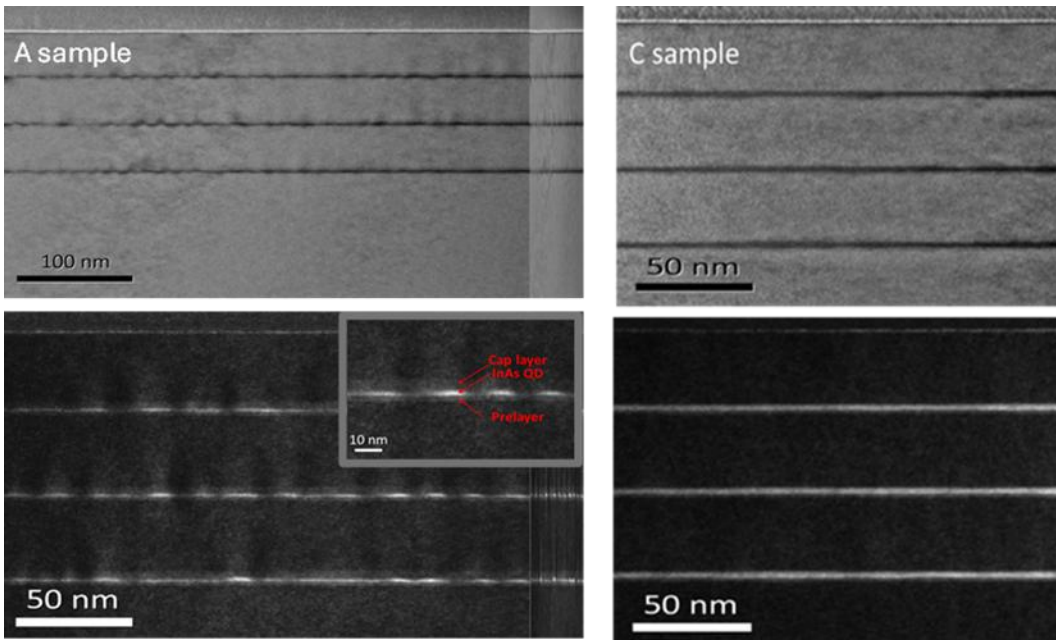

Figure 7. 2: TEM images showing the bright field (top) and dark field (bottom) of the active layer of structure A (left). A and B are expected to have similar nanostructure types as the QD capping material was the same, and the structure C (right). Images were supplied by Dr Qiang Li.

TEM was only carried out for samples A and C. The TEM images in Figure 7.2 show the 3 layers of material in the active region of the device. The presence of dots is not always very easy to see in TEM images, but the dark field image of structure A gives better resolution and clearly indicates that either dot or dash structures are present within the sample. The high magnification image in the inset shows regularly spaced features that are of order 10nm long with a similar size gap between the features. They

are substantially thinner in the vertical direction than the horizontal direction, as is commonly seen for both dots and dashes. On the right, the TEM image shows structure C, which does not exhibit discrete features in either the bright or dark field TEM images and seems to be a more well-like structure, albeit with a well width or composition that may vary considerably.

Since Sample A exhibits a dot or dash like structure, we assume that sample B is also likely to have such a structure. However, further measurements will help us determine this as well as have a better idea of whether these features are dashes or dots. Sample C, similar to the samples in Chapter 6, appears to be well like in nature and this gives us the opportunity to assess how the performance is different for dots / dashes and wells.

Two different sets of broad-area FP lasers, at a 90-degree angle to each other are fabricated. This means there are two orientations - one with the cavity aligned along the $[1\bar{1}0]$ direction, and the other with the cavity oriented along the [110] direction. According to the literature, the optical gain of the lasers fabricated in the two directions will differ if quantum dashes have been grown, with a higher gain for laser stripes oriented along the [110] direction. This is because dashes preferentially grow with longer dimensions along the $[1\bar{1}0]$ direction, as reported in [19,20]. This happens because of the different behaviours of the step edges on the InAs (001) surface. Step edges in the $[1\bar{1}0]$ direction have indium atoms, making them less reactive, while step edges in the [110] direction have arsenic atoms, which makes them more reactive to indium. As a result, the nanostructures grow faster along the $[1\bar{1}0]$ direction, leading to the formation of long quantum dashes, as shown in Figure 7.3: **The image illustrates the directional growth of dashes along the [110] crystallographic direction, showing their elongation in this direction as compared to their growth along the [110] direction. This behaviour is discussed in Chapter 2, Section 2.19.**

.b .

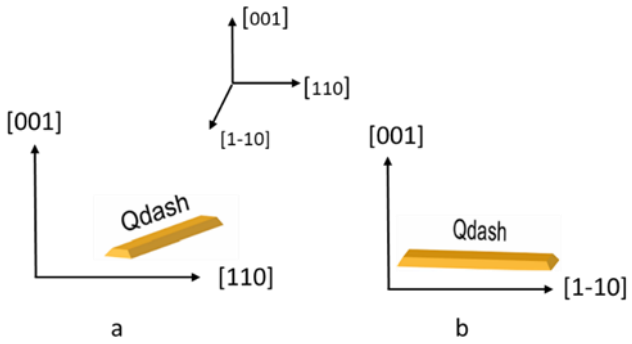

Figure 7.3: The image illustrates the directional growth of dashes along the [1$\bar{1}$0] crystallographic direction, showing their elongation in this direction as compared to their growth along the [110] direction. This behaviour is discussed in Chapter 2, Section 2.19.

To determine the direction depicted in the figure involving Qdash structures, it is important to consider the physical and structural characteristics of the Qdashes. These elongated nanostructures exhibit anisotropic optical properties, with emission and polarization typically aligned along their elongation axis. This axis, therefore, serves as a natural reference for defining directionality. Furthermore, the growth conditions and crystallographic orientation of the underlying substrate can influence the alignment of the Qdashes, often resulting in preferred directions such as [1$\bar{1}$0]. Accordingly, in the presented figure, the direction is defined by the elongation axis of the Qdash, which provides a basis for interpreting the emission characteristics, polarization behavior, and carrier transport, as discussed in Chapter 2, Section 2.19.

On the contrary, for QDs and QWs, it is expected that the gain and threshold current should be the same for lasers fabricated in both directions. In total six samples were fabricated, resulting in: A, B, and C orientated along the [110] direction, and A`, B`, and C` orientated along the [1$\bar{1}$0] direction. In more detail, we have six structures: structure A consists of three QD/QDH layers, structure B consists of five QD/QDH layers, and structure C consists of three QW-like layers. All these structures have the cavity aligned along the [1$\bar{1}$0] direction (the cavity oriented parallel (∥) to the QD/QDH direction). Structure A` consists of three QD/QDH layers, structure B`

consists of five QD/QDH layers, and structure C` consists of three QW like layers. All of these structures have the cavity aligned along the [110] direction, (with the cavity oriented perpendicular (⊥) to the QD/QDH direction) as shown in Figure 7. 3 .

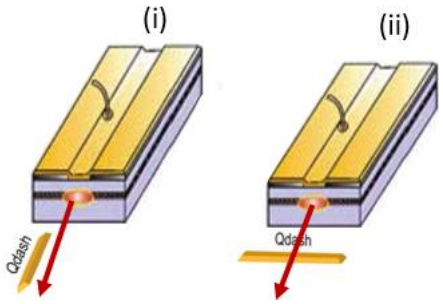

Figure 7. 3: Shows the orientation of the laser cavity. (i) presents the cavity aligned along the [1$\bar{1}$0] direction (parallel to the dot/dash direction), while (ii) illustrates the lasers with the cavity oriented along the [110] direction (perpendicular to the dot/dash direction).

7.4 Device Fabrication

The laser devices studied were fabricated in Cardiff by Dr. Zhongming Cao. The broad-area laser device was used to determine the basic electrical and optical properties of the grown material. The device was fabricated using standard processes such as photolithography, etching, and metal deposition. The fabrication steps are detailed in Chapter 3 in the device fabrication section.

The fabricated devices were then cleaved into a range of cavity lengths from 2000 to 300 µm, with uncoated and parallel facets reflecting approximately 28% of the light at the lasing wavelength. The cleaved chips were mounted and wire-bonded onto TO-8 headers. The samples were mounted onto copper heat sinks using silver-loaded epoxy and were then gold-wire-bonded to prepare them for measurement

7.5 Results and discussion

7.5.1 Optical Power-Current Characteristics

The properties of the three different laser diode structures, A, B, and C, each having FP laser devices fabricated with two orientations, 90 degrees to each other, are

investigated. To examine the impact of these structures on the threshold behavior of lasers on InP substrates, light-current measurements were conducted as a function of cavity length. Optical power was measured as a function of current and voltage.

A pulsed current source was employed, with a pulse duration of 1 µs and a repetition frequency of 5 kHz (resulting in a duty cycle of 0.005% to prevent self-heating effects). The measured P-I characteristics at 21±1°C are displayed in in Figure 7.5. From these plots, we extract and analyze the threshold current as a function of cavity length. The lasers have varying cavity lengths ranging from 2000 µm to 300 µm, with uncoated facets, and were intended to emit light with wavelengths around 1550 nm. It is clear from Figure 7.5 that the optimum length in terms of threshold current is 400 µm and threshold current increases for longer devices because of the increased amount of material being pumped. For the shortest devices, the threshold current is also higher than for long devices, which occurs because the mirror loss per unit length increases with reduce cavity dimensions and the gain per unit length available increases very slowly with current. This is also known as gain saturation [21] and is often the case for QD lasers. A typical I-V curve and the measured 0.75 V turn-on voltage is shown in Figure 7.6.

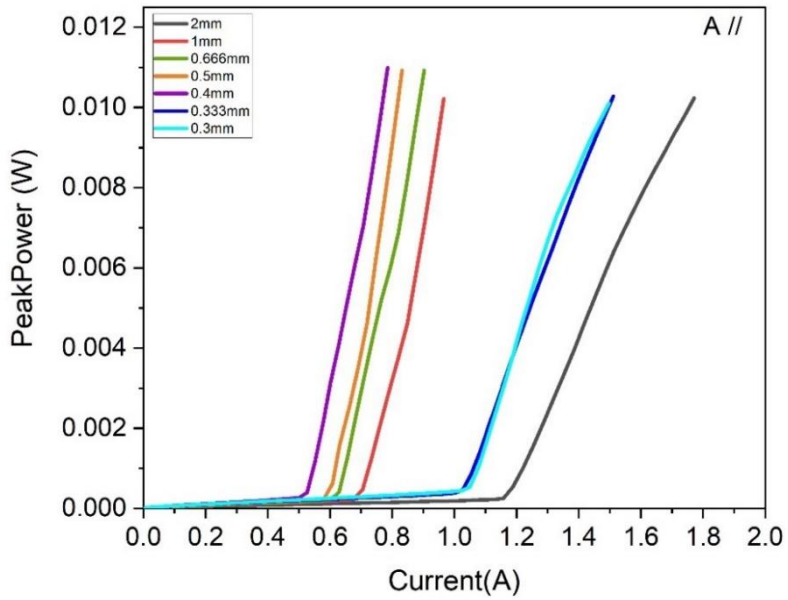

Figure 7.5: P-I characteristics for a typical A structure at room temperature (21±1°C). Any external differential efficiencies determined from the plot reflect the lower limit since not all of the emitted light is detected in the experiment.

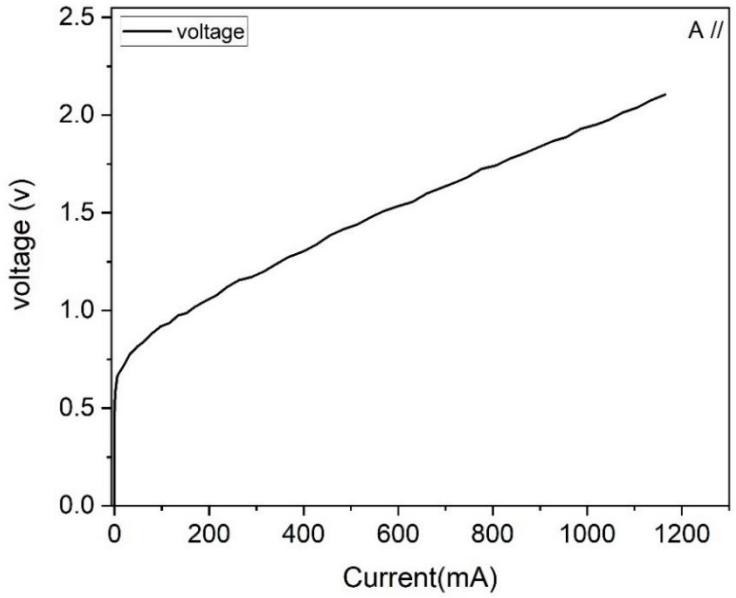

Figure 7.6: I-V Characteristics for a typical A structure at room temperature (21±1°C).

7.5.2 Threshold Current Dependence on Cavity Length

Figure 7.7 presents a comparison of threshold current from different cavity lengths from 2mm to 0.3mm at room temperature 21±1°C for different structure devices: A, B, C, A`, B` and C.` It is observed that the threshold current rises as the cavity length increases for all samples. This can be attributed to the larger pumping volume associated with longer cavity lengths. It should be noted that the threshold current is very high for some devices. In this case, simply comparing their threshold currents wouldn't be fair, as a larger diode inherently demands more current. Therefore, as explained in chapter 3 and as done in previous Chapters, the current density is calculated as a parameter that is more representative of the material because it is less dependent on the dimensions of the device.

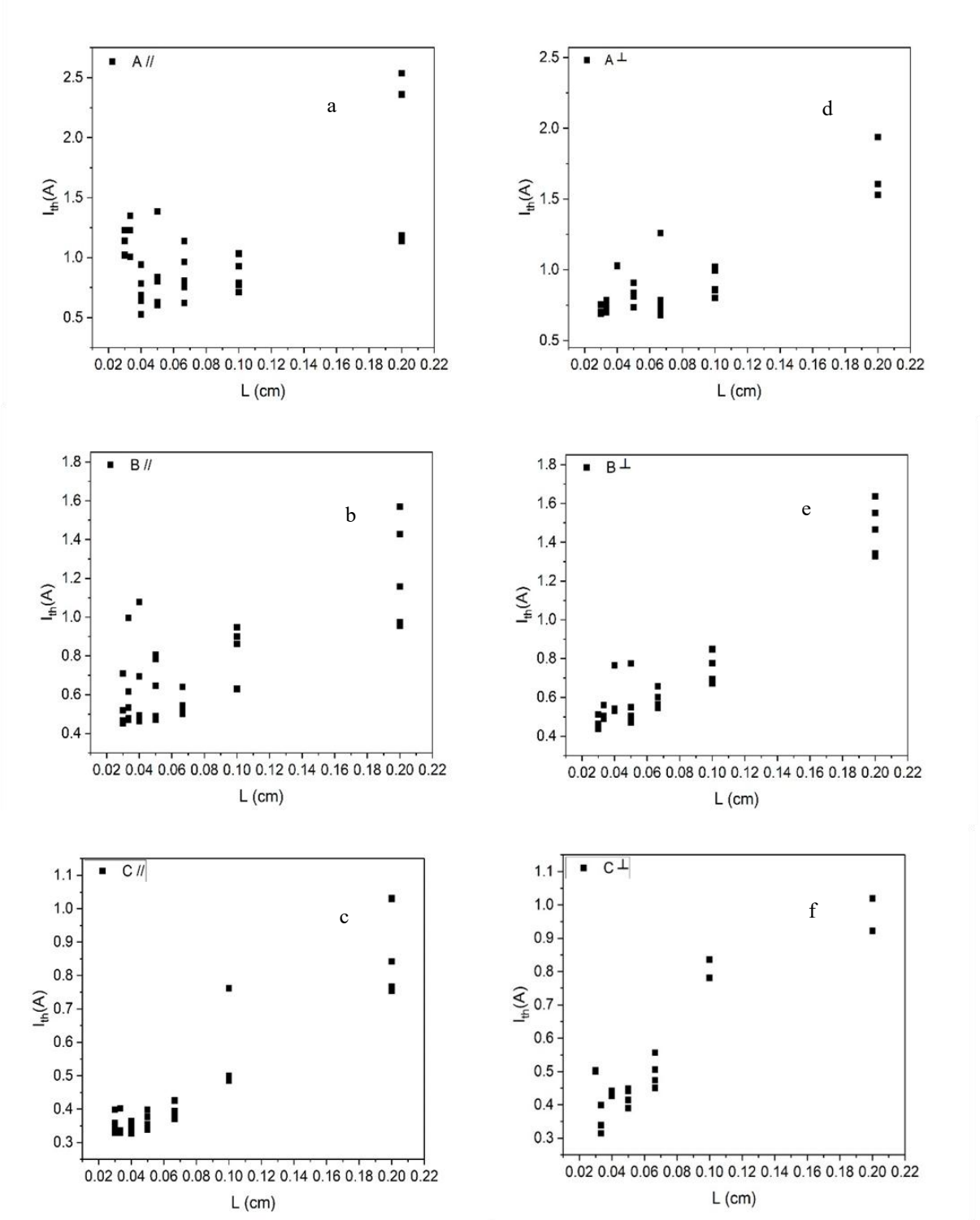

Figure 7. 7: The threshold current of different cavity length a) the three layer QDH/QD (b) the five layer QDH/QD (c) the three layer QW structure, all with the cavity aligned to the[1$\bar{1}$0] direction, and (d) the three layer QDH/QD (e) the five layer QDH/QD (f) the three layer QW, with the cavity aligned to the [110]direction.

7.5.3 Threshold current density vs. cavity length

The current density J_{th} was calculated by determining the current spreading using Equation (3.1) and near-field measurements, as mentioned in Chapter 3 [22].

After calculating the current density, there are still some devices that have very high current density values, which are large compared to other devices with the same cavity length. While devices can have a higher threshold current density due to imperfections in the cleaved facet, which act as mirrors, there are no reasons why the current density would be lowered by fabrication defects. As a result, devices with excessively high threshold current densities are excluded from further analysis, as shown by the red circles in Figure 7.8. Figure 7.9 demonstrates that threshold current density depends on the cavity length, and it is anticipated to be inversely proportional to it. A shorter cavity length results in a higher threshold current density due to increased mirror losses.

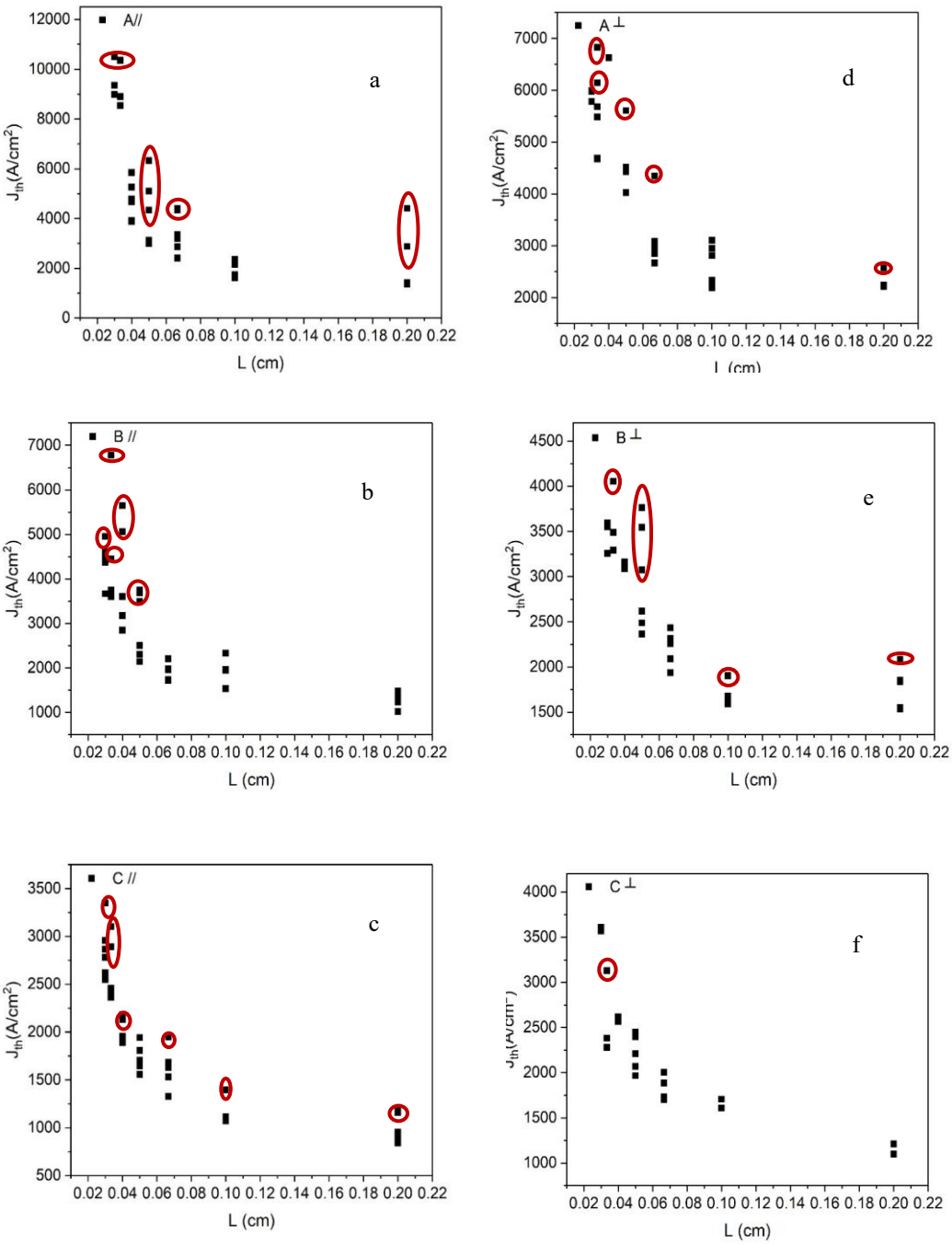

Figure 7. 8: Threshold current density as a function of L_c for different structures a) the three layer QDH/QD (b) the five layer QDH/QD (c) the three layer QW structure, all with the cavity aligned to the [1$\bar{1}$0] direction, and (d) the three layer QDH/QD (e) the five layer QDH/QD (f) the three layer QW, with the cavity aligned to the [110] direction.

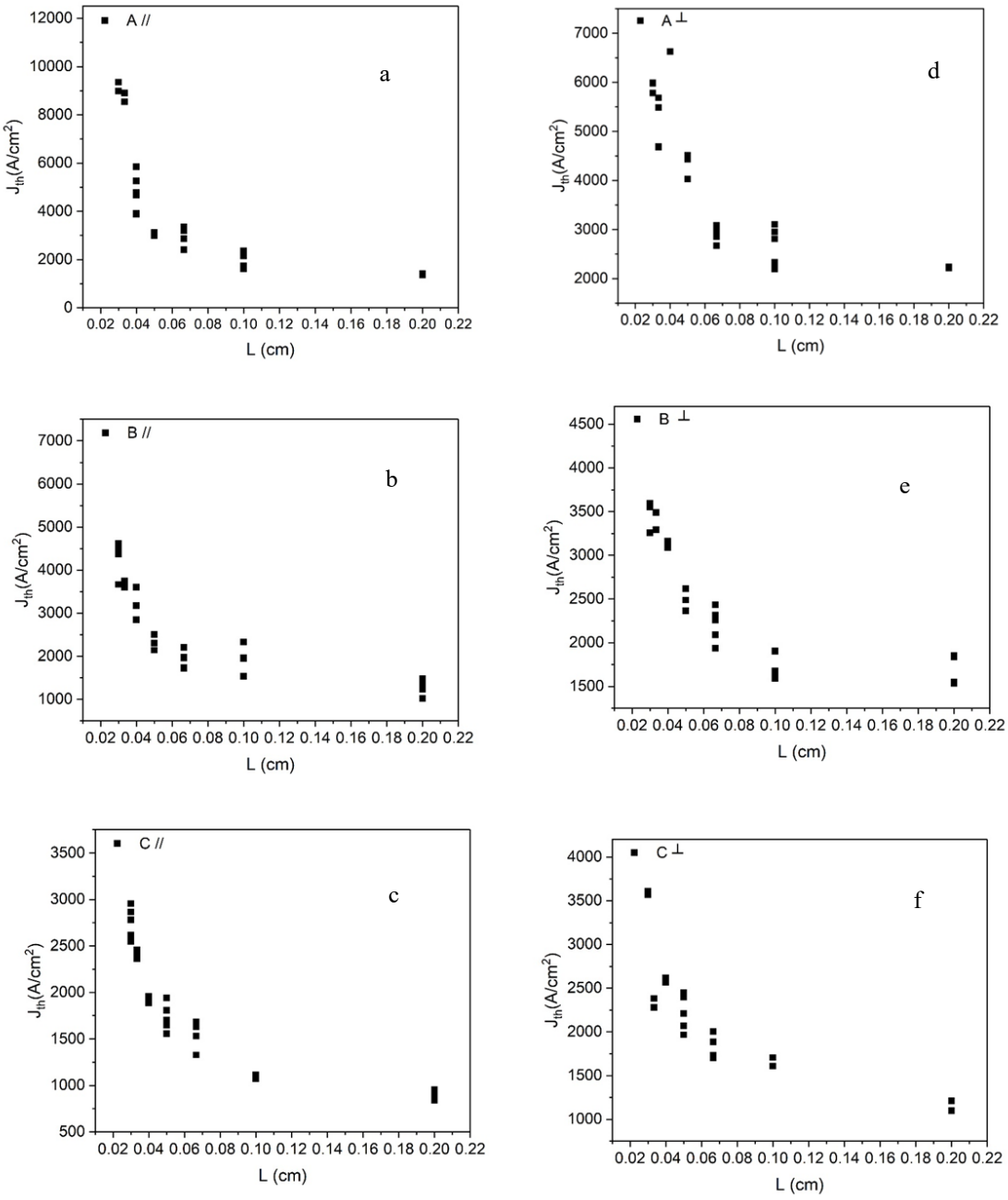

Figure 7.9: Threshold current density for different L_c ,excluding devices with very high threshold current densities-a) the three layer QDH/QD (b) the five layer QDH/QD (c) the three layer QW structure, all with the cavity aligned to the [1$\bar{1}$0] direction, and (d) the three layer QDH/QD (e) the five layer QDH/QD (f) the three layer QW, with the cavity aligned to the [110] direction.

7.5.4 Gain-Current density relation

In laser materials, the relationship between the peak gain and current density is expressed in Equation (2.18) from Chapter 2.

From this equation, we can plot the experimentally determined threshold current density against the inverse of cavity length to obtain the gain coefficient parameter G_0, as shown in Figure 7.10. The gain coefficient can be used to compare the quality of different laser-active materials, such as whether the optical gain differs when the cavity is aligned along the $[1\bar{1}0]$ direction (parallel to the dot/dash direction) and when the cavity is oriented along the [110] direction (perpendicular to the dot/dash direction), and how the these samples compare to the QW-like samples.

7.5.5 Semi-logarithmic plot of threshold current density vs 1/cavity length

By fitting Equation (2.19) to a semi-logarithmic plot of the experimental threshold current density and reciprocal cavity length, we can determine the gain parameter G_0 [22].

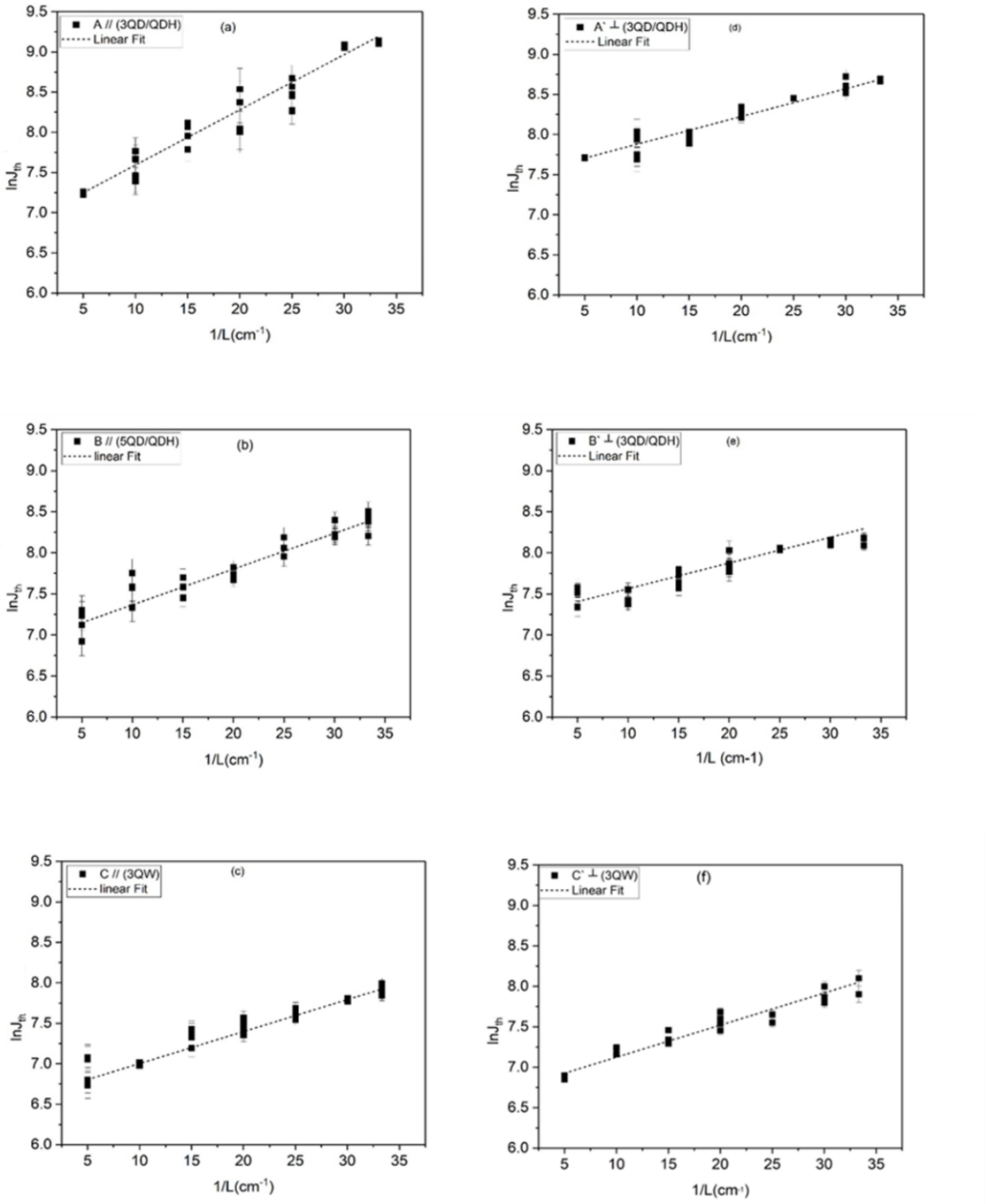

Figure 7.10 : Threshold current density versus reciprocal cavity length L_c for different structures, a) the three layer QDH/QD (b) the five layer QDH/QD (c) the three layer QW structure, all with the cavity aligned to the [1$\bar{1}$0] direction, and (d) the three layer QDH/QD (e) the five layer QDH/QD (f) the three layer QW, with the cavity aligned to the [110] direction.

Figure 7.10 displays a graph of current density plotted against the inverse of cavity length. A linear line with a gradient given by $\frac{(lnR^{-1})}{NG_0}$ is fitted to the plot, which is then used to determine the gain coefficients shown in Table 7.1. It is a fitting parameter that can describe the gain-current density curve experimentally, and it is an intrinsic property of the gain medium that indicates its ability to amplify light through stimulated emission, which occurs when a sufficient population inversion is achieved.

Table 7.1. Values of the Gain parameter, G_0, for different structures with the laser cavity oriented along the [110] direction, and the laser cavity oriented along the [1$\bar{1}$0] direction to the direction.

Structure	G_0-whole-structre	G_0-Per-layer
A ‖ (3QD/QDH)	17.5±0.4	5.8±0.1
B ‖ (5QD/QDH)	27.6±2	5.5±0.4
C‖ (like 3QW)	35.5±0.6	11.8±0.2
A`⊥ (3QD/QDH)	30.1±0.6	10±0.2
B`⊥ (5QD/QDH)	39±3	7.8±0.6
C`⊥ (like 3QW)	34.8±2	11.6±0.7

In table 7.1, A and B represent three-layer and five-layer lasers, respectively, with cavities oriented along the [1$\bar{1}$0] direction (parallel to the QD/QDH direction), while A` and B` have cavities aligned along the [110] direction (perpendicular to the QD/QDH direction). It is observed that laser diodes with cavities perpendicular to the QD/QDH direction exhibit approximately twice the value of gain parameter compared to those with cavities parallel to it. This suggests that these structures contain QDHs as the gain material rather than quantum dots. This variation in gain-parameter is due to the optical gain dependence on the electric field polarization [19,20]. For the specific dimensions of these QDHs, the transition matrix element is much larger when the electric field is aligned parallel to the dash direction. In other words, the light propagates perpendicular to the QDH's direction. The laser emission is strongly TE polarized, and this polarisation is expected to be strongly affected by cavity orientation for quantum dashes, whereas the QDH TM polarization is not affected by changes in the cavity orientation in the plane that is perpendicular to the direction of growth [13,19].

These findings show that and that while trying to grow dots by changing the growth conditions, in fact, we still have quantum dashes.

It is worth noting that the lower gain in the three-layer QDH laser compared to the five-layer QDH laser is attributed to its smaller active volume and lower confinement factor. The value being similar per layer. The low density and small size of the QDHs, combined with carrier saturation in the nanostructures, lead to lower gain. Therefore, stacking more layers is typically employed to increase the active region volume. As a result, the five-layer laser has higher gain parameters than the three-layer laser. From Table 7.1, it is also observed that the gain parameters for laser diodes C and C`, which use quantum wells, are approximately the same despite having different orientations, and higher than those obtained for the quantum dashes.

As shown in Figure 7.2 (TEM images) it appears that changing the active layer by maintain an indium content of 0.45, similar to Chapter 6, while adding aluminum to the capping layer has led to the formation of quantum wells instead of quantum dots or dashes.

The difference in the results between the two designs can be attributed to the materials used for capping the quantum dots, although other unintentional changes in growth can also lead to such a change. The formation of elongated quantum dash structures happens because the strain induces anisotropic surface diffusion of adatoms, causing the quantum dots to elongate into dashes [23]. The $In_{0.45}Al_{0.275}Ga_{0.275}As$ and $In_{0.45}Ga_{0.55}As$ (Chapter 6) capping layers add less highly strained material (relative to the InAs) than the $In_{0.35}Ga_{0.65}As$ and therefore there is less impetus to form either dots or dashes. The addition of aluminum (Al) in the alloy can also stabilize the material and prevent it from elongating into dashes, here leaving a quantum well structure [24]. While one would normally expect the material below the dots to have most affect here it seems that the capping layer also has a very important role. The introduction of aluminum (Al) into the alloy may contribute to stabilizing the material by reducing the diffusion of indium (In), preventing the formation of quantum dashes. This stabilizing effect occurs because aluminum alters the solubility and diffusion rates of indium (In) atoms. By limiting the mobility of indium, aluminum reduces the strain and anisotropic diffusion that could lead to rectangular quantum dash structures, promoting the formation of more stable quantum well structures.

7.5.6 External Differential Quantum (Slope) Efficiency

The differential quantum efficiency (η_{ext}), it is defined as the number of photons out per electrons in above threshold and thus reflects how well the laser converts current into light that is actually emitted from the device.

It can be determined experimentally from the derivative of the optical power versus current characteristics (P–I) above threshold as shown in Chapter 2. We note that P here is actually the light detected by the detector, which differs by some collection factor C, where C≤ 1, from the emitted power. We have recorded the P-I curves of the laser diodes with different cavity lengths under pulsed operation and used the slope above threshold current, as explained in Chapter 3. The ΔP/ΔI slope was multiplied by 2 because the laser diode with cleaved mirror facets emits equal amounts of light from both the front and back mirror facets and then multiplied by $[\frac{q\lambda}{hc}]$ to convert the optical power into a photon flux, as shown in Equation (7.1) [22].

$$\eta_{ext} = 2C \frac{\Delta P}{\Delta I} \frac{q\lambda}{hc} \qquad (I > I_{th}) \qquad (7.1)$$

$$\frac{1}{\eta_{ext}} = \left[\frac{\alpha_i}{C\ln(R^{-1})} L_c + 1\right] \frac{1}{C\eta_i} \qquad (7.2)$$

In Figure 7.11 the measurements show a large variation in the external differential quantum efficiency from different devices of the same length. This is most likely because in practice not all the light emitted by one facet is collected by the detector resulting in an apparent reduced differential quantum efficiency.

In an ideal, perfect laser, each electron-hole pair recombination event generates one photon, which travels through the laser waveguide structure and is emitted out of the cavity, contributing to the optical output.

In a real laser, some electron-hole pairs produce photons, while others generate unwanted energy like heat. Additionally, not all generated photons by the device are emitted out of the cavity. These factors can directly impact the external differential quantum efficiency values.

Accordingly, the measurements typically show the total current, which includes the external current entering the active region and the recombination current within the active region. The external current is partly lost due to current spreading and carrier leakage, while the recombination current is reduced by non-radiative processes. Additionally, heating due to the diode's series resistance, including contact resistances, can cause a reduction in the laser's power efficiency [25].

Moreover, the measured laser output power depends on experimental conditions, such as the distance between the sample and the integrating sphere, and the location of the integrating sphere relative to the device, which affects the magnitude of C. While I kept the distances constant in the experiment there will be some variation in C from device to device that will introduce some uncertainty in the measurement.

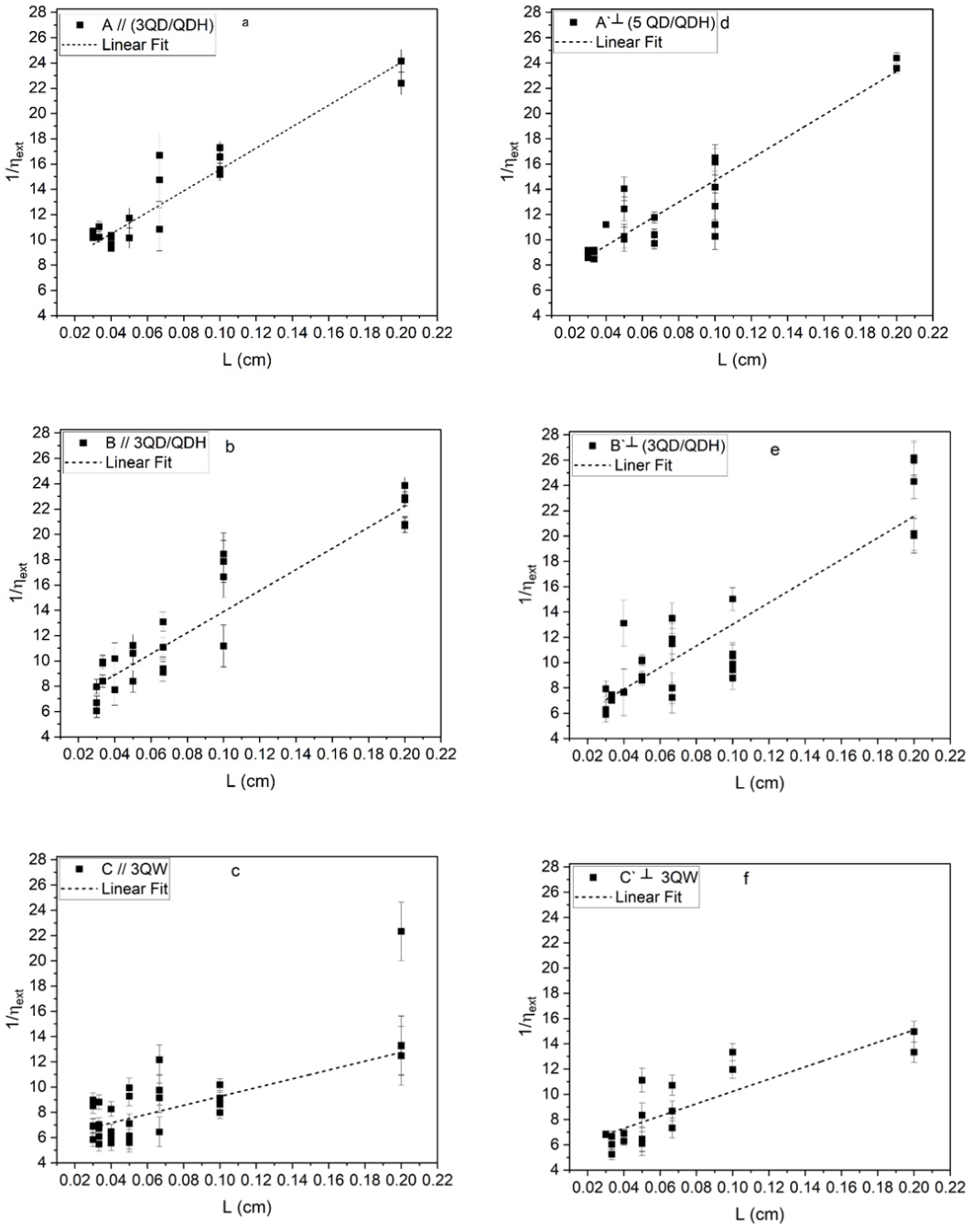

Figure 7: 11 Inverse external differential efficiency ($1/\eta_{ext}$) as a function of cavity length(L), (a) the three layer QDH (b) the five layer QDH (c) the three layer QW structure, all with the cavity aligned to the [$1\bar{1}0$] direction, and (d) the three layer QDH (e) the five layer QDH (f) the three layer QW, with the cavity aligned to the [110] direction. (Error bars indicate the standard error of the mean from multiple measurements of $1/\eta_{tot}$ at each L, calculated as SEM=$\sigma/\sqrt{n}$)).

7.5.7 Internal Differential Efficiency and Internal Optical Loss

The internal differential quantum efficiency is less dependent of the laser-device geometry, and it is related to the gain material. It is one of the key properties used to evaluate the quality of the semiconductor wafer used to fabricate the laser diode. This parameter represents the measure of the efficiency with which injected electrical current is converted into photons within the active region of the laser diode. The internal efficiency is affected by carrier processes such as current spreading, carrier injection and non-radiative processes.

From Figure 7.11, we can determine the internal differential efficiency (η_i) and internal optical loss (α_i) for different structures, by fitting Equation (7.2). The y-intercept is the reciprocal of the internal efficiency, and the slope can be used to give us the value of the internal optical loss. For each structure, the experimentally determined internal differential efficiency η_i and internal loss α_i are shown in Table 7.2 [22].

Table 7.2. Values of the internal differential efficiency (η_i) and internal optical loss (α_i), for different structures with the laser cavity oriented along the [110] direction, and the laser cavity oriented along the [1$\bar{1}$0] direction to the dash direction.

Structure	η_i%	$\propto_i (cm^{-1})$	Note
A ‖	**14 ±1**	**14.4 ±1.8**	**3QDH**
B ‖	**18 ±2**	**18.1 ±1.4**	**5QDH**
C ‖	**17 ±2**	**10.3 ±2.5**	**like 3QW**
***A*`⊥**	**16±1**	**17.1 ±1.2**	**3QDH**
B`⊥	**22 ±2**	**22.9 ±3.2**	**5QDH**
***C*`⊥**	**19±1**	**11 ±2.3**	**like 3QW**

Since the samples A and A', B and B', as well as C, and C` are made of the same wafer, the internal efficiency and the material optical losses would likely be the same. Experimental results show that the values of η_i and α_i for these structures are approximately the same when accounting for the experimental error. Summarising as the average values internal quantum efficiency (internal optical loss) values of 15±1.4

(~15.8 ±2.2cm^{-1}), 20 ±2.8 (~20.5 ± 3.5cm^{-1}), are found for the three and five-layer QDH lasers, respectively, while the QW samples had values of 18±2.2 (~11±3.4cm^{-1}). The reflectivity (R) used is calculated to be 0.28 for the cleaved facets.

Since the laser structures A and A', as well as B and B', were identical except for the number of QDH layers, the differences in η_i and α_i are likely to have arisen from the varying number of layers

The internal differential quantum efficiency shows how effectively a laser converts electron-hole pairs (created by the injected current) into light (photons) within the laser diode itself. Consequently, a low internal differential quantum efficiency indicates that a small proportion of the carriers contribute to photon generation. A large proportion are lost to non-radiative processes such as defect recombination and Auger recombination.

It is clear from Table 7.2 that all the samples feature relatively high internal optical loss, and this may be due to several reasons, including scattering and absorption. Generally, the internal optical loss in laser diodes can increase due to several design and fabrication-related factors. For example, the thickness of the waveguide layer can impact internal optical losses, i.e. a thicker waveguide layer can reduce leakage of light into the cladding or substrate, thus reducing losses. Additionally, fabrication processes can introduce structural defects, impurities, and roughness in the waveguide, which scatter light and increase losses. Free-carrier absorption may also occur when free carriers (electrons and holes) in the active region and waveguide absorb photons, leading to higher internal optical losses [21] Thus, understanding and managing these factors is crucial for optimizing laser diode performance. To better understand the origin of the high internal optical loss, segmented contact multi-section devices were fabricated, and used to characterise the optical gain and absorption. These measurements are described in section 7.7 following further characterisation of the lasing wavelength and temperature dependence of threshold current density.

7.5.8 Wavelength

The photoluminescence (PL) spectra were measured at room temperature by Qiang Li to investigate the spectral emission range of the dot ensemble, where the peak height can be a measure of quality. In Figure 7.12, we can observe two subfigures (a) and (b) that provide insight into the photoluminescence and emission spectra of three different test structures: A, B, and C.

In Figure 7.12(a), we observe a peak wavelength at 1550 nm for sample A, 1500 nm for sample B, and 1540 nm for sample C. It is noteworthy that laser structures A and B show different PL peak wavelengths despite being nominally identical, except for the number of QDH layers, which may indicate that the growth conditions were not identical. This suggests that the dot formation is extremely sensitive to growth conditions. Sample B, the peak is broader and shifted to shorter wavelengths or blue shifted. This could be because of strain in the material especially in the extra layers, which changes how the light is emitted.

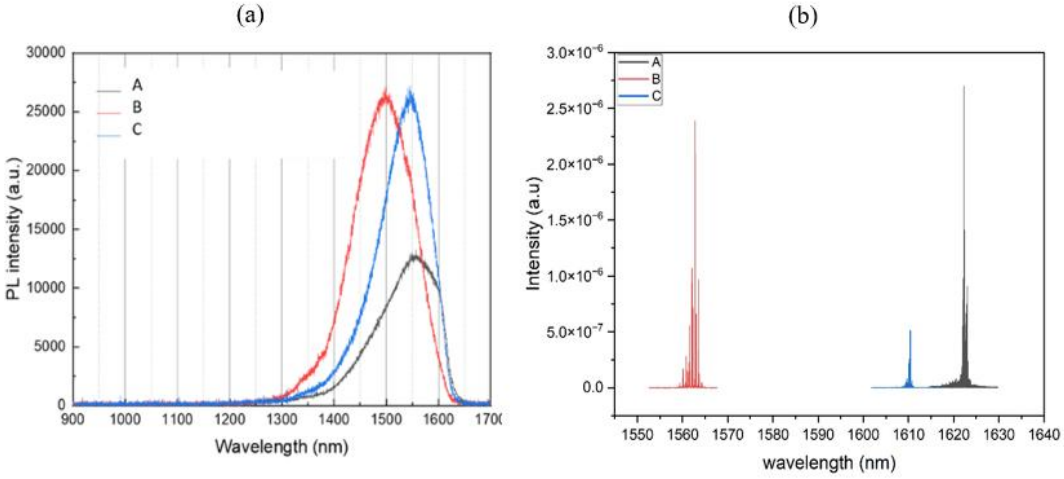

Figure 7.12: (a) PL for test structures. A the three layer QDH (black), B the five layer QDH (red) and C the three layer QW (blue). Measurement results were supplied by Dr Qiang Li. (b) emission spectra at 1.1xith for laser devices with cavity length 1000 µm.

Figure 7.12(b) shows the emission spectra during lasing, measured at a current 1.1 times the threshold showing how the material emits light when electrically excited in

a laser. This emission is different from the natural emission and depends on the material and cavity properties.

The peak laser wavelength as a function of cavity length for the lasers is plotted in Figure 7.13 and illustrates the operational range of these laser structures, spanning from 1520 to 1620 nm and covering both the C-band and L-band.

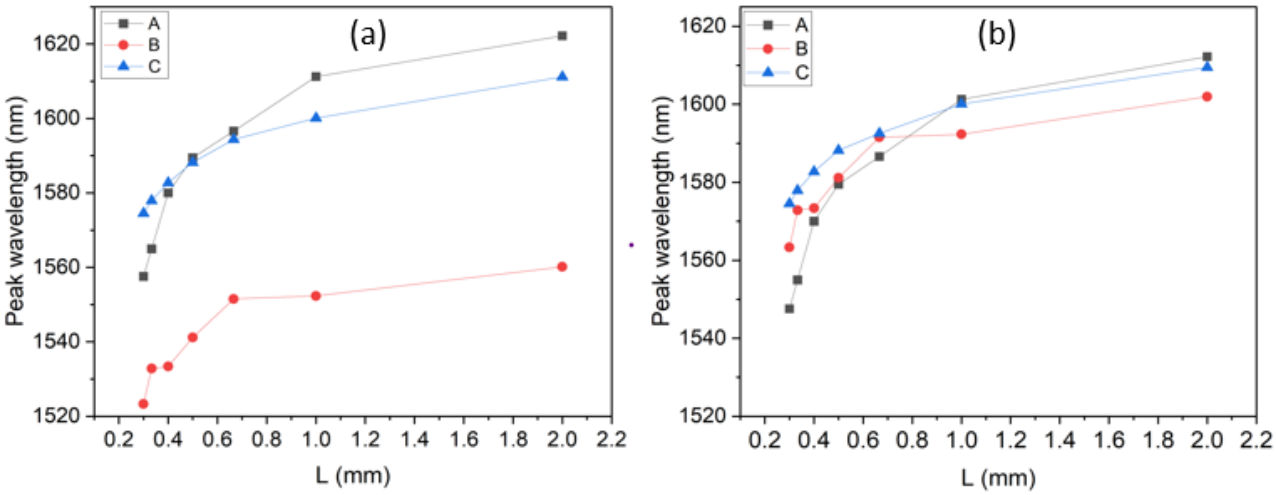

Figure 7.13: a) Peak lasing wavelength at room temperature (21±1°C) as a function of cavity length for laser devices: A, the three layer QDH (black squares); B, the five layer QDH (red circles); and C, the three layer QW (blue triangles). b) A second-order polynomial fit to each data set where the sample B data has been shifted by the difference in wavelength of the PL peaks.

Figure 7.13(b) shows the peak wavelength data for sample B, which has been shifted by the difference in wavelength observed in the PL measurements from Figure 7.12. This adjustment allows for a more straightforward comparison with samples A and C. By accounting for the differences in the PL peak wavelengths, the data focuses on the influence of the cavity length on the lasing wavelength, eliminating material property variations and enabling a clearer analysis of the laser behaviour.

The seemingly large offset in laser wavelength of sample B is simply due to the large change in the dash formed during growth and the wavelength of the material as seen in Figure 7.13 where the laser results are offset by the PL wavelength difference from Figure 7.12.

7.6 Temperature Dependence of Threshold Current

The threshold current density is measured for structures A, B and C and for different device lengths and as function of temperature and plotted in Figure 7.14. We observe that the 3-layer QD sample only lasers up to 330 K whereas the 5-layer samples lase up to 370 K. This suggest the higher gain obtained in the 5-layer sample is important for achieving better performance. The lasers made with a QW active material have a much better threshold current temperature dependence operating up to 380 K, and, also showing a smaller difference in values between lasers of different length. This again suggests that it is the magnitude of the gain available which is the critical factor in achieving good performance.

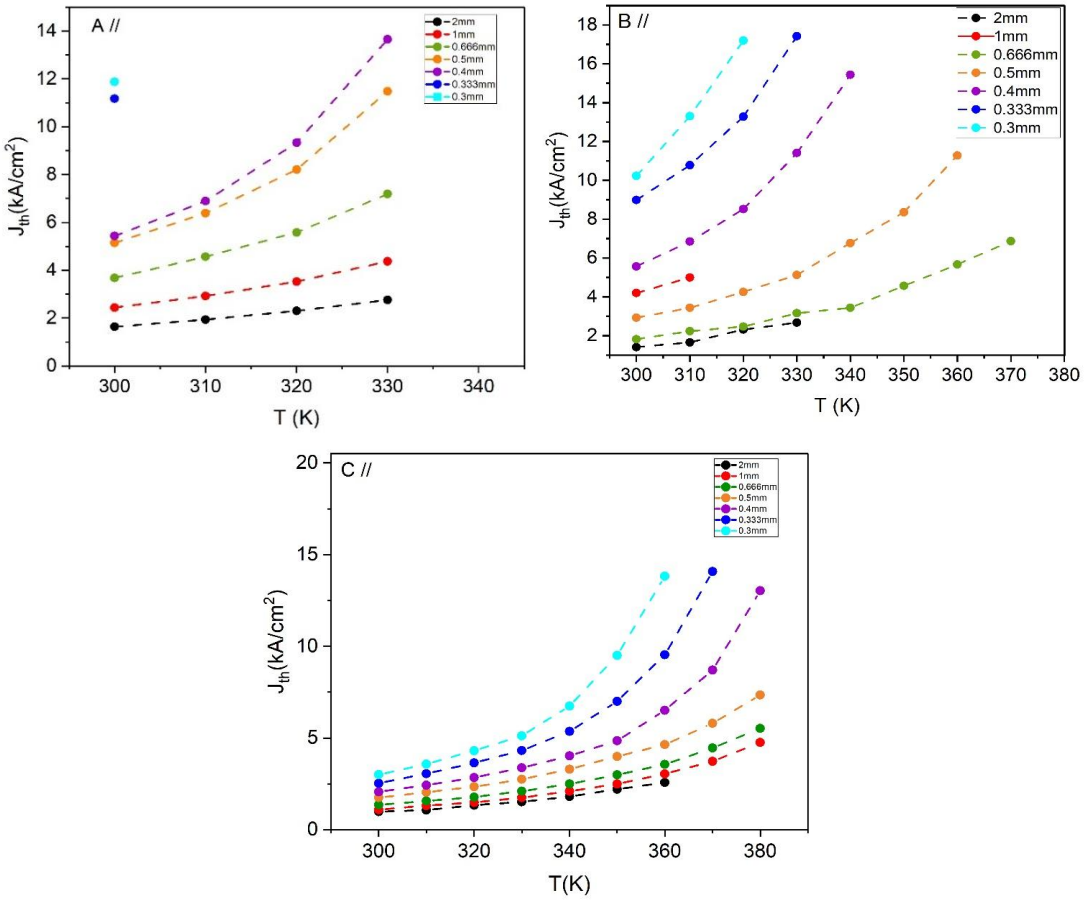

Figure 7.14: Temperature dependence of threshold current function of cavity length for laser devices: A, the three layer QD; B, the five layer QD and C, the three layer QW structure, all with the cavity aligned to the [1$\bar{1}$0] direction.

In Figure 7.14 the temperature dependence of the threshold current is illustrated for the growth direction of high-gain structures. For the 3-layer QD sample, the lasers operate effectively up to 350 K. In sample B, which consists of 5 layers, operation extends up to 370 K; however, the difference in values between lasers of different lengths becomes smaller at higher temperatures. This indicates that higher gain produces better results in terms of the temperature dependence of the threshold current. Similarly, lasers made with a quantum well active material exhibit the same temperature dependence of the threshold current, operating effectively up to 380 K.

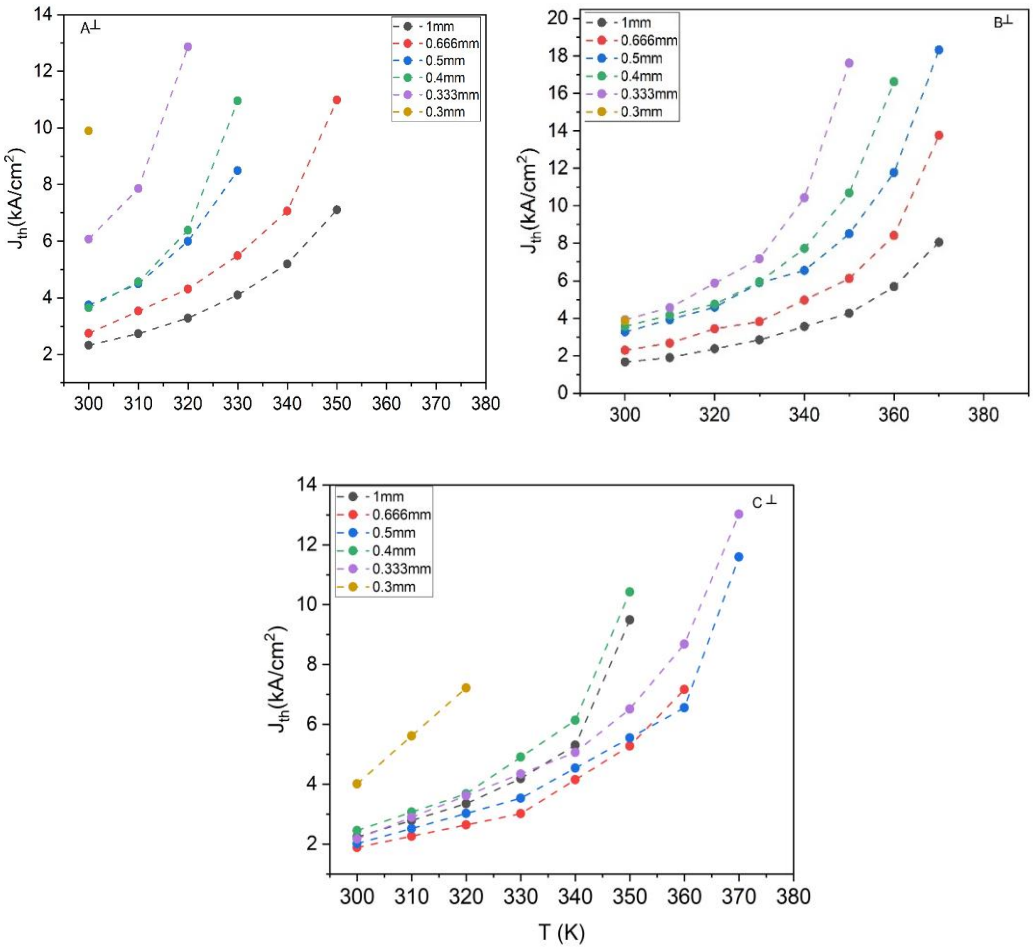

Figure 7.15: Temperature dependence of threshold current function of cavity length for laser devices: A, the three layer QD; B, the five layer QD and C, the three layer QW structure, all with the cavity aligned to the [110] direction.

I return to the issue of the high optical loss, which seems to be affecting the performance of these devices significantly. Figure 7.16 shows a near-field image of a multi-section device, that was taken by Dr. Curtis Hentschel, when the third section was electrically pumped, while the first and second sections were grounded such that the active region in those sections remained absorbing. Light associated with the waveguide mode and light that has leaked out of the waveguide and into the substrate are both apparent.

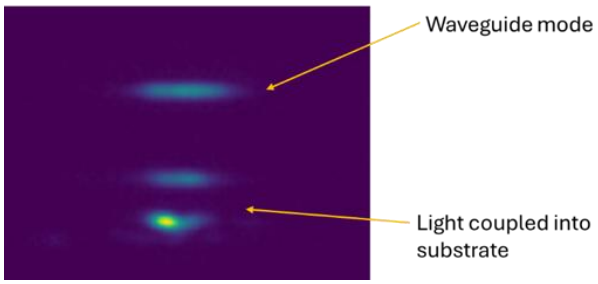

Figure 7.16: Near-field Image of a segmented contact device fabricated from the three-layer QW structure that had been ion-implanted to improve the electrical isolation between sections. The third section was electrically pumped, while the first and second sections were grounded.

The segmented contact structure may be more prone to a mode in the substrate that the actual laser devices. This is because the top contact layer is etched between the sections and ion implantation is used between the sections to increase resistance further. Such changes may also reduce the refractive index above the active layer, and this can have the effect of pushing the optical mode towards the substrate. Therefore, it is also necessary to determine whether light was also leaking into the substrate for the laser structures. The near-fields were measured with a 50x microscope objective lens to image the substrate-coupled light, if any. The high magnification also helps to spatially filter out the high intensity lasing mode in the waveguide core, as the lasing mode image can be projected outside the pixel array of the camera while still allowing the low intensity light in the substrate to be captured by the camera. The high magnification also prevented the entire structure to be imaged so individual images were taken as shown in Figure 7.17. (a) shows the lasing mode within the waveguide core, (b and c) show the region below the waveguide core and includes the substrate, and (d) shows the bottom of entire structure. It is clear from the picture, the presence

of light in an area (b and c) between the core and the bottom of the substrate. As light in the substrate suggests either a much larger mode, which intersects with more interfaces and more doped material, or light that is completely lost from the waveguide, it is likely that the optical losses will increase considerably due to the effects described above. Since the extended mode will not generate any additional gain and there are likely to be higher optical losses this leakage into the substrate will be detrimental to laser action making the current density much higher than it needs to be.

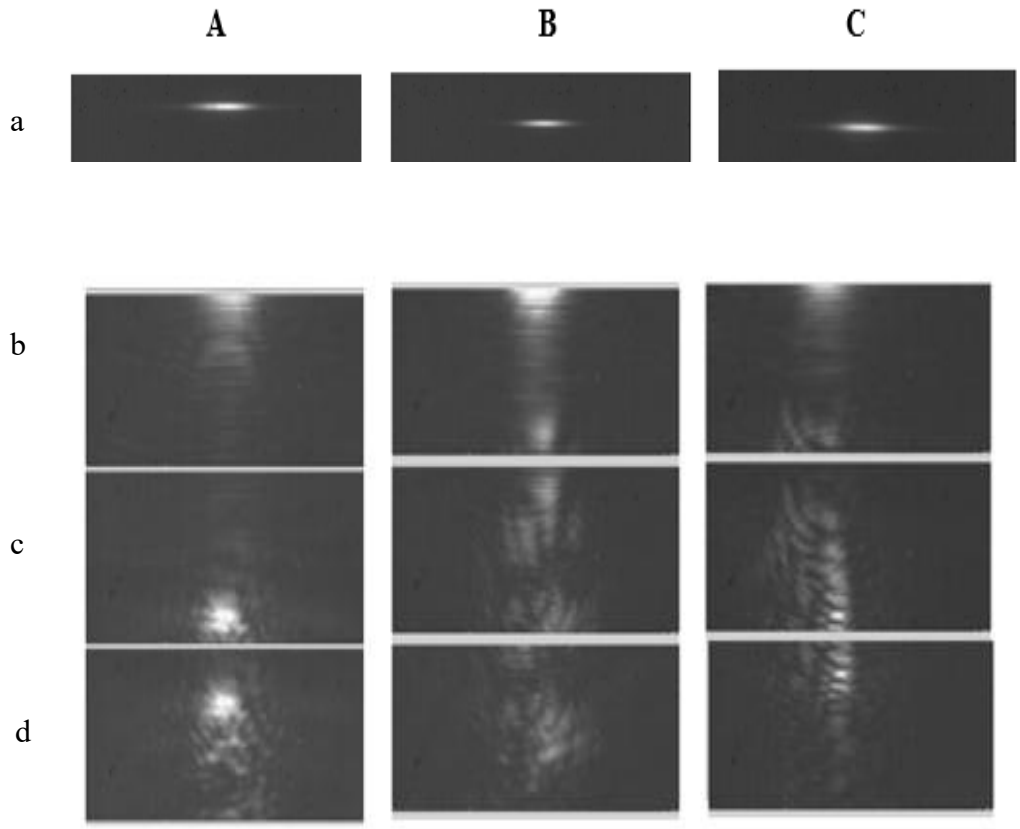

Figure 7.17: Near-field images of a three-layer QD (A), a five-layer QD (B), and a three-layer QW (C) laser sample. (a) shows the lasing mode within the waveguide core, (b) and (c) show the region below the waveguide core, including the substrate, and (d) shows the bottom of the entire structure.

A simulation using Fimmwave software was performed by Dr. Fwoziah Albeladi. The electric field profile of the TE_{00} mode for the three structures A, B, and C, were analysed using a 2-D waveguide finite difference method (FDM) solver using Fimmwave software from Photon Design [26–28]. This analysis focused on determining

whether the electric field decays exponentially toward zero at the substrate boundaries. In these calculations, the substrate was not included to avoid the need for a significantly increased resolution, which was required to accurately account for the thin layers in the waveguide core. Including the substrate would have substantially increased the simulation time. For clarity, the zero point on the x-axis in Figure 7.18 represents the substrate boundary.

Figure 7.18 presents the vertical distribution of the electric field for the fundamental TE_{00} mode in the three structures. The Figure shows that for all three structures, the electric field is nearly zero at the top boundary, indicating that the thickness of the upper cladding is sufficient to confine the optical mode effectively.

For the lower cladding, the calculations reveal that the electric field at the lower boundary (i.e., at the substrate) is approximately ~0.097, 0.084, and 0.073 for structures C, A, and B, respectively. These values suggest that the thickness of the lower cladding is insufficient to avoid the mode from escaping into the substrate. This simulation confirms the existence of leakage to the substrate layer in all three structures. The observed increase in structure C could be attributed to the presence of the aluminum in the capping layer. However, when aluminum was added to structures A and B in the calculation, where it was absent in the measured structures, only a slight increase in leakage toward the substrate layer was observed.

The differences are small, and it is unlikely to be the exact magnitude of the light reaching the substrate that is the dominate factor, given C has a larger value than A and B. The differences in interface roughness and doping level in the cladding and substrate regions are more likely to affect the precise value of α_i in the lasers. However, such opportunity for extra loss could be removed by designing lasers with better confinement to keep the optical mode within the core of the device.

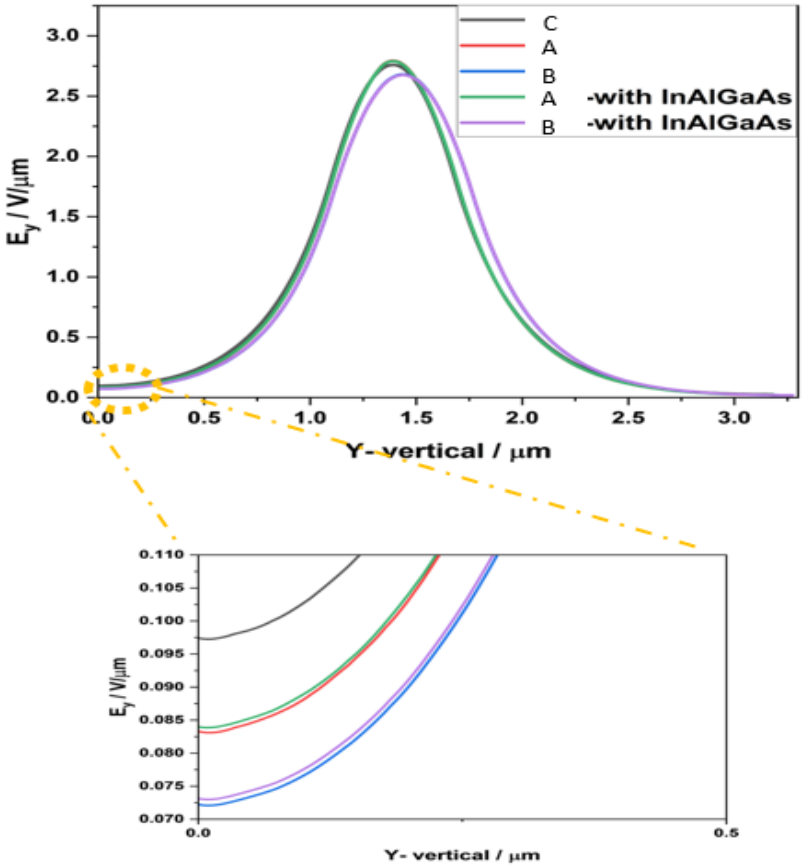

Figure 7.18: Simulation in Fimmwave software was performed by Dr.Fwoziah Albeladi. Showing vertical distribution of the electric field for the TE00 mode in structures A, B, and C. The electric field vanishes towards zero at the upper boundary, while the field at the substrate boundary is non-zero, indicating insufficient containment in the lower cladding for all three structures.

The optical losses are also determined using the segmented contact method, similar to the approach taken in study [14], to confirm the high values of optical loss, see the next section (7.7).

7.7 Gain and absorption measurements

We will discuss in this section the gain and absorption measurements for samples B(5QD) and C(3QW), while sample A is excluded because there was insufficient material to fabricate the segmented contact samples.

The gain and absorption spectra were measured using the segmented contact method, as described in Chapter 3. These measurements were carried out by Dr. Curtis

Hentschel. The segmented contact devices, which were used for this determination, were fabricated by Dr. Zhongming Cao. The devices featured individual segments measuring 150 µm long with a Ti/Pt/Au top contact that was 142 µm long. There were 8 µm wide gaps between sections to ensure electrical isolation between the contacts. These were etched to a depth of 50 nm removing the highly doped contact layer. Ion implantation was used to increase the isolation between sections.

The characteristics of the gain section were investigated under different current densities. Figures 7.19 and 7.20 show the net modal gain and absorption of structures B and C. These values were obtained and measured at currents ranging from approximately 60 mA to 270 mA at 300K. Key parameters, such as internal optical loss, gain amplitudes, and gain bandwidth, can be extracted from the gain and absorption curves at different injected current.

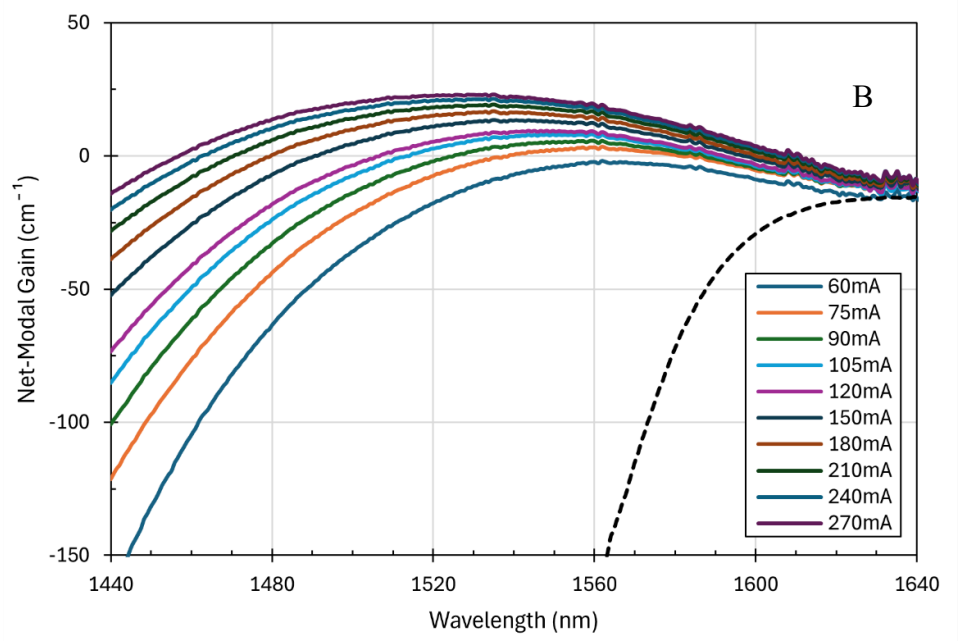

Figure 7.19: The net optical gain as a function of wavelength for the B (5QD) structure, obtained from segmented contact measurements, for different injection currents at room temperature (21±1°C). [Data provided by Dr.Curtis Hentschel].

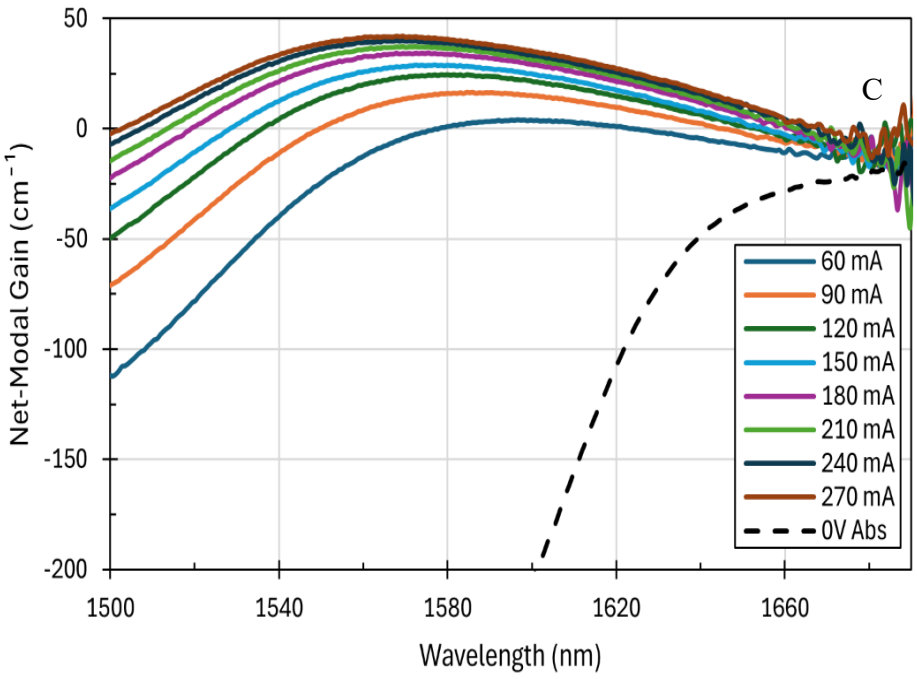

Figure 7.20: The net optical gain as a function of wavelength for the C (3QD) structure, from segmented contact measurements at room temperature (21±1°C), is shown for different injection currents, [Data provided by Dr.Curtis Hentschel].

The internal optical loss can be determined from the long-wavelength region beyond the gain and absorption curve's band edge. For structure B, it is approximately 15±3 cm^{-1}, whereas for structure C, it is around 18±3 cm^{-1}. The large loss is similar to that obtained from the laser data although the relative magnitudes are reversed compared to earlier, and this is in better agreement with the optical mode calculations where the amplitude of the electric field at the substrate was larger for sample C.

The peak modal gain rises with increasing injected current density, attributed to state filling of energy levels. For structure B, the gain peaks saturate at approximately 24±2 cm^{-1} at the highest injected current density. A similar trend is observed for structure C, with the gain peaks saturating at around 40±2 cm^{-1}. The gain saturation is due to states being filled with carriers [22]. The gain peak is saturated at the high gain peak of the C structure compared to the B structure. Both are lower than the value measured in Chapter 6 but here we have either 5 layers of dashes or 3 layers of QWs compared with the 5 layers of QWs in Chapter 6. The gain in quantum wells is generally higher

due to the higher density of states. In contrast, QDs, due to their discrete energy levels, experience significant state-filling effects. Once the available states are occupied, additional carriers cannot easily contribute to the gain, which leads to a saturation effect. The gain bandwidth of both structures is relatively broad around ~150 nm for both structures. For structure B, the broad gain bandwidth is attributed to inhomogeneous broadening caused by size effects and variations in the size distribution of the quantum dashes [29,30] . These variations lead to differences in their energy levels, resulting in a broader gain spectrum [31] . In structure C, the broad gain bandwidth may be due to the modulated width /composition of the well seen in the TEM images [32,33].

7.8 Results Summary

In this work, we compared experimentally, three laser diode structures with InAs based active layers were grown by MOCVD on an InP (001) substrate. TEM suggests that structures A and B are either dots or dashes, and TEM suggests structure C is QWs. We investigated laser diodes fabricated from these structures with two different orientations: A, B and C which had the axis of the laser cavity aligned along the $[1\bar{1}0]$ direction, and A`, B`, and C` which had the cavity oriented in the [110] direction. Structures with dashes should have a higher gain when the laser cavity is fabricated in the [110] direction. Indeed, we found that lasers fabricated from A and B to have higher gain parameters along the [110] direction. Sample C showed similar threshold current behaviour in both orientations, as would be expected for quantum wells. Internal parameters were analyzed from the device results to facilitate better material evaluation and future enhancements. These lasers exhibit low gain, high optical loss, and low internal efficiency. We primarily attribute these outcomes to the lower level of homogeneity in this type of active laser material, which results in lower gain compared to the more commonly used quantum well active regions. The low efficiency suggests_high values of non-radiative recombination perhaps due to high defect densities and there is significant potential for improvement.

The results of laser measurements, along with gain and absorption spectra were measured using the segmented contact method SCM, revealed the following findings: the gain coefficients for the laser measurements of the samples were 17.5 ± 0.4 cm^{-1} for sample A, 27.6 ± 2 cm^{-1} for sample B, and 35.5 ± 0.6 cm^{-1} for sample C. The net modal gain and absorption measurements, where the maximum net gain was measured as 24 cm^{-1} for sample B and 40 cm^{-1} for sample C.

The internal optical loss was evaluated; high values were observed in both the laser measurements and the gain and loss measurements using SCM. Specifically, sample A exhibited a loss of approximately ~15.8 ± 2.2 cm^{-1}, sample B had a loss of ~20.5 ± 3.5 cm^{-1}, and sample C showed a loss of ~11.0 ± 3.4 cm^{-1}. Similarly, in the gain and absorption measurements, sample B showed a loss of about 15 ± 3 cm^{-1}, and sample C showed a loss of approximately 18 ± 3 cm^{-1}. The gain bandwidth of both structures is relatively broad around ~150 nm for both structures, which is wider than that seen in Chapter 6 (130 nm).

In comparing results to the earlier samples from Chapter 6 we see that the internal optical loss is much higher here; it was found to be approximately, $\alpha_i \approx 5 \pm 3$ cm^{-1} for Chapter 6. It is not clear whether the lower value is due to a random effect, but the very similar designs of this Chapter do not result in low losses.

Measurements of how the threshold current density depends on temperature for structures A, B, and C reveal that the 3-layer dash sample operates up to 330 K, whereas the 5-layer sample extends its performance to 370 K. This suggests that increased gain and reduced carrier loss, supported by a larger energy offset at longer wavelengths, enhance efficiency. Lasers with quantum well QW active material demonstrate the best performance, operating up to 380 K with excellent threshold current temperature stability and minimal variation across device lengths. These results underscore the importance of high gain for achieving superior laser operation. However, QWs are not typically insensitive to defects so dots or dashes are probably necessary for integration with silicon.

The use of quantum dots QDs for InP/Si monolithic integration in Si photonics presents a potential future manufacturing alternative to the bonding of long-wavelength telecom light sources onto CMOS-compatible silicon substrates, considerable improvements are required. In particular the better confinement of light in the active region is critical to reduce optical loss and make better lasers and also to facilitate traditional methods of analysis for feedback and further material improvement.

References

1. Grillot, F., Norman, J.C., Duan, J., Zhang, Z., Dong, B., Huang, H., Chow, W.W. & Bowers, J.E. Physics and applications of quantum dot lasers for silicon photonics. *Nanophotonics*, vol 9(6), 1271–1286 doi.org/10.1515/nanoph-2019-0570 (2020).

2. Xiao, Z., Liu, W., Xu, S., Zhou, J., Ren, Z. & Lee, C., Recent Progress in Silicon-Based Photonic Integrated Circuits and Emerging Applications. Advanced Optical Materials, vol 11(20), 2301028. doi.org/10.1002/adom.202301028 (2023).

3. Pan, S., Cao, V., Liao, M., Lu, Y., Liu, Z., Tang, M., Chen, S., Seeds, A. & Liu, H. Recent progress in epitaxial growth of III-V quantum-dot lasers on silicon substrate. *Journal of Semiconductors.* vol 40(10), p.101302. doi.org/10.1088/1674-4926/40/10/101302 (2019).

4. Shang, C., Wan, Y., Selvidge, J., Hughes, E., Herrick, R., Mukherjee, K., Duan, J., Grillot, F., Chow, W.W. & Bowers, J.E., Perspectives on Advances in Quantum Dot Lasers and Integration with Si Photonic Integrated Circuits. *ACS Photonics*.vol. 8(9),2555–2566. doi.org/10.1021/acsphotonics.1c00707 (2021).

5. Khan, M. Z. M., Ng, T. K. & Ooi, B. S. Self-assembled InAs/InP quantum dots and quantum dashes: Material structures and devices. *Progress in Quantum Electronics* vol. 38(6), 237-313. doi.org/10.1016/j.pquantelec.2014.11.001 (2014).

6. Cao, V., Park, J.S., Tang, M., Zhou, T., Seeds, A., Chen, S. & Liu, H. Recent Progress of Quantum Dot Lasers Monolithically Integrated on Si Platform. *Frontiers in Physics* vol.10, 839953.doi.org/10.3389/fphy.2022.839953 (2022).

7. Shang, C., Wan, Y., Selvidge, J., Hughes, E., Herrick, R., Mukherjee, K., Duan, J., Grillot, F., Chow, W.W. & Bowers, J.E., Perspectives on Advances in Quantum Dot Lasers and Integration with Si Photonic Integrated Circuits. *ACS Photonics* vol. 8 2555–2566. doi.org/10.1021/acsphotonics.1c00707 (2021).

8. Reithmaier, J. P., Eisenstein, G. & Forchel, A. InAs/InP quantum-dash lasers and amplifiers. *Proceedings of the IEEE* 95(9), 1779-1790 (2007).

9. Norman, J. C., Mirin, R. P. & Bowers, J. E. Quantum dot lasers History and future prospects. *Journal of Vacuum Science & Technology A: Vacuum, Surfaces, and Films* 39 (2), (2021).

10. Norman, J.C., Jung, D., Zhang, Z., Wan, Y., Liu, S., Shang, C., Herrick, R.W., Chow, W.W., Gossard, A.C. and Bowers, J.E. A review of high-performance quantum dot lasers on silicon. *IEEE Journal of Quantum Electronics* vol. 55(2), 1-11. doi.org/10.1109/JQE.2019.2901508 (2019).

11. Zilkie, A.J., Meier, J., Mojahedi, M., Poole, P.J., Barrios, P., Poitras, D., Rotter, T.J., Yang, C., Stintz, A., Malloy, K.J. and Smith, P.W. Carrier dynamics of quantum-dot, quantum-dash, and quantum-well semiconductor optical amplifiers operating at 1.55 μm. *IEEE J Quantum Electron* 43(11), 982-991 (2007).

12. Grillot, F., Duan, J., Dong, B. & Huang, H. Semiconductor quantum dot lasers: Genesis, prospects, and challenges. in *Quantum Photonics* 191-266. Elsevier, (2024). doi:10.1016/B978-0-323-98378-5.00008-8.

13. Khan, M. Z. M., Ng, T. K. & Ooi, B. S. Self-assembled InAs/InP quantum dots and quantum dashes: Material structures and devices. *Progress in Quantum Electronics* vol. 38(6), 237-313etdoi.org/10.1016/j.pquantelec.2014.11.001 (2014).

14. Li, Z., Shutts, S., Xue, Y., Luo, W., Lau, K.M. and Smowton, P.M. Optical gain and absorption of 1.55 μ m InAs quantum dash lasers on silicon substrate. *Applied Physics Letters*, 118(13). (2021).

15. Xue, Y., Luo, W., Zhu, S., Lin, L., Shi, B. and Lau, K.M., 1.55 μm electrically pumped continuous wave lasing of quantum dash lasers grown on silicon. *Optics Express,* 28(12),18172-18179 (2020).

16. Torchynska, T. V., Casas Espinola, J. L. & Stintz, A. Impact of capping layer type on emission of InAs quantum dots embedded in

InGaAs/InxAlyGazAs/GaAs quantum wells. in *Journal of Applied Physics* vol. 115(1). (2014).

17. Yuan, J., Dear, C., Jia, H., Park, J.S., Hou, Y., El Hajraoui, K., Zeng, H., Deng, H., Yang, J., Tang, M. and Chen, S. Indium-flush technique for C-band InAs/InP quantum dots. *APL Materials* 12 (12)., (2024).

18. Ko, F. K. & Wan, Y. Characterization of nanofibers. *Introduction to Nanofiber Materials*. Cambridge University Press 101-145. (2014) doi:10.1017/CBO9781139021333.007.

19. Wang, R.H., Stintz, A., Varangis, P.M., Newell, T.C., Li, H., Malloy, K.J. & Lester, L.F. *Room-Temperature Operation of InAs Quantum-Dash Lasers on InP (001)*. *IEEE Photonics Technology Letters*, 13(8).767-769. (2001).

20. Ukhanov, A.A., Wang, R.H., Rotter, T.J., Stintz, A., Lester, L.F., Eliseev, P.G. and Malloy, K.J., Orientation dependence of the optical properties in InAs quantum-dash lasers on InP. *Applied physics letters,* 81(6), 981-983. (2002).

21. Coldren, L.A., Corzine, S.W. and Mashanovitch, M., *Diode Lasers and Photonic Integrated Circuits*. (Vol. 218). John Wiley & Sons. (2012).

22. Blood, P. *Quantum Confined Laser Devices: Optical Gain and Recombination in Semiconductors*. vol. 23, OUP Oxford, (2015).

23. Liew, S.L., Walther, T., Irsen, S., Hopkinson, M., Skolnick, M.S. and Cullis, A.G., *Investigating the Capping of InAs Quantum Dots by InGaAs*. In Microscopy of Semiconducting Materials, 259-262. Springer Netherlands. (2007).

24. Jung, D., Ironside, D. J., Bank, S. R., Gossard, A. C. & Bowers, J. E. Effect of growth interruption in 1.55 μ m InAs/InAlGaAs quantum dots on InP grown by molecular beam epitaxy. *Journal of Applied Physics,* 123(20)., (2018).

25. Blood, P. Quantum Efficiency of Quantum Dot Lasers. *IEEE Journal of Selected Topics in Quantum Electronics* 23(6).1-8., (2017).

26. Photon Design Ltd. "FIMMWAVE." https://www.photond.com/products/fimmwave.htm (accessed 2024).

27. Photon Design Ltd. https://www.photond.com/index.htm (accessed 2024).

28. Photon Design Ltd. "The FDM solver." https://www.photond.com/products/fimmwave/fimmwave_features_22.htm (accessed 2023).

29. Lelarge, F., Dagens, B., Renaudier, J., Brenot, R., Accard, A., Van Dijk, F., Make, D., Le Gouezigou, O., Provost, J.G., Poingt, F. and Landreau, J., Recent Advances on InAs/InP Quantum Dash Based Semiconductor Lasers and Optical Amplifiers Operating at 1.55 μm. *IEEE Journal of Selected Topics in Quantum Electronics* 13(1), 111–124 (2007).

30. Ooi, B.S., Djie, H.S., Wang, Y., Tan, C.L., Hwang, J.C., Fang, X.M., Fastenau, J.M., Liu, A.W., Dang, G.T. and Chang, W.H., Quantum dashes on inp substrate for broadband emitter applications. *IEEE Journal on Selected Topics in Quantum Electronics* 14(4), 1230-1238 (2008).

31. Maximov, M.V., Gordeev, N.Y., Shernyakov, Y.M., Kornyshov, G.O., Beckman, A.A., Payusov, A.S., Mintairov, S.A., Kalyuzhnyy, N.A., Kulagina, M.M. and Zhukov, A.E., Superluminescent Diodes Based on Chirped InGaAs/GaAs Quantum Well-Dot Layers. *In Photonics.* Vol. 10 (10), 1090., (2023).

32. Chen, S., Zhou, K., Zhang, Z., Orchard, J.R., Childs, D.T., Hugues, M., Wada, O. and Hogg, R.A. Hybrid quantum well/quantum dot structure for broad spectral bandwidth emitters. *IEEE Journal of Selected Topics in Quantum Electronics*, 19(4),.1900209. (2012).

33. Chuang, S. L. *Physics of Photonic Devices*. John Wiley & Sons, 25 (2012).

Chapter 8: Conclusions

8.1 Introduction

In this thesis, we sought to understand InAs/InP quantum dot QD lasers and to assess whether they can be suitable for integration on silicon for lasers and as sources for photonic integrated circuits (PICs) operating around 1550 nm. At 1300 nm InAs/GaAs QD lasers have demonstrated an insensitivity to defects, operation up to high temperature but have failed to perform well when the cavity length is reduced below approximately 1mm.

Although quantum dot lasers have already been grown on silicon substrates, further advancements are required to reduce operating current and lower energy consumption, particularly under high-temperature conditions. Despite considerable progress, InAs/InP quantum dot lasers on silicon and native III-V substrates still encounter challenges compared to quantum well devices grown on native III-V substrates. These challenges include relatively high threshold current density at room temperature, a significant rise in operating current at higher temperatures, and lower optical gain. Overcoming these issues is crucial for achieving reliable high-temperature performance in long-wavelength lasers for integrated optoelectronic applications [1–5].

While we did not have samples grown on silicon, we set out to understand whether InAs-on InP lasers could operate with short cavity lengths and at high temperature for applications requiring longer wavelengths.

In Chapter 4, The power-current characteristics of quaternary AlGaInAs/InP multi-quantum-well MQW laser diodes with six and nine quantum well (QW) layers were analyzed, revealing a strong dependency of gain parameters on the number of quantum wells in the active region. Notably, the structure with nine QW layers demonstrated the highest gain coefficient, measured at 94.4 cm^{-1}. A gain per QW of > 10 cm^{-1} is achieved in both structures.

Simulations presented in Chapter 5 highlight the benefits of incorporating an electron stopper layer in the operation of AlInGaAs/InP MQW laser diodes to achieve highly optimized performance for long waveguides. The results demonstrate that the electron

stopper layer does not impede carrier injection into the active region while significantly reducing thermionic emission of carriers from the active layer and minimizing electron leakage into the p-cladding layer, particularly at elevated temperatures. This improvement enhances the threshold current density and overall efficiency of the devices.

In Chapter 6, lasers with 5 layers of active material and similar to a previous design from the literature, were assessed as function of cavity length and temperature. Lasers grown on n-InP exhibited an emission wavelength ranging from 1560 nm to 1600 nm, with cavity lengths varying from 300 μm to 2000 μm at 21°C. As the cavity length increased from 300 μm to 2000 μm, the threshold current density decreased from approximately 2.2 kA/cm² to around 1 kA/cm². It was observed that the threshold current density increased consistently with temperature across all cavity lengths. For the longest 2000 μm cavity, the threshold current density increased by a factor of 3.4 from 300 K to 380 K, while for the shortest 300 μm cavity, it increased by a factor of 3.8. Moreover, a laser with a 300 μm cavity can function effectively at temperatures up to 380 K, indicating that the laser structure is suitable for operation over a wide temperature range. Importantly, the peak lasing wavelength does not exhibit any noticeable transition from the ground state to the excited state. Even for cavity lengths as short as 300 μm, the laser sustained stable ground-state lasing at temperatures up to 380 K.

Gain measurements using the multi-section or segmented contact method 6 showed a modal gain peak of 60 cm^{-1} at an injection current of 200 mA. No gain saturation was observed. Positive gain was observed over a wide wavelength range of 130 nm indicating the material could be very useful as source for different wavelength or tunable wavelength lasers. The measurements also suggested a value of internal optical mode loss of approximately 5 ± 3 cm^{-1}, low compared to previous literature values. The primary difference in the design of the structure compared to the previous work was an $In_{0.45}Ga_{0.55}As$ capping layer, and this may suggest that the $In_{0.45}Ga_{0.55}As$ capping layer used above each of the self-assembled layers is a good way to minimise scattering loss. These characteristics make the presented structures promising optical sources for integration into silicon-photonic platforms. However, the combination of measurements, including TEM results, also suggest that the material consists of quantum dashes or even modulated QWs rather than QDs and, if the latter, may make

this design unsuitable for growth on silicon where the QDs are thought to be necessary for the insensitivity to defects.

The characterization of further designs of quantum dot lasers was presented in Chapter 7. Three epitaxial layer structures with 4 nm capping on InAs QDs were studied. Two were three-layer structures and one was a five-layer structure. Compared to the structures of Chapter 6 the thickness of the capping layers was increased, and two variants were introduced of $In_{0.45}Al_{0.275}Ga_{0.275}As$ (3 layer) and $In_{0.35}Ga_{0.65}As$ (3 and 5 layer). The intention was to increase the depth of the dot potential. Each structure was fabricated in two variants 90° to each other, to evaluate the dot or dash form of the 3D features, with the laser cavity axis aligned along the $[1\bar{1}0]$ direction or along the [110] direction. It was found that lasers fabricated with the $In_{0.35}Ga_{0.65}As$ capping layer had higher gain parameters along the [110] direction, which is indicative of these samples containing quantum dashes. The sample with $In_{0.45}Al_{0.275}Ga_{0.275}As$ capping had similar gain parameters in the two directions and putting this together with the TEM images suggest this sample was QW like.

The gain parameters derived from the lasers oriented along the [110] direction 17.5 ± 0.4 cm^{-1} and 27.6 ± 2 cm^{-1} for the 3- and 5-layer quantum dash samples respectively and 35.5 ± 0.6 cm^{-1} for the 3-layer QW like structure. It is worth noting that the gain achieved with the unintentional QWs in this chapter is lower compared to the conventional QWs discussed in Chapter 4 but reaches a similar level per layer. These modulated QW structures reach similar gain but do require much larger current density compared to the lasers of Chapter 4. The peak modal gain in the modulated quantum well devices is greater than that in quantum dash devices. Using the segmented contact technique positive gain was measured over a 150 nm bandwidth for both the 5-layer quantum dash and the 3-layer QW structures, which is slightly wider than the structure of Chapter 6. The internal optical loss derived from laser measurements was found to be: ~15.8 ± 2.2 cm^{-1}, ~20.5 ± 3.5 cm^{-1}, and ~11.0 ± 3.4 cm^{-1} at room temperature 21±1°C for structures 3-layer quantum dash, 5-layer quantum dash and 3-layer QW respectively. The results from the segmented contact technique are broadly in agreement, albeit with a slightly higher value being derived for the QW sample. The losses are substantially higher than that measured for the structure of Chapter 6 and may the reduction of light or the spreading of the optical mode into the substrate for the structures of Chapter 7, which was observed in the measured near field images.

This was not observed for the structure of Chapter 6, although it is not clear that this structure is substantially different to the ones in Chapter 7 with respect to the guiding of the optical mode. It is clear that every effort should be made to change the design to create better optical confinement so leakage of light into the substrate does not happen as this is very likely increasing the optical loss in these structures, which impacts laser performance substantially when the gain is relatively low.

The measurements of how the threshold current depends on temperature for the three structures of Chapter 7 at different device lengths showed that the 3-layer quantum dash sample only lases up to 330 K. The 5-layer quantum dash lase up to 370 K. Lasers made with a quantum well active material have a much better threshold current temperature dependence, operating up to 380 K. This is consistent with the magnitude of the available gain and suggest it is a critical factor in achieving good performance. In general, the QW like samples perform best but may not be suitable for growth on silicon. The 5-layer quantum dash performance is reasonably good and may be a good compromise for growth on silicon.

These findings highlight the potential of InAs QD based on InP lasers for growth on silicon and use in photonic integrated circuits.

8.2 Future work

The results discussed in this thesis provide a foundation for advancing the integration of InAs/InP quantum dot (QD) lasers into silicon photonic platforms. However, several challenges remain, further efforts are needed to enhance the performance and scalability of these devices.

This investigation examined the impact of the epitaxial layer structure with capping on InAs quantum dots for the creation of QD-based InP quantum dots or quantum dashes. Enhancing QD growth is essential for optimizing the devices, and further research in this area may provide useful information to enhance their operating performance.

This work demonstrated that quantum dot lasers maintain stable operation at temperatures up to 380 K. However, the performance of these devices at higher temperatures could be further optimized. Future research should focus on improving the thermal stability of the quantum dot structures, reducing the increase in operating

current at elevated temperatures, and enhancing optical gain. There are some strategies that may include exploring alternative capping layers and pre-layers to reduce carrier scattering and recombination rates at high temperatures and also to change the optical guiding to minimise the loss of light from the active layer. The results of Chapter 5 indicated that the integration of an electron blocker layer in the quantum dot QD structures is an additional option to try.

The asymmetry in the performance of the quantum dash material may cause limitations in PICs and so it may be necessary to perform further growth studies to try and identify the range of parameters necessary to produce quantum dots. It may also be worth trying out some of the QWs with varying width and composition on silicon. It is primarily the reduced diffusion and localisation of charge carriers that occurs with QDs that is required for growth on silicon. The broadening observed in the gain spectra for the QW samples indicates there is substantial variation in either well width or composition or both and this may be sufficient to localise the carriers and provide some insensitivity to defects.

To ensure the viability of quantum dot lasers for commercial and industrial applications, long-term reliability studies are necessary. These studies should assess the devices under a variety of operational conditions to evaluate their robustness and longevity. Understanding factors that influence degradation and failure rates will be critical for transitioning these technologies to practical applications. By addressing these areas of improvement, quantum dot lasers can achieve enhanced performance, scalability, and reliability, paving the way for their broader integration into silicon photonic platforms.

Future investigations could include a detailed study of Fermi-level pinning through second derivative voltage-to-current ($\frac{d^2V}{d^2I}$) measurements. Another promising avenue for research is the exploration of power-dependent sub-threshold electroluminescence EL and photoluminescence PL, which could provide deeper insights into the carrier dynamics at low excitation levels.

Additionally, low-temperature measurements within regimes where carrier confinement is observed in quantum dots QDs would provide further understanding of quantum effects and carrier behaviours. Investigating carrier diffusion through PL

measurements would complement this by helping to better understand transport properties at various temperatures.

Moreover, a future investigation could include near-field imaging of lasers as discussed in Chapter 6. This approach could be extended to examine potential substrate leakage, providing clarity on whether the observed laser characteristics are influenced by leakage currents or other substrate interactions.

References

1. Bimberg, D. & Ledentsov, N. Quantum dots: lasers and amplifiers. *Journal of Physics: Condensed Matter*. 15(24). R1063 (2003).

2. Yadav, A., Chichkov, N. B., Avrutin, E. A., Gorodetsky, A. & Rafailov, E. U. Edge emitting mode-locked quantum dot lasers. *Prog Quantum Electron* 87, 100451 (2023).

3. Poole, P. InP-based quantum dot lasers. in *Semiconductors and Semimetals* vol. 86 419–453. Elsevier, (2012).

4. Li, S.G., Gong, Q., Cao, C.F., Wang, X.Z., Yan, J.Y., Wang, Y. and Wang, H.L., The developments of InP-based quantum dot lasers. *Infrared Physics & Technology,* 60, 216–224 (2013).

5. Chen, S., Li, W., Wu, J., Jiang, Q., Tang, M., Shutts, S., Elliott, S. N., Sobiesierski, A., Seeds, A, J., Ross, I., Smowton, P. M., & Liu, H. Electrically pumped continuous-wave III-V quantum dot lasers on silicon. *Nature photonics* 10, 307–311 (2016). doi .10.1038/nphoton.2016.2110.

6. Blood, P., Lewis, G.M., Smowton, P.M., Summers, H., Thomson, J. & Lutti, J. Characterization of Semiconductor Laser Gain Media by the Segmented Contact Method. *in IEEE Journal on Selected Topics in Quantum Electronics* vol. 9(5), 1275–1282 (2003).